Doctoral Dissertation

Maximizing Potential of Graphene Oxide for Nanocatalysis

Gao Ce

Supervisor: Toshiaki Taniike

Graduate School of Advanced Science and Technology

Japan Advanced Institute of Science and Technology

Materials Science

September 2025

Maximizing Potential of Graphene Oxide for Nanocatalysis

Gao Ce

2220015

Graphene oxide (GO) and its derivatives such as graphene oxide frameworks (GOFs) are widely used as supports in the field of catalysis due to their high specific surface area, and abundance of various functional groups. Although properties of GO significantly influence the synthesis of their derivatives and interaction with the supported metal nanoparticles (NPs), the relationship between the properties of GO and the performance of the resultant nanocatalysts has not been systematically studied, which corresponds to the aim of this thesis.

In **Chapter 2**, GOFs have great potential as supports for metal NPs, due to their well-defined and engineerable pores. Since GOFs are prepared by bridging GO sheets with linker molecules, their properties depend on those of GO as the starting material. However, the diversity in the physicochemical properties of GO has prevented understanding key parameters for catalyst design. To address this issue, in this chapter, GOFs and GOF-supported Pd NP catalysts (Pd@GOFs) were synthesized from three GO samples with different properties. They were subjected to systematic characterization and catalytic recyclability test in Suzuki-Miyaura cross-coupling. The major findings are: The density of linker molecules in GOF is crucial for enhancing catalytic recyclability, which is influenced by the abundance of reactive in-plane functional groups in the raw GO samples. The gallery spaces between GO layers are important to maintain uniform dispersion of Pd NPs. GO with too small sheets cannot create such gallery spaces, leading to significant aggregation of NPs. Although GOFs have been demonstrated to be useful for various applications, the importance of the quality of the raw material, GO, has sometimes been overlooked. The results presented in this chapter, which assess the quality of GO samples using a multifaceted method, is valuable for fundamental research and design of nanocatalysts.

In **Chapter 3**, the intellectual design of catalysts is pivotal for developing advanced materials and enhancing various catalytic reactions, including electrochemical water splitting for sustainable energy production. Among different catalysts, Pd on GO supports has shown promise for the hydrogen evolution reaction (HER). Although numerous studies have utilized GO as a support material for HER catalysts, research on which specific properties of GO affect catalytic performance remains relatively scarce. Therefore, in this chapter, various GO materials with different characteristics were selected to synthesize GO-supported Pd NP catalysts. The catalysts were evaluated in HER. The properties of the GO materials were characterized using multiple techniques, and their catalytic performance was evaluated through linear sweep voltammetry (LSV) and electrochemical surface area normalization. The LSV results are shown in Figure 2. Firstly, the Pd NP catalyst supported on GOFs did not exhibit promising performance (not shown), but those of GOs showed reasonable performance, which is apparently an opposite trend compared to the Suzuki-Miyaura reaction discussed in Chapter 2, suggesting the importance of diffusion resistance in HER. Among all the catalysts, Pd/GO-GNP (GO prepared from graphene nanoplates (GNP)) exhibited the best HER performance, with the largest electrochemically active.

In **Chapter 4**, GOFs using several different linkers with varying functional groups were synthesized, aiming to investigate their effects on the structural and catalytic performance of GOF-confined catalysts. FTIR and XRD analyses revealed that linker types and amounts influence GOF properties, such as interlayer spacing and functional group retention. Pd@GOF catalysts, synthesized by incorporating palladium NPs into GOFs, were tested for their performance in the Suzuki-Miyaura

coupling reaction. Catalytic tests demonstrated that the linker's functional groups significantly affect activity and durability, highlighting the importance of balanced functional group availability and sufficient pillar density for retaining Pd NPs. Comparisons between GOF-confined and GO-supported catalysts indicated that GOFs effectively prevent NP agglomeration while offering enhanced recyclability. The study also noted that commercially sourced GO, with fewer in-plane functional groups, impacted catalytic retention. These findings provide valuable insights into designing high-performance GOF-based nanocatalysts by optimizing linkers and GO surface functionalization to meet diverse catalytic requirements.

In conclusion, this thesis highlights the pivotal role of GO's physicochemical properties and linker design in optimizing nanocatalyst performance. By systematically exploring the relationship between GO characteristics, linker functionality, and catalytic behavior, the findings offer a comprehensive understanding of material design strategies. This work provides a foundation for developing high-performance GOF-based catalysts tailored for specific reactions, bridging fundamental research and practical applications in sustainable catalysis and energy production.

Keywords: Graphene oxide; Nanocatalysts; Graphene oxide framework, Suzuki-Miyaura coupling reaction,

Referee-in-chief: Professor Toshiaki Taniike

Japan Advanced Institute of Science and Technology

Referees:

Professor Yoshifumi Oshima

Japan Advanced Institute of Science and Technology

Professor Kazuma Gotoh

Japan Advanced Institute of Science and Technology

Professor Noriyoshi Matsumi

Japan Advanced Institute of Science and Technology

Professor Akira Yada

National Institute of Advanced Industrial Science and Technology

Preface

The research thesis is submitted for the degree of doctor of philosophy at Japan Advanced Institute of Science and Technology, Japan. The thesis is consolidation of results of the research work on the topic “Maximizing Potential of Graphene Oxide for Nanocatalysis” under the supervision of Prof. Toshiaki Taniike during April 2022–March 2025 at Graduate School of Advanced Science and Technology, Japan Advanced Institute of Science and Technology.

Chapter 1 introduces the research background and objectives of this thesis.

Chapter 2 investigated the impact of graphene oxide (GO) properties on the catalytic performance of graphene oxide framework (GOF)-supported catalysts by preparing various qualities of GO and characterizing them.

Chapter 3 explored the influence of different GO properties on the electrocatalytic performance in hydrogenation reactions.

Chapter 4 investigated the impact of different crosslinking molecules on the catalytic performance of GOFs.

Finally, **Chapter 5** summarizes the findings and conclusions of the previous chapters of the thesis.

Gao Ce

Graduate School of Advanced Science and Technology

Japan Advanced Institute of Science and Technology

March 2025

Acknowledgments

First and foremost, I would like to express my deepest gratitude to my advisor, Professor Toshiaki Taniike of the School of Advanced Science and Technology at the Japan Advanced Institute of Science and Technology (JAIST), for his guidance and encouragement throughout my doctoral studies. His patience, professional insights, and extensive knowledge have been immensely helpful to me. I am also very thankful to Assistant Professor Toru Wada for his valuable suggestions and constructive discussions during my experiments and research. Additionally, I would like to extend my appreciation to all the members of the Taniike Laboratory for their assistance.

I deeply appreciate Prof. Yoshifumi Oshima (JAIST), Prof. Kazuma Gotoh (JAIST), Prof. Noriyoshi Matsumi (JAIST), Prof. Akira Yada (National Institute of Advanced Industrial Science and Technology) for their review and valuable suggestions. Last but not the least, my gratitude also extends to my family who has been assisting, supporting, and caring for all my life.

Gao Ce

Graduate School of Advanced Science and Technology

Japan Advanced Institute of Science and Technology

March 2025

Content

Chapter 1

General Introduction

Chapter 1

1.1. Graphene oxide

Graphene is a single-atom-layer, two-dimensional (2D) material composed of sp^2 hybridized carbon atoms arranged in a hexagonal honeycomb lattice.[1–7] Graphene was fully isolated and characterized in 2004. It potentially has widespread application in fields such as engineering, electrochemistry, medicine, and energy due to its excellent electrical conductivity, high thermal conductivity, exceptional mechanical strength, good flexibility, and large specific surface area.[8–10] However, the high costs associated with graphene, due to synthesis challenges, poor solubility, and its tendency to re-aggregate into graphite because of strong van der Waals interactions, limit its widespread application.[11–13]

Therefore, graphene oxide (GO) is a more promising alternative material, which is easier to synthesize and can retain certain properties of graphene.[1] The most common method for synthesizing GO involves the oxidation of graphite by the Hummers method.[14] This strategy was initially developed using various techniques by Brodie, Staudenmaier, Hummers, and Offerman, among others.[14–16] Due to the Hummers method being safer, more environmentally friendly, and offering greater potential for improvement, the Hummers method or modified Hummers method has been the most commonly employed for GO synthesis.[1,17]

Chapter 1

Similar to graphene, GO also is a 2D carbon-based nanomaterial.[7] As shown in **Figure 1.1**, GO contains a large amount of oxygen-containing functional groups, which can affect the GO preference.[2] In GO, the epoxy and hydroxyl groups are primarily located on the lateral surfaces, while carboxyl groups are mainly distributed along the edges of the graphene sheets.[18–20] Due to over-oxidation or exfoliation, defects are introduced into the GO sheets, further affecting the performance of materials.[1] The mechanical properties of GO are affected by the oxygen-containing functional groups and the number of defects on its surface, causing GO strength (276 ± 23.4 GPa) which is slightly lower than graphene (1.0 TPa).[21] However, after annealing in a hydrogen atmosphere, GO can achieve an exceptionally high strength (250 ± 150 TPa).[22] Also, the conductivity of GO is affected by defects and the abundance of functional groups on its layers, resulting in a wide conductivity range from 0.1 S/m to 29,800 S/m.[23] Similarly, due to the effect of functional group content and defects, the thermal conductivity of GO ranges from 0.5 to 1 W/mK.[24]

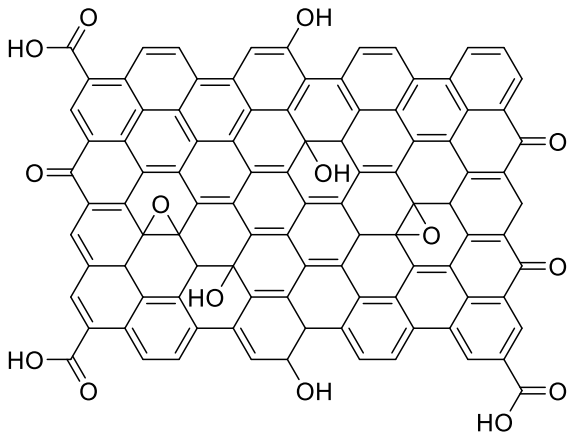

Figure 1.1 Structure and typical functional groups of GO.

Based on the easily adjustable properties and the ability for functional modification, GO and its derivative materials are widely applied in various fields. Due to the abundance of functional groups on GO and its impermeability to gases, modified GO-based composites are widely applied in high-selectivity small-molecule gas separation membranes.[25] With hydrophilicity driven by numerous oxygen-containing functional groups and an easily adjustable interlayer spacing, GO and its derivatives are also commonly used in water treatment membranes.[26,27] The presence of these functional groups prevents the restacking of GO sheets, creating internal porosity that shortens electronic transport distances, making GO and its derivatives ideal for use in energy storage devices such as high-performance, stable supercapacitors and lithium-ion batteries.[11] Moreover, their large

specific surface area allows for more active site exposure as catalyst supports, while abundant defects and functional groups serve as anchors to prevent the leaching and agglomeration of nanoparticles (NPs). These properties make GO and its derivatives valuable as supports for nanocatalysts.[28–30]

1.2. Graphene oxide framework

As mentioned in section 1.1, GO is rich in various oxygen-containing functional groups, which can be utilized directly or modified to introduce new functional groups, thereby enhancing its properties.[1] However, as a 2D material, GO tends to lose some of its unique properties due to excessive restacking, resulting in suboptimal performance in applications.[31,32] Therefore, leveraging the inherent functional groups and the easy modifiability of GO to construct well-organized and interconnected 3D framework structures is an effective strategy.[32,33] This approach helps retain unique properties for GO while providing a stable structure.[33]

Common strategies for constructing graphene oxide frameworks (GOFs) include the following methods. GO has strong chemical modification capabilities due to its numerous oxygen-containing functional groups.[1] One of the most common methods for constructing GOFs is using bifunctional crosslinking agents.[2,34] The interlayer spacing of GOFs can be adjusted

according to the length of the crosslinking agents.[35,36] Additionally, the covalently crosslinked structure of GOFs provides a rigid framework, offering enhanced stability in harsh environments. Compared to GO, covalently crosslinked GOFs exhibit superior mechanical properties. GOFs can also be constructed by coating GO with polymers. By embedding polymer NPs into GO nanosheets, the interlayer spacing can be adjusted, and the mechanical stability of the GOFs can be enhanced. GOFs can also be effectively constructed by uniformly dispersing solid NPes on the GO surface through methods such as in situ growth. However, GOFs prepared using this method often face challenges such as uneven NP distribution and difficulty in controlling the interlayer spacing.

GOFs retain GO's high surface area, excellent mechanical properties, diverse functional groups, and some of its electrical and thermal properties, while also allowing for the control and determination of pore sizes. As a result, they are widely used in various fields such as water purification, energy storage, gas storage, and catalyst support.

1.3. Supported nanocatalysts

With advancements of industrial production, environmental protection, and the energy industry, catalyst technology has become increasingly

important in these sectors. Catalysts are extensively studied for their ability to lower reaction conditions, increase reaction rates, minimize side reactions, and reduce industrial production costs while protecting the environment. Catalysts dispersed in the same phase as the reactants are called homogeneous catalysts, whereas those in a different phase are referred to as heterogeneous catalysts. Although homogeneous catalysts generally exhibit higher selectivity and catalytic activity, they are difficult to separate from the products after the reaction. In contrast, heterogeneous catalysts are easier to separate and reuse, making them more widely used in industrial applications. However, as heterogeneous catalysts are typically solid, their catalytic efficiency is often limited by the number of active sites exposed on their surface, resulting in lower overall activity.

Therefore, using nanoscale catalysts with a larger specific surface area, capable of exposing more active sites, is one effective way to enhance the catalytic activity of heterogeneous catalysts. However, nanocatalysts tend to agglomerate into larger particles with reduced surface area, leading to a decrease in exposed active sites and a rapid loss of catalytic activity. Anchoring nanocatalysts onto the surface of a support can effectively mitigate NP agglomeration, thereby improving their stability and enhancing their durability.

Thus, developing suitable catalyst supports is essential for enhancing the catalytic activity and durability of nanocatalysts. Currently, materials such as zeolites, carbon, and silica are widely used as catalyst supports. Their high porosity provides a large specific surface area for the dispersion of NPs, thereby enhancing the catalyst's reactivity. Additionally, functional groups and defects on these material surfaces act as anchoring sites for NPs, helping to improve their resistance to sintering and enhancing the stability of the nanocatalysts.

1.4. Aim of thesis

The development of industrial production activities has created the need for high-performance catalysts and related materials increasingly urgent. Although nanocatalysts exhibit high catalytic efficiency, they tend to agglomerate, which reduces their durability and significantly increases their usage costs, thereby limiting their application in industrial production. Enhancing both the catalytic performance and durability of nanocatalysts remains a key challenge. Therefore, developing superior support materials is crucial for improving the performance and durability of nanocatalysts.

GO and its derivatives, with their large surface area and ease of modification, hold significant potential as support materials for nanocatalysts.

Chapter 1

Maximizing the potential of GO in nanocatalysis is a promising solution to the challenges associated with catalyst performance and stability.

In this research is aimed to clarify the key role that different physicochemical properties of GO play in determining the performance and stability of various supported nanocatalysts under catalytic reaction conditions, as well as methods for controlling the synthesis of functional groups to create highly recyclable supported catalysts. In this study, various GO materials with different characteristics and their derivatives were synthesized and compared, then applied to different catalytic reactions to explore the relationship between the properties of GO and their catalytic performance. My research consists of the following three chapters:

The primary objective of Chapter 2 is to elucidate the influence of GO characteristics on GOF. Various precursors are used to synthesize GO, which is then intercalated with 1,4-phenylenediboronic acid (PDBA) to obtain rigid and well-defined GOFs. Multiple characterization techniques are employed to analyze and compare both GO and GOF, aiming to discuss and determine the specific GO properties required for GOF to function effectively as a framework material.

Chapter 3 aims to investigate the physicochemical properties of a series of GO-supported Pd nano catalysts derived from various graphite sources

and to elucidate their hydrogen evolution reaction (HER) performance. The results of this study will provide guidance for designing efficient HER electrocatalysts based on the material properties and electrochemical behavior.

Chapter 4 focuses on exploring the impact of different linker molecules on the constructed GOFs. In this chapter, quality-assured GO was uniformly used, and five linkers with different functional groups were employed to create GOFs through various covalent reactions. The effects of these linkers on the GOFs were then determined through multiple characterization techniques and catalytic applications.

Based on this research, it is identified that the properties of GO and certain GO derivatives, as well as their significance in influencing the performance of supported catalysts under various catalytic conditions. I believe that this study provides valuable guidance for the targeted design and synthesis of high-quality GO and GO derivatives.

References

(1) Smith, A. T.; LaChance, A. M.; Zeng, S.; Liu, B.; Sun, L. Synthesis, Properties, and Applications of Graphene Oxide/Reduced Graphene Oxide

and Their Nanocomposites. *Nano Materials Science* **2019**, *1* (1), 31–47. https://doi.org/10.1016/j.nanoms.2019.02.004.

(2) Chen, D.; Feng, H.; Li, J. Graphene Oxide: Preparation, Functionalization, and Electrochemical Applications. *Chem. Rev.* **2012**, *112* (11), 6027–6053. https://doi.org/10.1021/cr300115g.

(3) Geim, A. K.; Novoselov, K. S. The Rise of Graphene. *Nat. Mater.* **2007**, *6* (3), 183–191. https://doi.org/10.1038/nmat1849.

(4) Sykes, E. C. H. Graphene Goes Undercover. *Nat. Chem.* **2009**, *1* (3), 175–176. https://doi.org/10.1038/nchem.224.

(5) Li, D.; Kaner, R. B. Graphene-Based Materials. *Science* **2008**, *320* (5880), 1170–1171. https://doi.org/10.1126/science.1158180.

(6) Brumfiel, G. Graphene Gets Ready for the Big Time: Physicists Are Talking about How to Make Practical Use of a Former Laboratory Curiosity. *Nature* **2009**, *458* (7237), 390–392.

(7) Huang, X.; Yin, Z.; Wu, S.; Qi, X.; He, Q.; Zhang, Q.; Yan, Q.; Boey, F.; Zhang, H. Graphene-Based Materials: Synthesis, Characterization, Properties, and Applications. *Small* **2011**, *7* (14), 1876–1902. https://doi.org/10.1002/smll.201002009.

(8) Novoselov, K. S.; Geim, A. K.; Morozov, S. V.; Jiang, D.; Zhang, Y.; Dubonos, S. V.; Grigorieva, I. V.; Firsov, A. A. Electric Field Effect in

Atomically Thin Carbon Films. *Science* **2004**, *306* (5696), 666–669. https://doi.org/10.1126/science.1102896.

(9) Bolotin, K. I.; Sikes, K. J.; Jiang, Z.; Klima, M.; Fudenberg, G.; Hone, J.; Kim, P.; Stormer, H. L. Ultrahigh Electron Mobility in Suspended Graphene. *Solid State Communications* **2008**, *146* (9–10), 351–355. https://doi.org/10.1016/j.ssc.2008.02.024.

(10) Morozov, S. V.; Novoselov, K. S.; Katsnelson, M. I.; Schedin, F.; Elias, D. C.; Jaszczak, J. A.; Geim, A. K. Giant Intrinsic Carrier Mobilities in Graphene and Its Bilayer. *Phys. Rev. Lett.* **2008**, *100* (1), 016602. https://doi.org/10.1103/PhysRevLett.100.016602.

(11) Zhu, Y.; Murali, S.; Cai, W.; Li, X.; Suk, J. W.; Potts, J. R.; Ruoff, R. S. Graphene and Graphene Oxide: Synthesis, Properties, and Applications. *Adv. Mater.* **2010**, *22* (35), 3906–3924. https://doi.org/10.1002/adma.201001068.

(12) Kuilla, T.; Bhadra, S.; Yao, D.; Kim, N. H.; Bose, S.; Lee, J. H. Recent Advances in Graphene Based Polymer Composites. *Progress in Polymer Science* **2010**, *35* (11), 1350–1375. https://doi.org/10.1016/j.progpolymsci.2010.07.005.

(13) Niyogi, S.; Bekyarova, E.; Itkis, M. E.; McWilliams, J. L.; Hamon, M. A.; Haddon, R. C. Solution Properties of Graphite and Graphene. *J. Am. Chem. Soc.* **2006**, *128* (24), 7720–7721. https://doi.org/10.1021/ja060680r.

(14) Hummers, W. S.; Offeman, R. E. Preparation of Graphitic Oxide. *J. Am. Chem. Soc.* **1958**, *80* (6), 1339–1339. https://doi.org/10.1021/ja01539a017.

(15) Staudenmaier, L. Verfahren Zur Darstellung Der Graphitsäure. *Berichte der deutschen chemischen Gesellschaft* **1898**, *31* (2), 1481–1487. https://doi.org/10.1002/cber.18980310237.

(16) Brodie, B. C. XIII. On the Atomic Weight of Graphite. *Philos. Trans. Roy. Soc. London* **1859**. https://doi.org/10.1098/rstl.1859.0013.

(17) Pendolino, F.; Armata, N. *Graphene Oxide in Environmental Remediation Process*; SpringerBriefs in Applied Sciences and Technology; Springer International Publishing: Cham, 2017. https://doi.org/10.1007/978-3-319-60429-9.

(18) Eda, G.; Chhowalla, M. Chemically Derived Graphene Oxide: Towards Large-Area Thin-Film Electronics and Optoelectronics. *Adv. Mater.* **2010**, *22* (22), 2392–2415. https://doi.org/10.1002/adma.200903689.

(19) Kim, F.; Cote, L. J.; Huang, J. Graphene Oxide: Surface Activity and Two-Dimensional Assembly. *Adv. Mater.* **2010**, *22* (17), 1954–1958. https://doi.org/10.1002/adma.200903932.

(20) Li, X.; Zhang, G.; Bai, X.; Sun, X.; Wang, X.; Wang, E.; Dai, H. Highly Conducting Graphene Sheets and Langmuir-Blodgett Films. *Nat. Nanotechnol.* **2008**, *3* (9), 538–542. https://doi.org/10.1038/nnano.2008.210.

(21) Suk, J. W.; Piner, R. D.; An, J.; Ruoff, R. S. Mechanical Properties of Monolayer Graphene Oxide. *ACS Nano* **2010**, *4* (11), 6557–6564. https://doi.org/10.1021/nn101781v.

(22) Gómez-Navarro, C.; Burghard, M.; Kern, K. Elastic Properties of Chemically Derived Single Graphene Sheets. *Nano Lett.* **2008**, *8* (7), 2045–2049. https://doi.org/10.1021/nl801384y.

(23) Pei, S.; Zhao, J.; Du, J.; Ren, W.; Cheng, H.-M. Direct Reduction of Graphene Oxide Films into Highly Conductive and Flexible Graphene Films by Hydrohalic Acids. *Carbon* **2010**, *48* (15), 4466–4474. https://doi.org/10.1016/j.carbon.2010.08.006.

(24) Renteria, J. D.; Ramirez, S.; Malekpour, H.; Alonso, B.; Centeno, A.; Zurutuza, A.; Cocemasov, A. I.; Nika, D. L.; Balandin, A. A. Strongly Anisotropic Thermal Conductivity of Free-Standing Reduced Graphene

Oxide Films Annealed at High Temperature. *Adv. Funct. Mater.* **2015**, *25* (29), 4664–4672. https://doi.org/10.1002/adfm.201501429.

(25) Yang, Y.-H.; Bolling, L.; Priolo, M. A.; Grunlan, J. C. Super Gas Barrier and Selectivity of Graphene Oxide-Polymer Multilayer Thin Films. *Adv. Mater.* **2013**, *25* (4), 503–508. https://doi.org/10.1002/adma.201202951.

(26) Hu, M.; Mi, B. Enabling Graphene Oxide Nanosheets as Water Separation Membranes. *Environ. Sci. Technol.* **2013**, *47* (8), 3715–3723. https://doi.org/10.1021/es400571g.

(27) Nair, R. R.; Wu, H. A.; Jayaram, P. N.; Grigorieva, I. V.; Geim, A. K. Unimpeded Permeation of Water through Helium-Leak–Tight Graphene-Based Membranes. *Science* **2012**, *335* (6067), 442–444. https://doi.org/10.1126/science.1211694.

(28) Melo, J. P.; Ríos, P. L.; Povea, P.; Morales-Verdejo, C.; Camarada, M. B. Graphene Oxide Quantum Dots as the Support for the Synthesis of Gold Nanoparticles and Their Applications as New Catalysts for the Decomposition of Composite Solid Propellants. *ACS Omega* **2018**, *3* (7), 7278–7287. https://doi.org/10.1021/acsomega.8b00837.

(29) Li, Y.; Gao, W.; Ci, L.; Wang, C.; Ajayan, P. M. Catalytic Performance of Pt Nanoparticles on Reduced Graphene Oxide for Methanol Electro-

Oxidation. *Carbon* **2010**, *48* (4), 1124–1130. https://doi.org/10.1016/j.carbon.2009.11.034.

(30) Nawaz, M.; Miran, W.; Jang, J.; Lee, D. S. One-Step Hydrothermal Synthesis of Porous 3D Reduced Graphene Oxide/TiO2 Aerogel for Carbamazepine Photodegradation in Aqueous Solution. *Appl. Catal. B* **2017**, *203*, 85–95. https://doi.org/10.1016/j.apcatb.2016.10.007.

(31) Liu, F.; Zhang, L.; Wang, L.; Zhao, B.; Wu, W. Graphene Oxide for Electronics. In *Oxide Electronics*; John Wiley & Sons, Ltd, 2021; pp 1–19. https://doi.org/10.1002/9781119529538.ch1.

(32) Singh, R.; Ullah, S.; Rao, N.; Singh, M.; Patra, I.; Darko, D. A.; Issac, C. P. J.; Esmaeilzadeh-Salestani, K.; Kanaoujiya, R.; Vijayan, V. Synthesis of Three-Dimensional Reduced-Graphene Oxide from Graphene Oxide. *J. Nanomater.* **2022**, *2022* (1), 8731429. https://doi.org/10.1155/2022/8731429.

(33) Sun, Z.; Fang, S.; Hu, Y. H. 3D Graphene Materials: From Understanding to Design and Synthesis Control. *Chem. Rev.* **2020**, *120* (18), 10336–10453. https://doi.org/10.1021/acs.chemrev.0c00083.

(34) Eigler, S.; Grimm, S.; Hirsch, A. Investigation of the Thermal Stability of the Carbon Framework of Graphene Oxide. *Chem. - Eur. J.* **2014**, *20* (4), 984–989. https://doi.org/10.1002/chem.201304048.

(35) Hung, W.-S.; Tsou, C.-H.; De Guzman, M.; An, Q.-F.; Liu, Y.-L.; Zhang, Y.-M.; Hu, C.-C.; Lee, K.-R.; Lai, J.-Y. Cross-Linking with Diamine Monomers to Prepare Composite Graphene Oxide-Framework Membranes with Varying d-Spacing. *Chem. Mater.* **2014**, *26* (9), 2983–2990. https://doi.org/10.1021/cm5007873.

(36) Li, B.; Wang, C.-G.; Erdeanna Surat'man, N.; Jun Loh, X.; Li, Z. Microscopically Tuning the Graphene Oxide Framework for Membrane Separations: A Review. *Nanoscale Adv.* **2021**, *3* (18), 5265–5276. https://doi.org/10.1039/D1NA00483B.

Chapter 2

Critical Properties for Stabilizing Palladium Nanoparticles in Graphene Oxide Framework-Supported Catalysts: Insights from Multifaceted Characterization

Chapter 2

Abstract

Graphene oxide frameworks (GOFs) have great potential as supports for metal nanoparticle (NP) catalysts due to their advantageous properties such as engineerable pores. Since GOFs are prepared by bridging graphene oxide (GO) sheets with linker molecules, their properties depend on the GO raw material, and thus designing guidelines for GOs is important but has not been established yet. The most significant obstacle is the diversity of the physicochemical properties of GOs, making it difficult to determine which properties are linked to their performance as catalyst supports. To address this issue, we synthesized GOFs from three GOs with different properties, loaded them with Pd NPs, and evaluated their catalytic performance in Suzuki-Miyaura reaction. Using a multifaceted characterization approach, the following facts were found: The amount of linker molecules in the GOFs, and thus the amount of reactive functional groups in the GOs to anchor the linker molecules, are vital for the stabilization of Pd NPs. Therefore, to obtain highly dispersed and recyclable Pd NP catalysts, it is important to synthesize the raw GO materials at the site and convert them to GOFs as freshly as possible and under mild conditions. Although GOFs have been demonstrated to be useful for various applications, the importance of the quality of the raw material, GO, has sometimes been overlooked. The approach presented in

this study, which assesses the quality of GOs using a multifaceted method, is likely to be valuable for fundamental research and the enhancement of performance in all GOF materials.

Keywords: Graphene oxide framework; Pd nanoparticle; Suzuki-Miyaura cross-coupling; Catalyst supports; Catalytic recyclability; Multifaceted characterization

Chapter 2

2.1. Introduction

Metal nanoparticle (NP) catalysts have garnered significant attention due to their unique catalytic properties arising from the high surface-to-volume ratio, rich active surface atoms, and unique electronic structures as compared with their bulk counterparts.[1,2] However, the NPs easily aggregate and decrease in activity during use, posing challenges in practical implementation.[3] Thus, stabilizing NPs has been a vital aspect of NP catalyst research. Graphene oxide frameworks (GOFs), a three-dimensional graphene-based material, have emerged as promising catalyst supports due to their high surface area, low mass density, engineerable pores, and high mechanical strength.[4–6] Particularly, their engineerable pores are promising to stabilize metal NPs and control their growth, which are significant for active catalysts. Compared to GOFs prepared by non-covalent interaction,[7–11] those covalently constructed by intercalating graphene oxide (GO) layers with organic linkers are very important for durable catalytic processes.[12–17]

GOFs have often been employed in hydrogen storage,[12,18,19] water desalination,[20-22] molecular sieves,[23-25] and in the extraction of herbicides.[26,27] Conceptually, utilizing GOFs as catalyst supports would provide advantages, such as preventing direct exposure of NPs and improving their structural and interfacial stability. Based on these

characteristics, GOFs are expected to be promising supports for the confinement and immobilization of NPs. Until recently, there have been hardly any reports in the literature about successful employment of GOFs in organic transformation reactions.[5,28] We have reported the successful synthesis of GOF-confined Pd NP catalysts using a GOF as a support and their application in Suzuki-Miyaura coupling reaction,[29] clarifying the recyclability was superior to that of a commercial Pd/C catalyst. The same concept was extended to Ru catalysts for hydrogenation application.[30] Furthermore, we have reported the synthesis of GOFs tailored with additional organic ligands containing heteroatoms to enhance the stability of the confined Pd NPs.[31]

To enhance the stability of GOF itself, which is very essential for maintaining the catalytic activity, significant efforts have been reported to optimize synthetic parameters such as temperature to suppress reduction of GOs, choice of solvent to achieve good dispersibility, and the concentration of linker to produce a rigid framework.[32] However, the importance of GOs and their precursors in improving the resulted GOFs quality remains an open subject. It is well known that the size and morphology of graphite, as a source of GOs, can significantly affect the size, morphology, and distribution of reactive groups in the produced GOs. For example, several studies[33–36] have

successfully demonstrated that smaller graphite particles lead to the formation of highly dispersed GOs with more oxidized groups.[33–36] Moreover, the abundance of functional groups and their distribution (in-plane or edge) on GO is crucial for synthesizing covalently linked GOF using 1,4-phenylenediboronic acid (PDBA), in which the hydroxyl (-OH), epoxy (-O-), and carboxyl (-COOH) groups present on GOs serve as reactive sites for cross-linking with PDBA. Specifically, the hydroxyl and carboxyl groups can directly react with the phenylboronic acid moieties of PDBA to form ester linkages, resulting in the covalent attachment of the linker to the GO sheets. The presence of moisture in GOs facilitates the ring-opening reaction of epoxy with boronic acid at a moderate temperature, leading to additional cross-linking within the GOF structure.[33,37,38] Therefore, fundamental understanding of the reactive groups of GOs and their contribution in establishing stable GOF is necessary for enhancing catalytic performance. To the best of our knowledge, there are no literature reports on how the physicochemical properties of GOs could effectively influence the structure of GOF and, in turn, its utility as a catalyst support for achieving higher stability.

Our focus in this research is elucidating the impact of the properties of GOs on the resulting GOFs. In addition to a commercial GO, we synthesized

various GOs using different precursors, and then GO layers were intercalated with PDBA to afford a rigid and well-defined GOF. Finally, supported Pd NP catalysts were obtained through the thermal decomposition of $PdCl_2$ in the presence of synthesized GOFs and dried toluene, avoiding the use of any supplementary reductants and stabilizers such as polymers or surfactants.[29] The catalytic activity was investigated in the Suzuki-Miyaura cross-coupling reaction, which is the most widely employed organic transformation for constructing carbon-carbon bonds. The encapsulation effectively prevented sintering and leaching of Pd NPs. Because GOs have multifaceted properties from both chemical and physical perspectives, systematic and multifaceted characterization is vital. Here, we applied Raman spectroscopy, thermogravimetric-differential analysis (TG-DTA), X-ray diffraction (XRD), X-ray photoelectron spectroscopy (XPS), Fourier transform infrared spectroscopy (FT-IR), scanning electron microscopy (SEM), and transmission electron microscopy (TEM) at each synthetic stage. This comprehensive approach allowed us to thoroughly investigate properties such as defects, interlayer spacing, elemental composition, functional groups, and morphology. By comparing the multifaceted characterization results with the catalytic properties, particularly recyclability, we identified and

discussed the critical properties of GO required for constructing GOF as a catalyst support.

2.2. Experimental section

2.2.1. Materials

Three sources of GOs, including one purchased from a commercial source, and two synthesized from different carbon sources, were used for the synthesis of GOFs. **Table 2.1** summarizes the sample codes and the carbon sources used to synthesize GOs.

Table 2.1 Sample code.

Carbon material	GO code	GOF code
N.A. [a]	GO-commercial	GOF-commercial
Graphite (> 45 μm)	GO-graphite	GOF-graphite
Graphene nanoplatelets (< 2 μm)	GO-GNP	GOF-GNP

a The GO was purchased from a commercial source.

GO-commercial (dry powder, 50–100 mesh) was obtained from Layer One – Advanced Materials. Graphene nanoplatelets (particle size < 2 μm) were sourced from Strem Chemicals. Graphite (particle size > 45 μm, purity

> 98%), diethyl ether, and potassium carbonate were acquired from Wako Pure Chemical Industries. Graphite (particle size < 150 μm), PDBA (purity > 95.0%), and palladium (II) chloride ($PdCl_2$) were supplied by Sigma Aldrich. Hydrogen peroxide (35% aqueous solution), bromobenzene, and phenylboronic acid were provided by Tokyo Chemical Industry Co., Ltd. Sulfuric acid, potassium permanganate, toluene, methanol, ethanol were purchased from Kanto Chemical Co., Inc. All the materials were used as received without further purification.

2.2.2. Synthesis of GOs

GOs were prepared based on the modified Hummers method as reported in the literature.[39] A carbon material (3.0 g) and concentrated sulfuric acid (69 mL) were mixed in an ice bath at 0 °C. Then, potassium permanganate (9.0 g) was slowly added to the mixture under stirring, and the solution was kept stirred at r.t. for 30 min. Deionized (DI) water (69 mL) was added dropwise into the mixture, ensuring that the temperature did not exceed 98 °C. After stirring for 15 min, the mixture was diluted with 420 mL of DI water and thoroughly mixed. Finally, hydrogen peroxide (30 mL) was added, and the mixture was further stirred at r.t. for 24 h. The obtained GO dispersion

was repeatedly washed by centrifugation (10,000 rpm, 10 min) with DI water until the pH became 7, and then freeze-dried.

2.2.3. Synthesis of GOFs

GOFs were synthesized by a solvothermal method as reported by Buress et al.[18] A GO (300 mg) and PDBA (600 mg) were added to methanol (60 mL) in an autoclave under an N_2 atmosphere. The mixture was treated at 90 °C for 48 h and stirred occasionally. After completion of the reaction, the sample was washed with methanol three times by decantation, and then the remaining powder was vacuum-dried at 60 °C for 12 h.

2.2.4. Synthesis of Pd NP catalysts

Pd NP catalysts were synthesized through the reduction of $PdCl_2$ in the presence of GOFs in toluene.[29] In this method, the reactive functional groups present on the support were exploited as a reductant for NPs formation. $PdCl_2$ (18 mg) with a GOF (90 mg) in toluene (45 mL) was heated at 80 °C with stirring for 4 h under an N_2 atmosphere. After the reaction, the solution was cooled down to r.t. The solvent was removed using a syringe equipped with a 0.22 μm PES membrane (EMD Millipore) filter. The solid part was washed with diethyl ether (60 mL). Finally, the sample was vacuum-dried at 60 °C

for 12 h. For comparison, reference catalysts were also prepared using GOs instead of GOFs, following the same procedure. The catalysts confined within GOFs and supported on GOs are referred to as Pd@GOF and Pd/GO, respectively.

2.2.5. Characterization

In order to investigate the thermal behaviors, TG-DTA was performed on Thermo plus EVO2 (Rigaku) under a N_2 atmosphere. A sample contained in an alumina pan was heated from 30 to 800 °C at a ramping rate of 5 °C/min. The decomposition of functional groups can be assessed through mass loss and heat release. The interlayer distance (d-spacing) between GO sheets was determined based on powder XRD. The XRD patterns were recorded in the 2θ range of 3–60° at a speed of 10°/min and a step size of 0.01° on MiniFlexC600 (Rigaku) with Cu Kα radiation (λ = 1.5418 Å). Raman spectra of powder samples dispersed on a glass plate were recorded using a laser Raman spectrometer, NRS-4100 (JASCO) with an excitation wavelength of 532 nm and an exposure time of 25 s with 10 acquisitions. The FT-IR spectra were acquired using JASCO 6100 (JASCO) in the range of 4,000–400 cm^{-1} with a resolution of 4 cm^{-1} by 16 scans. Sample powder was ground with dried KBr at a weight ratio of 1:50 and then pressed into a pellet. To get more

insights into the surface functional groups, in-situ FT-IR measurements with temperature ramping were conducted. A KBr diluted pellet was placed in a Harrick cell equipped with KBr windows and connected to a vacuum line. Then the pellet was heated from 30 to 200 °C at a ramping rate of 1 °C/min under vacuum. XPS was used to investigate the chemical composition and the chemical state of individual elements. The spectra were recorded on Kratos AXIS Ultra DLD (Shimadzu) equipped with an Al-Kα anode. Powder samples were loaded onto a sample holder using double-sided adhesive copper tape. The survey spectrum was recorded with a 1 eV step size and a pass energy of 80 eV. Narrow scans were recorded with a 0.1 eV step size and a pass energy of 160 eV. The binding energies were calibrated using the C 1s peak of graphitic carbon at 284.6 eV. The sample powder was spread evenly on copper tape and measurement positions were determined by adjusting the stage position to the location where the C 1s peak of the sample exhibited the highest intensity. The spectra were analyzed using XPSpeak 4.1 software, with baseline correction performed using the Shirley method. The elemental composition was calculated by the area ratio of the detected peaks. Note that the Cu peak was not detected in any of the samples, ruling out the possibility that the observed C and oxygen-containing functional group originated from the copper tape. The amount of PDBA linkers and Pd

NPs loading were estimated by the contents of B and Pd, respectively. The morphology, particle size, and particle size distribution of the Pd NPs were investigated by TEM using H-7650 (Hitachi) operating at an acceleration voltage of 100 kV. A sample is dispersed in ethanol with ultrasonication for 15 min, then dropped onto a carbon-coated copper grid and naturally dried overnight. The surface morphology was observed by SEM using TM-3030-plus (Hitachi), with an accelerating voltage of 15 kV. The sample was spread onto a copper tape for the measurement.

The dispersion of Pd NPs were evaluated through dispersion index (*D*), which calculated using the Delaunay–Voronoi tessellation method, implemented via the Delaunay–Voronoi plugin in ImageJ.[40–42] This method constructs a network of triangles by connecting neighboring particles in such a way that no other point lies within the circumcircle of any triangle. It effectively captures the spatial relationships and uniformity of particle distribution across the support.

To quantify the uniformity of particle dispersion, we calculated a dispersion index (*D*) using the following formula:

$$D = \left(\frac{0.2}{\sqrt{2\pi}}\right) \times \frac{Avarage\ distance}{Standard\ deviation} \quad (1),$$

In this expression, the average distance refers to the mean edge length in the Delaunay triangulation, while the standard deviation represents the

variation in these distances. A higher value of *D* indicates a more uniform and evenly spaced distribution of particles.

2.2.6. Catalytic test

Pd@GOF and Pd/GO catalysts were used in the Suzuki-Miyaura coupling reaction of bromobenzene and phenylboronic acid to form biphenyl. Under a N_2 atmosphere, a catalyst (17.5 mg), phenylboronic acid (67.6 mg), bromobenzene (52.6 μL), and potassium carbonate (193.5 mg) were mixed in toluene (2.0 mL). The mixture was heated at 80 °C and stirred under N_2 for 6 h. After the reaction, the liquid part was separated by decantation following centrifugation (10,000 rpm, 5 min). The separated liquid was analyzed using an 7890A (Agilent) equipped with a flame ionization detector (GC-FID). The yield was calculated using the following equation:

$$yield = \frac{[biphenyl]}{[bromobenzene]_0} \times 100\% \quad (2),$$

where the $[bromobenzene]_0$ is the initial concentration of bromobenzene and the [biphenyl] is the concentration of biphenyl after the reaction. The concentration was determined using GC-FID employing an external standard method.

To evaluate recyclability, the solid part was washed 5 times with toluene (5 mL) through decantation and centrifugation (10,000 rpm, 5 min). The

washed catalyst was employed for the subsequent cycle of the reaction. The catalytic recyclability was assessed by determining the reduction in the yield.

2.3. Results and discussion

2.3.1. Characterization of GOs

The structural characteristics of GOs are multifaceted in terms of the following three perspectives: i) The types, numbers, and distribution of functional groups. Generally, the most abundant functional groups in GO are epoxide and hydroxyl groups. Additionally, carbonyl and carboxyl groups, which arise from the cleavage of C=C bonds due to over-oxidation, are found at the edges of the GO sheet.[38] Other functional groups identified so far include C-H, lactol, peroxide, dioxolane, ether, and anhydride.[43] ii) Defects in the GO sheets such as sp^3 hybridized carbon atoms resulting from functionalization, edges, and vacancies. iii) Physical properties such as the interlayer distance, number of stacking sheets, lateral size of the sheets, and the morphology as well as pore architecture of the secondary particles formed by aggregation. Here, we utilized a combination of multiple characterization methods to figure out key properties of GO that determine the performance of the final Pd@GOF.

Figure 2.1 summarizes the result of multifaceted characterization for the three GO samples: The two GOs (GO-GNP and GO-graphite) synthesized from different sources, whose chemical and structural properties differ, and the commercially available GO (GO-commercial). **Figure 2.1A** shows the FT-IR spectra. GO-graphite exhibited a broad peak centered around 3,450 cm^{-1}, attributed to the stretching of OH groups, indicating the presence of adsorbed water and surface OH groups. The broad peak at 1,747 cm^{-1} is attributed to ketone and carboxyl groups, while the other broad peak at 1,626 cm^{-1} is from sp^2 hybridized C=C (in-plane stretching) or adsorbed water. The two broad absorption bands observed for GO-graphite at 1,232 cm^{-1} and 876 cm^{-1} can be attributed to in-plane epoxy (C-O-C), which is known to appear at 1,230 cm^{-1} (asymmetric stretching) and around 850 cm^{-1} (bending motion). The peak at 1,060 cm^{-1}, observed between the epoxy peaks, is attributed to C-OH.[43] GO-GNP exhibited weaker and broader peaks at similar positions to those for GO-graphite. On the other hand, the in-plane epoxy absorption bands could not be observed in GO-commercial due to the overlapping of intense absorption bands at 1,263 cm^{-1}, 1,105 cm^{-1}, and 1,024 cm^{-1}. The clear assignment of these peaks is difficult due to the overlapping of peaks from many candidates,[43] but the appearance of similar peaks during the conversion of GO-graphite to GOF (discussed in **Figure 2.3**) suggests

that they are derived from some functional groups produced by reduction through hydrothermal treatment. GO-commercial also exhibited a sharp peak at 803 cm^{-1}, which is known to originate from aggregated edge esters.[43] The other peak observed at 2,964 cm^{-1} is attributed to the C-H of sp^3 hybridized carbon, which is often observed in reduced GO.[44,45] These IR observations indicate the types and quantities of the functional groups vary depending on the GO samples.

In the XRD patterns shown in **Figure 2.1B**, GO-graphite and GO-commercial exhibited intense single peaks corresponding to the separation of GO sheets at 8.3° (d = 10.7 Å) and 11.0° (d = 8.0 Å), respectively. The expansion of the d-spacing can be attributed to the loss of the strong π-π interaction among the sheets and the distortion within a GO sheet due to the formation of sp^3 hybridized carbons by functionalization,[38,42] and the interlayer insertion of functional groups[38,42] or residual water.[46] GO-GNP only had a broad and small hump at 11.6° (d = 7.6 Å), indicating that the number of stacked GO sheets is quite small compared to the other samples.

Figure 2.1C shows the Raman spectra of the GO samples. Raman spectra of graphene-like carbonous materials are generally characterized by the intensity ratio of the G-band peak at 1,581 cm^{-1}, which is derived from in-plane bond-stretching motion of sp^2 carbon pairs (E_{2g} symmetry), and the

D-band peak at 1,355 cm^{-1} (A_{1g} symmetry). The *D* mode is forbidden in perfect graphite and only becomes active in the presence of disorder causing disconnection of the fused aromatic rings. The disorder includes atomic defects such as a carbon vacancy/edges and the presence of sp^3 carbon due to in-plane functionalization.[47] The relatively high I_D/I_G ratio of GO-GNP, despite the low functionalization confirmed by FT-IR, can be attributed to the presence of many edges. GO-commercial showed the lowest I_D/I_G ratio, suggesting the largest lateral size of the sheets and the least in-plane functionalization.

The TG-DTA analyses under a N_2 atmosphere shown in **Figure 2.1D** provide further insights into the differences in functional groups. Each GO sample displayed two distinct weight losses: An initial minor loss with endotherm below 100 °C and a 40–50% weight loss with exotherm above 100 °C. The extent of the second weight loss and the temperature of its occurrence differed significantly among the samples: GO-GNP exhibited a broad and weak exothermic peak at 160 °C with a gradual weight loss, while GO-graphite showed a more prominent exothermic peak at 142 °C with a distinct weight loss, which was followed by further weight loss without exothermic over around 200 °C. On the other hand, GO-commercial exhibited a more intense exothermic peak at 214 °C. It is believed that such

differences in thermal behavior are indicative of variations in the types and quantity of surface functional groups.

To ascertain the origins of the thermal behaviors, the temperature-dependent transitions in the FT-IR spectra of GO-graphite and GO-commercial were monitored (**Figure 2.2**). Note that the in-situ FT-IR measurements were executed under vacuum, and molecular release events happened at lower temperature compared to the TG-DTA under an ambient pressure. **Figure 2.2A** and **2.2B** show the transient of fingerprint region. It is obvious that the in-plane epoxy groups observed in GO-graphite decreased with increasing temperature and disappeared at 80 °C, while GO-commercial showed no change.

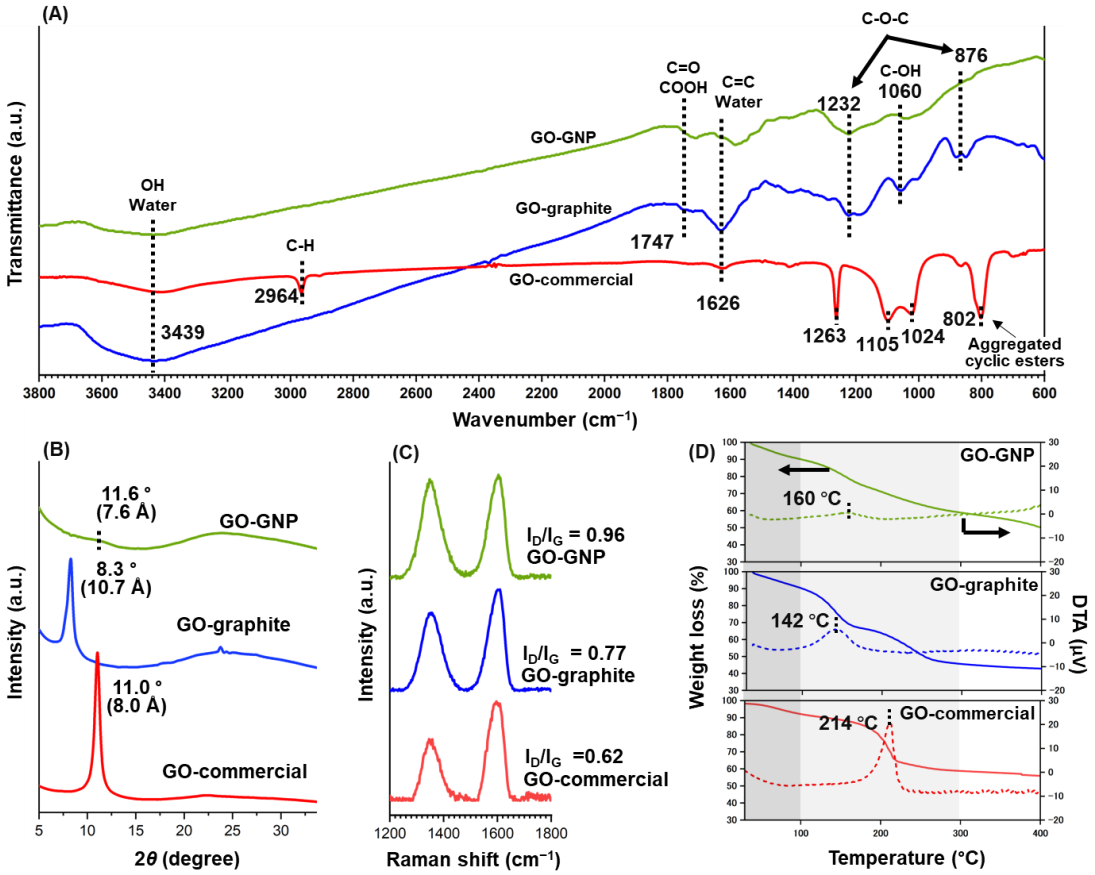

Figure 2.1. Summary of the multifaceted analysis for the three GOs. A) FT-IR spectra. B) Powder XRD patterns. The numbers in the parentheses are *d*-spacing. The broad feature appeared over 15–35° arises from the silicate-glass sample holder. C) Raman spectra. D) TG-DTA curves. The solid lines describe the weight loss, while the dotted lines correspond to DTA. Positive peaks indicate the occurrence of exothermic reaction.

To investigate the origin of the difference in the thermal behavior, differential spectra were plotted by subtracting a spectrum measured at a lower temperature from one measured at a higher temperature (**Figure 2.2C and 2.2D**). Thus, a downward feature indicates a decrease in intensity, and vice versa. The different spectrum between 60 °C and r.t. showed losses around 3,500 cm^{-1} (O-H stretching) and 1,650 cm^{-1} (H-O-H bending) for both GO-graphite and GO-commercial, indicating the desorption of water. Additionally, GO-graphite exhibited other losses in the fingerprint region (1,232 cm^{-1}, 1,060 cm^{-1}, and 876 cm^{-1}), likely due to the decomposition of epoxy groups as well as C-OH. For the temperature range of 60 to 80 °C in GO-graphite, water desorption and decomposition of epoxy and hydroxyl groups continued, and the baseline curvature steepened significantly. This steepening is attributed to the scattering of the IR beam as the sample became less transparent, likely due to void formation from the release of gaseous byproducts such as CO_2, which might be the cause of the second weight loss at 142 °C in TG-DTA. On the other hand, GO-commercial showed no significant changes between 60 and 80 °C and only showed slight baseline steepening between 80 and 100 °C, which is 20 °C higher compared to GO-graphite. Such differences may correlate to the differences in the weight loss temperatures observed in TG-DTA. Furthermore, the sharp peaks observed

in the fingerprint region (1,263 cm^{-1}, 1,105 cm^{-1}, and 1,024 cm^{-1}) in **Figure 2.1A** did not decrease at all even at 200 °C. These observations indicate that GO-graphite contains a greater quantity of unstable functional groups, which start to decompose below 60 °C, most likely in-plane epoxy, whereas GO-commercial contains a smaller amount of such unstable functional groups. The weight loss at 214 °C and the presence of many sharp peaks at the fingerprint region in the FT-IR spectrum suggest that GO-commercial has a certain quantity of functional groups, which are stable over 200 °C. In fact, it is known that aggregated cyclic esters are much more stable than in-plane epoxy.[40] The I_D/I_G ratio also suggests that GO-graphite contains a larger amount of in-plane functional groups. The presence of more in-plane functional groups increases wrinkling and reduces interlayer π-π interactions, which leads to increasing *d*-spacing. This is consistent with the trends observed in XRD.

On the other hand, GO-GNP exhibited weaker absorption peaks in the FT-IR spectrum for reactive functional groups and displayed a smaller weight loss in TG-DTA from 100 °C to 300 °C, which suggests minimal functionalization despite the expected high surface area of GNP. This minimal functionalization is likely due to particle aggregation. Among the GO samples tested, GO-GNP had the smallest particle size, making it more

prone to aggregation in the highly hydrophilic environment used during the synthesis. This aggregation appears to be random rather than ordered stacking, as indicated by the absence of a 002 peak in the XRD analysis. Consequently, only the outer surfaces of secondary particles were oxidized. This consideration was consistent with the SEM observation (**Figure 2.3**), where GO-GNP particles aggregated into a brick-like morphology, as well as the elemental composition determined by XPS as shown in **Table 2.2**, where GO-GNP had the lowest oxygen content compared to the other two GO samples.

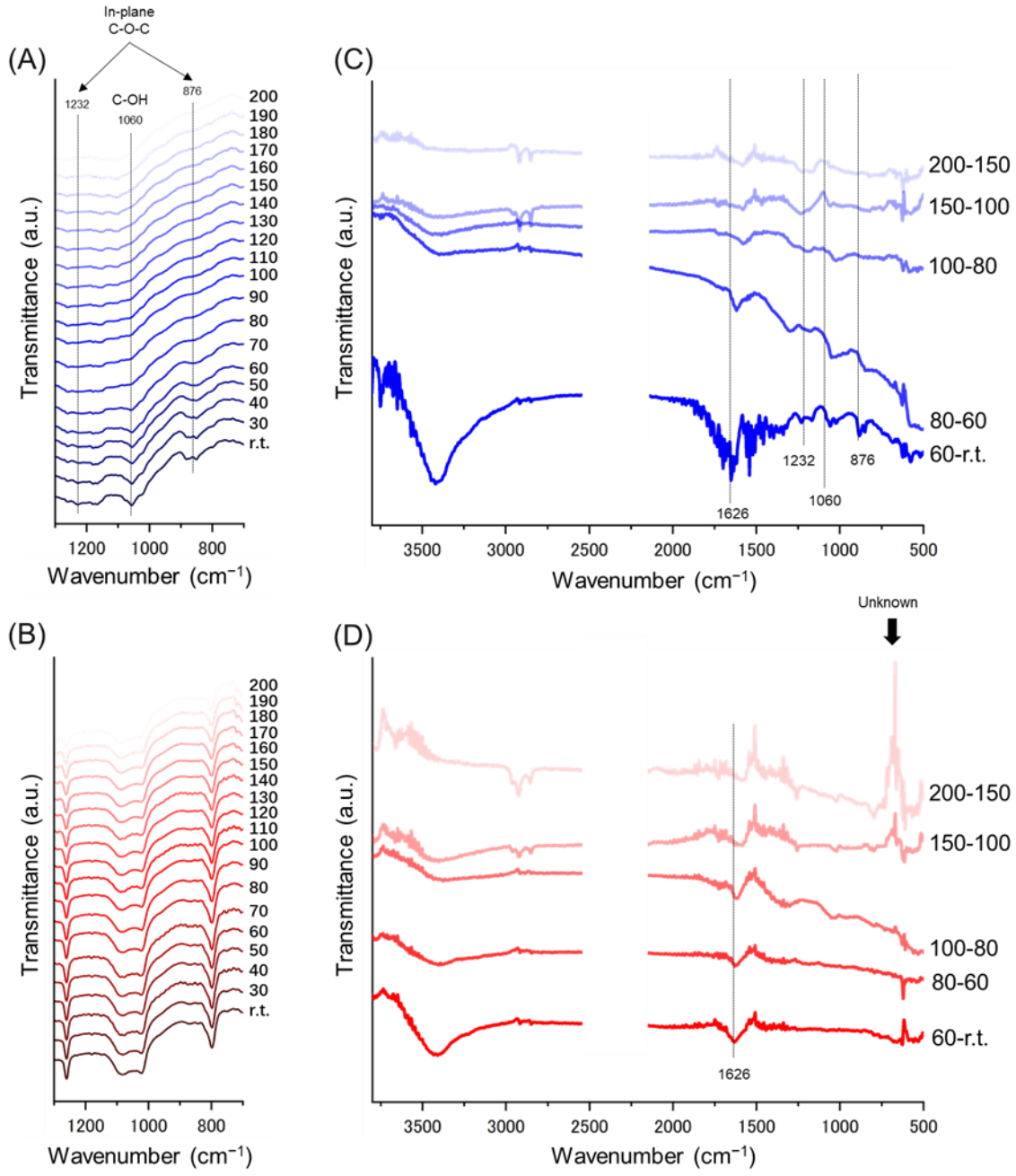

Figure 2.2 In-situ FT-IR spectra with temperature ramping from r.t. to 200 °C under vacuum for A) GO-graphite and B) GO-commercial. All the spectra are offset vertically for clarity. The applied temperature is given in °C on the right side of each spectrum. C) and D) are differential spectra,

where a spectrum measured at a lower temperature was subtracted from that at a higher temperature; thus, a downward feature indicates a decrease in the intensity, and vice versa. The temperature range is shown on the right side of each spectrum.

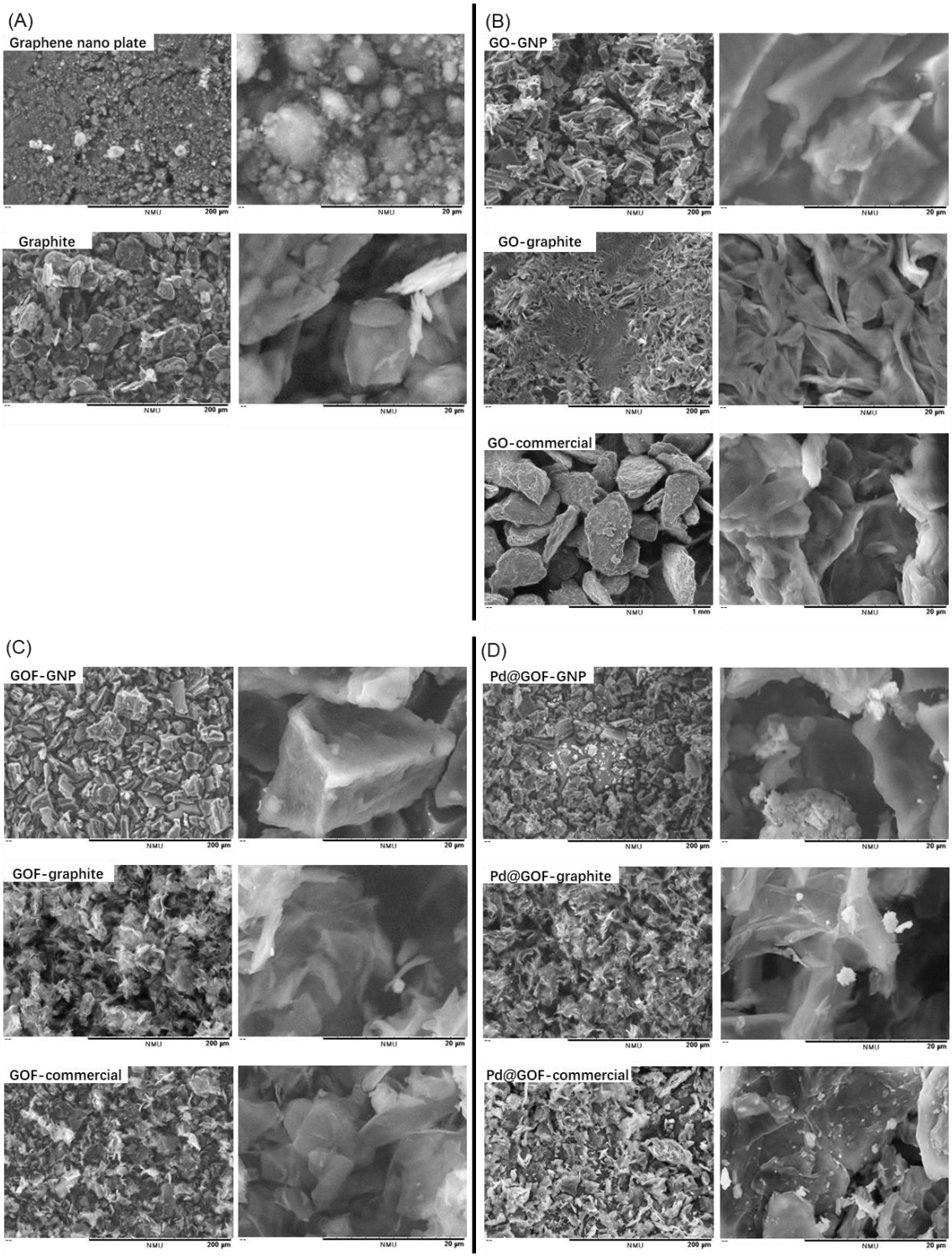
(A)
Graphene nano plate
Graphite
(B)
GO-GNP
GO-graphite
GO-commercial
(C)
GOF-GNP
GOF-graphite
GOF-commercial
(D)
Pd@GOF-GNP
Pd@GOF-graphite
Pd@GOF-commercial

Figure 2.3. SEM images of the prepared samples. A) Carbon materials used for preparation of GO samples, B) GO samples, C) GOF materials, and D) Pd@GOF catalysts.

2.3.2. Characterization of GOFs

GOFs were synthesized by reacting the GOs with PDBA via a solvothermal method. The majority of the reactive functional groups on GO are hydroxyl and epoxy groups, and PDBA is immobilized by the esterification reaction between the boronic acid and the hydroxyl groups.[48] It was reported that the direct ring-opening addition with boronic acid requires a strong acid catalyst such as sulfonic acid[49]; therefore, in the current reaction condition, majority of epoxy groups are believed to react with PDBA after hydrolysis mediated by the residual water.

In order to investigate the extent of functionalization and the structural changes, multifaceted characterization was applied to the GOFs (**Figure 2.4**). **Figure 2.4A** shows the FT-IR spectra. GOF-graphite exhibited an intense absorption peak at 1,320 cm^{-1} due to B-O bonds and at 1,120 cm^{-1} due to O-C bond of boronic ester groups (B-O-C), indicating successful reaction with PDBA. The FT-IR spectrum of GOF-commercial also exhibited the peak of B-O bonds with a lower intensity, and that of GOF-GNP had almost no peak,

which probably reflects lower quantities of PDBA linkers. This qualitative observation matched with the XPS elemental analysis results, showing that the GOF-graphite had a higher B content (2.4 wt%) than GOF-commercial and GOF-GNP (1.9 and 0.8 wt%) (**Table 2.2**). The disappearance of the epoxy peaks in the FT-IR spectrum of GOF-graphite indicates that the epoxy groups were decomposed and/or consumed by PDBA functionalization. On the other hand, GOF-commercial still exhibited the same sharp peaks in the fingerprint region as GO-commercial at 1,263 cm^{-1}, 1,105 cm^{-1}, and 1,024 cm^{-1}, suggesting that these chemical moieties were not involved in the PDBA functionalization. Interestingly, GOF-graphite also exhibited these peaks at lower intensity, which were not present in GO-graphite. This fact suggests that the solvothermal process converted the highly reactive in-plane epoxy groups to more stable functional groups such as ether, which was abundant in GO-commercial. In summary, since such highly reactive functional groups were already lost or hardly formed, GO-GNP and GO-commercial are considered to have a smaller number of PDBA linkers than GO-graphite.

In the XRD patterns (**Figure 2.4B**), both GOF-graphite and GOF-commercial exhibited an expansion of *d*-spacing by about 0.8 Å, which should be due to the intercalation of PDBA. The GOF-GNP also showed a *d*-spacing expansion of about 2 Å, but the intensity of the peak was very

weak. As no B-O peak was observed in FT-IR, this expansion suggests further exfoliation of GO sheets. In the Raman spectra shown in **Figure 2.4C**, all the GOFs showed an increase in the I_D/I_G ratio compared to the GOs. This increase is attributed to the formation of defects induced by the functionalization or removal of functional groups, which is common in reduced GO.[50–52]

Figure 2.4D shows the TG-DTA curves for GOFs. For GOF-graphite, the weight loss with an exothermic peak at 142 °C observed for GO-graphite (**Figure 2.1D**) was no longer present. On the other hand, a weight loss above 200°C was still observed, but it was accompanied by an exotherm. Similarly, for GOF-commercial, the weight loss with a prominent exothermic peak at 214 °C observed for GO-commercial (**Figure 2.1D**) was disappeared, but another weight loss appeared at 243 °C, similar to GOF-graphite. The disappearance of the 142 °C peak in GO-graphite is attributed to the loss of unstable in-plane epoxy groups, while the peak at around 240 °C in GOF-graphite could be attributed to the formation of relatively more stable functional groups, as discussed in the FT-IR results above. The thermal behavior change observed in GOF-commercial from GO-commercial may be due to the functional group consumption by the solvothermal process. GOF-GNP exhibited almost no exothermic weight loss below 300 °C, which is

likely due to the smaller quantity of reactive functional groups compared to the others.

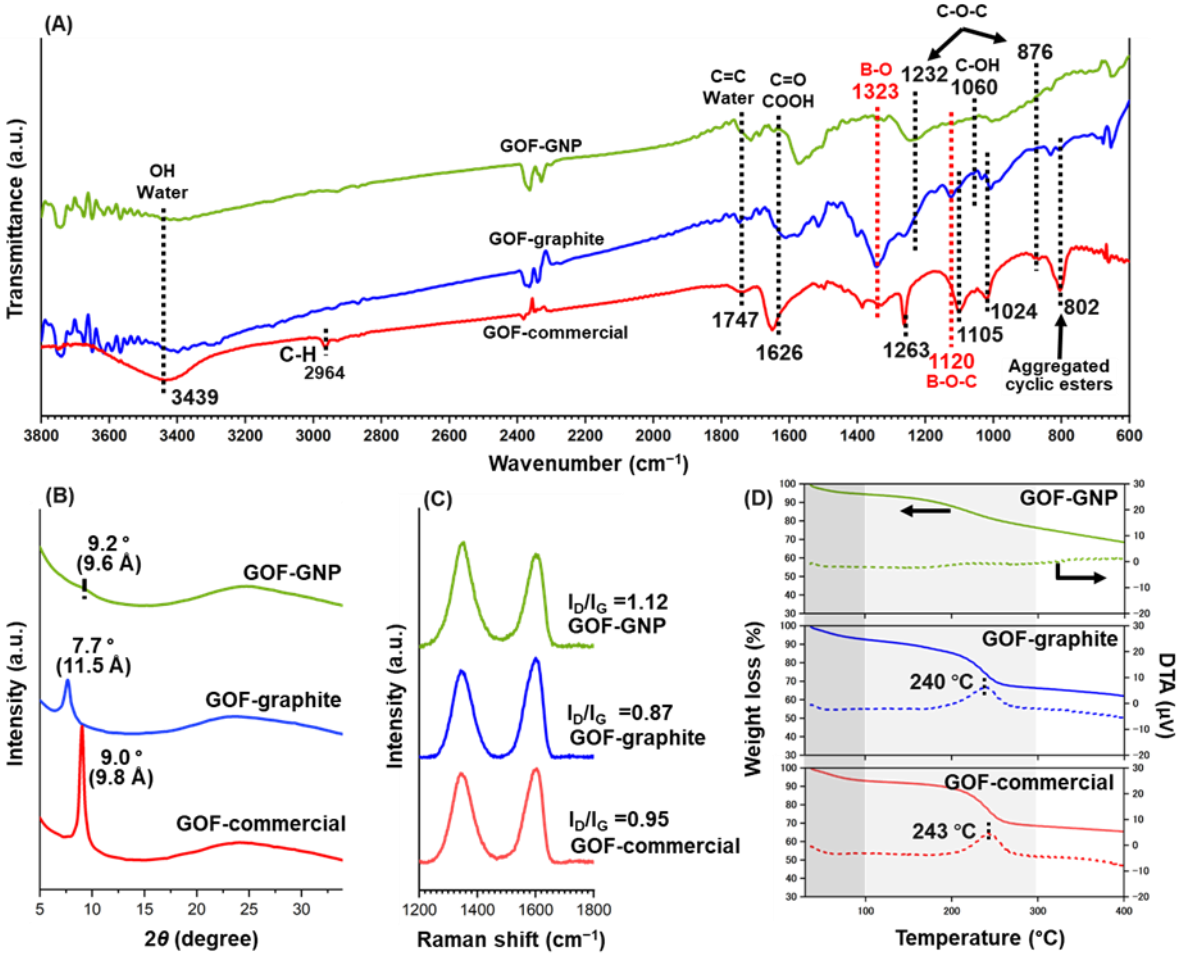

Figure 2.4. Summary of the multifaceted analysis for the three GOFs. A) FT-IR spectra. B) Powder XRD patterns. C) Raman spectra. D) TG-DTA curves.

Table 2.2 Elemental composition determined by XPS.

	C (wt%)	O (wt%)	B (wt%)	Cl (wt%)	Pd (wt%)
GO-GNP	65.5	34.5			
GO-graphite	61.4	38.6			
GO-commercial	62.1	37.9			
GOF-GNP	71.8	27.3	0.84		
GOF-graphite	65.8	31.7	2.41		
GOF-commercial	66.7	31.4	1.91		
Pd@GOF-GNP	54.6	25.6	0.67	5.96	13.2 (12.2/0.95) [a]
Pd@GOF-graphite	60.3	30.8	1.34	2.66	4.9 (4.5/0.38) [a]
Pd@GOF-commercial	52.7	30.4	1.04	5.53	10.3 (9.3/1.00) [a]

[a] The content of Pd(0) and Pd(II) are shown in the parentheses as (Pd(0)/Pd(II)).

2.3.3. Synthesis of supported Pd NP catalysts and performance test

Pd NP catalysts were synthesized using the prepared GOs and GOFs as supports. The Pd NP formation was observed by TEM (**Figure 2.5**). The bar graph shown on the right side of each image is the particle size distribution of Pd NPs calculated from the TEM image. Among the Pd/GOs (**Figures 2.5A–C**), Pd/GO-GNP showed a significantly larger particle size (average diameter = 20.1 ± 8.61 nm) compared to Pd/GO-graphite and Pd/GO-commercial (6.61 ± 2.23 nm and 6.31 ± 2.49 nm). This better dispersion was achieved by the formation of Pd NPs in between the GO sheets. On the other

hand, GO-GNP had almost no such space due to the severe exfoliation, and resulted in the formation of significantly coarse Pd NPs.

Pd@GOFs (**Figure 2.5A'–C'**) tended to exhibit smaller and highly distributed Pd NPs compared to Pd/GOs. Specifically, the median diameter of Pd NPs in Pd@GOF-graphite was about 2 nm smaller than those in Pd/GO-graphite, and Pd@GOF-commercial also exhibited Pd NPs with a smaller diameter than Pd/GO-commercial. This is because the covalently bonded PDBA pillars made the gallery space more rigid, controlling the growth of Pd NPs. Pd@GOF-GNP also showed better Pd NP dispersion than Pd/GO-GNP even though it has almost no gallery spaces. It can be speculated that exfoliation occurred in the formation of GOF-GNP to create a confinement space in which the Pd NPs are entrapped.

To quantify the uniformity of Pd NP dispersion, we calculated a dispersion index (*D*) using the Delaunay–Voronoi tessellation method, implemented via the Delaunay–Voronoi plugin in ImageJ.[40–42] The calculated values are given in **Figure 2.5**. A higher value of *D* indicates a more uniform and evenly spaced distribution of particles. Among the analyzed samples, most exhibited relatively uniform dispersion, as reflected by similar *D* values. However, Pd/GO-GNP and Pd@GO-GNP showed

noticeably lower dispersion uniformity, suggesting a more heterogeneous distribution of Pd NPs on these supports.

As shown in **Table 2.2**, The Pd loading of Pd@GOF-graphite is consistent with the previous reports,[29,31] but the other two catalysts exhibited 2.1–2.7 times higher loading. This difference in Pd loading is expected to be due to coarse Pd particles deposited on the outer surface. The presence of such coarse Pd particles can be confirmed by SEM images as white spots (**Figure 2.3**). The results of XRD and Raman analysis after Pd NP formation are shown in **Figure 2.6**. The XPS elemental analysis (**Table 2.2**) showed a decrease in B content in Pd@GOF-graphite and Pd@GOF-commercial, indicating that some of the linkers were lost in the process of $PdCl_2$ reduction.

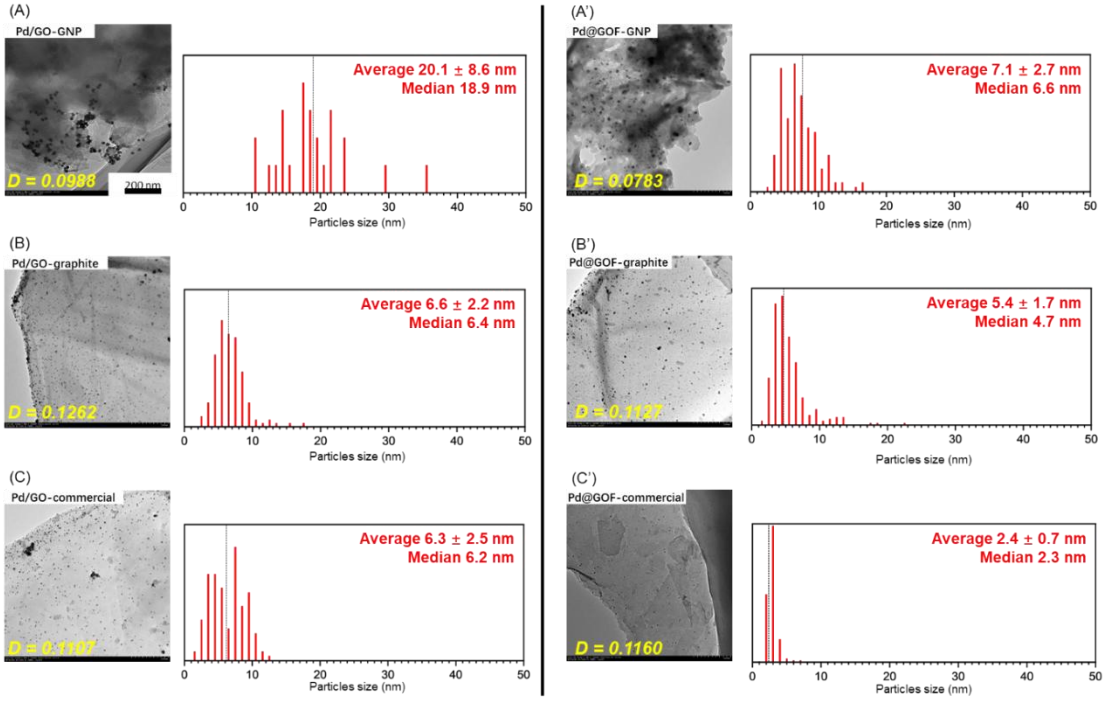

Figure 2.5 TEM images for the A‑C) Pd/GOs and A'–C') Pd@GOFs. The particle size distribution of Pd NPs is shown on the right side of each image. The particle size was determined by analyzing randomly selected 200 particles at the fixed magnification using ImageJ software.[42] The dispersion index (*D*) given in each figure is calculated by the Delaunay–Voronoi plugin in ImageJ software.[40–42] See the Experimental Section for calculation details. The images and graphes A-C) were reproduced from ref 53. Available under a CC-BY 4.0 license. Copyright 2024 Sathiyan et al.

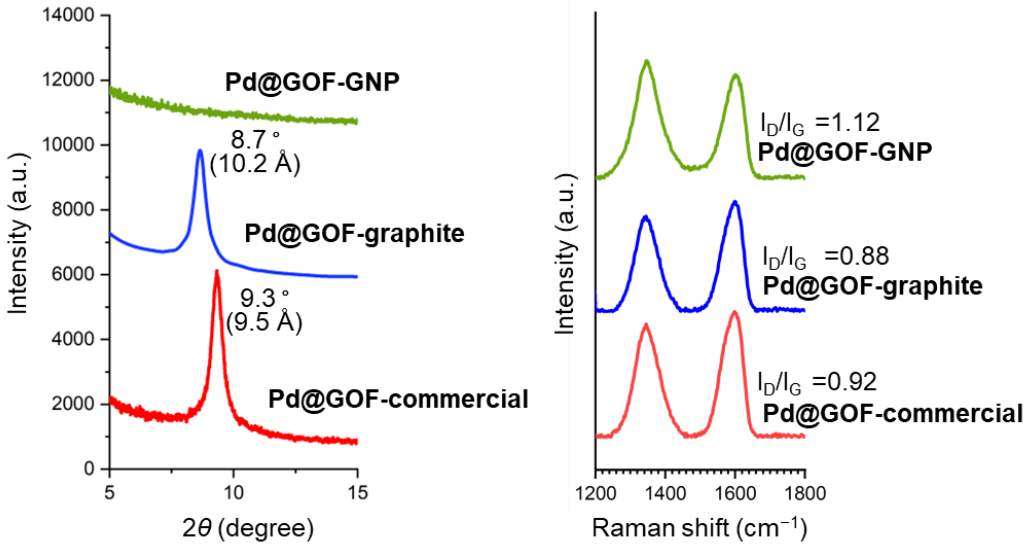

Figure 2.6. XRD patterns and Raman spectra of Pd@GOF catalyst samples.

Figure 2.7 displays the catalytic performance and recyclability results of Pd/GOs and Pd@GOFs in the Suzuki-Miyaura coupling reaction. For the initial reaction with fresh catalysts, all the Pd/GOs achieved a 70–80% yield but showed a significant reduction to approximately 30% in the second cycle, and showed further decrease to 20% by the fifth cycle. As previously reported,[29,31] the yield reduction is most likely due to sintering and leaching of Pd NPs. On the other hand, Pd@GOFs showed a higher initial yield of over 90%, with Pd@GOF-GNP and Pd@GOF-graphite retaining yields of 55% and 45% at the fifth cycle of the reaction, respectively. Note that Pd@GOF-graphite exhibited the superior recyclability despite having the

lower Pd loading among the Pd@GOFs. Interestingly, Pd@GOF-commercial showed a much greater yield reduction, reaching approximately 5% by the fifth cycle, which is even lower than Pd/GO-commercial.

In consideration of the possibility that the GOF itself might influence the catalytic properties, three GOFs without Pd loading were subjected to the same reaction conditions. In all cases, no reaction proceeded at all. Therefore, it was confirmed that Pd is clearly involved in the coupling reaction, and that the aggregation and leaching of Pd NPs are the main causes of the loss in catalytic activity.

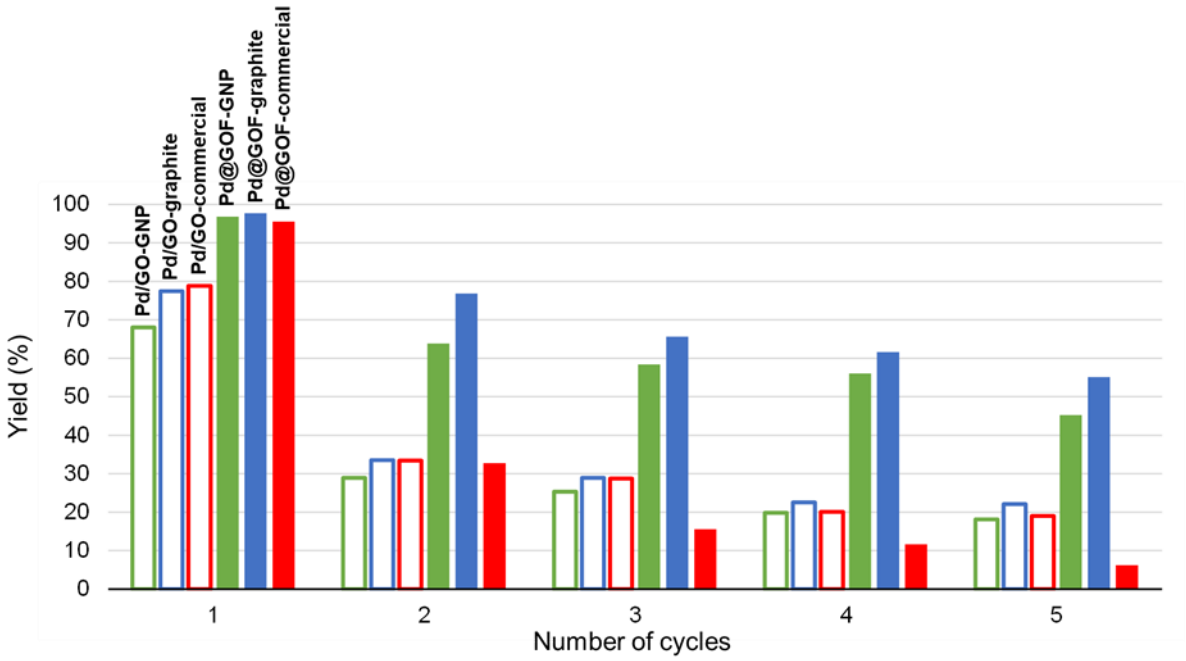

Figure 2.7 Catalytic performance and recyclability of the Pd NP catalysts in Suzuki-Miyaura coupling reaction of bromobenzene and phenylboronic acid.

To understand the cause of the yield reduction, TEM observation of the Pd@GOFs after the fifth cycle reaction was conducted (**Figure 2,8A-C).** It can be seen that Pd@GOF-graphite retained its initial dispersion state well. Conversely, Pd@GOF-commercial experienced a significant deterioration in dispersion, where Pd NPs, which are smaller than 10 nm, became nearly undetectable, indicating that both sintering and leaching occurred. The difference in the NP retention is very likely attributed to the difference in the density of PDBA linkers. The rigid confined spaces formed by the covalently linked PDBA linkers suppressed the leaching and sintering of Pd NPs. As discussed earlier, GOF-graphite had the largest amount of PDBA linkers among the GOFs, driven by the largest amount of in-plane reactive functional groups in GO-graphite. This leads us to conclude that the most critical property of GO as a material for metal NP catalysts support is the amount of in-plane reactive functional groups that serve as anchor points for linker molecules. For Pd@GOF-GNP, numerous coarse Pd NPs were observed, indicating significant sintering of Pd NPs; however, the resulting coarse Pd NPs were not leached out, being entrapped in the random aggregation of

GOF-GNP particles. Although NP leaching might be prevented, sintering was not suppressed due to the larger confinement spaces compared to GO-graphite, which is disadvantageous from the viewpoint of surface area reduction.

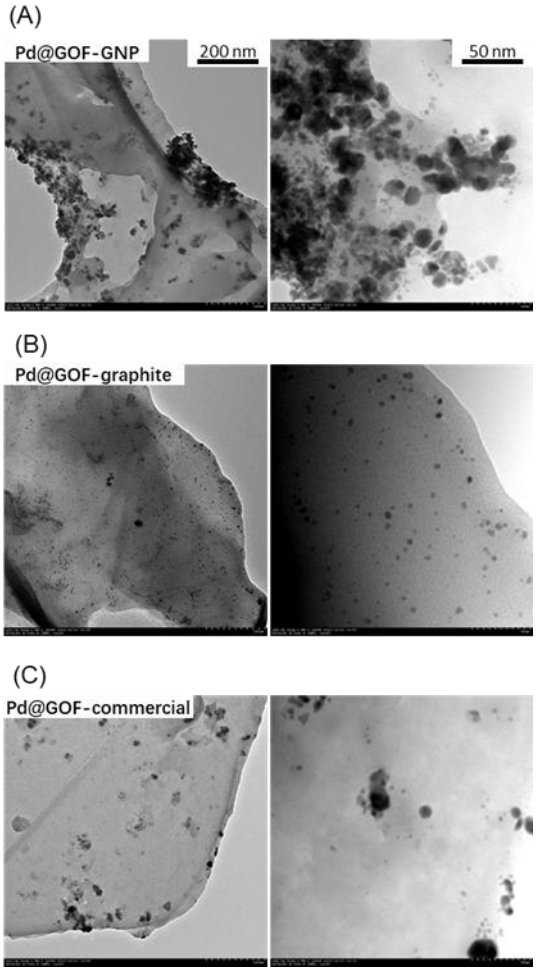

Figure 2.8 TEM images for the Pd@GOFs after 5 cycle reactions.

In order to investigate the impact of the lateral dimension of the GO sheets, an additional Pd@GOF was prepared from graphite powder with a

larger particle size (< 150 μm), which will be referred to Pd@GOF-graphite-larger. As shown in the **Figure 2.9**, the GO and GOF are almost identical in thermal characteristics and functional groups, and thus only difference is the lateral dimension. Its catalytic recyclability was almost the same as that of Pd@GOF-graphite (**Figure 2.10**). Thus, it was concluded that at least this degree of difference (45 to 150 μm) in lateral dimension only makes a negligible difference for the diffusion of reactants and products.

Finally, to explicitly demonstrate the excellent confinement effect of the Pd@GOF catalyst, we compared its performance with that of a commercially available Pd catalyst supported on activated carbon (Pd/C), as shown in **Figure 2.10**. The commercial Pd/C catalyst exhibited a significant decline in yield, dropping to 17% after five reaction cycles. These results indicate that a properly prepared GOF support can effectively suppress Pd leaching while maintaining sufficient accessibility to the Pd NPs.

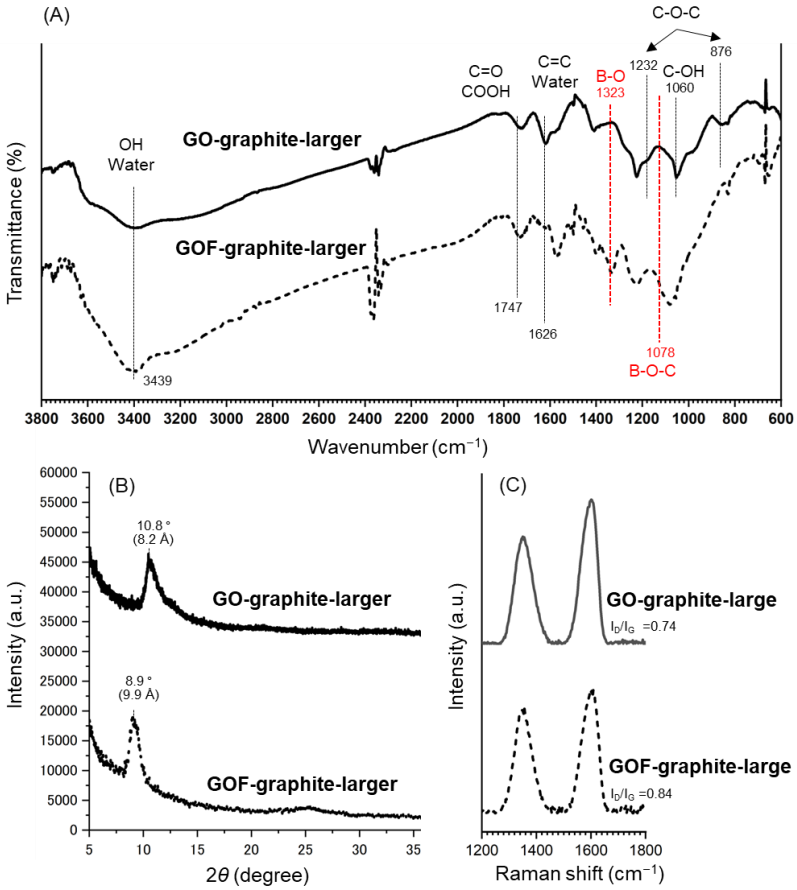

Figure 2.9. Characterization for GO-graphite-larger and GOF-graphite-larger. A) FT-IR spectra. B) Powder XRD patterns. C) Raman spectra.

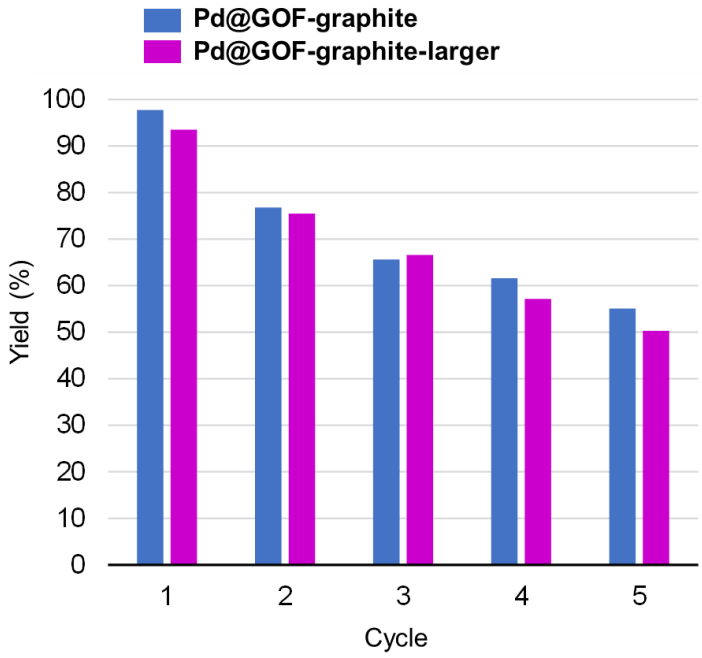

Figure 2.10. Catalytic recyclability of Pd@GOF-graphite and Pd@GOF-graphite-larger.

2.4. Conclusions

This study identified key properties of GO that determine the performance of GOFs as supports for Pd NP catalysts. We found that the density of in-plane reactive functional groups in GO critically affects the recyclability of Pd@GOF catalysts. These functional groups are prone to decomposition even under mild conditions, emphasizing the importance of using freshly prepared GO and optimizing reaction conditions to preserve

reactivity. In contrast, GOs from commercial sources may lose reactivity during storage or transport. Additionally, while the lateral size of GO sheets showed limited impact on performance, sufficient gallery spacing is essential for effective Pd dispersion. These findings highlight the critical role of GO quality in determining GOF performance and suggest that multifaceted characterization of GO is essential for advancing both fundamental studies and practical applications.

References

(1) Zheng, N.; Stucky, G. D. A General Synthetic Strategy for Oxide-Supported Metal Nanoparticle Catalysts. *J. Am. Chem. Soc.* **2006**, *128* (44), 14278–14280. https://doi.org/10.1021/ja0659929.

(2) Gao, C.; Lyu, F.; Yin, Y. Encapsulated Metal Nanoparticles for Catalysis. *Chem. Rev.* **2021**, *121* (2), 834 – 881. https://doi.org/10.1021/acs.chemrev.0c00237.

(3) Zhan, W.-W.; Zhu, Q.-L.; Xu, Q. Dehydrogenation of Ammonia Borane by Metal Nanoparticle Catalysts. *ACS Catal.* **2016**, *6* (10), 6892–6905. https://doi.org/10.1021/acscatal.6b02209.

(4) Ma, Y.; Chen, Y. Three-Dimensional Graphene Networks: Synthesis, Properties and Applications. *Natl. Sci. Rev.* **2015**, *2* (1), 40 – 53. https://doi.org/10.1093/nsr/nwu072.

(5) Liu, J.; Hu, G.; Yang, Y.; Zhang, H.; Zuo, W.; Liu, W.; Wang, B. Rational Synthesis of Pd Nanoparticle-Embedded Reduced Graphene Oxide Frameworks with Enhanced Selective Catalysis in Water. *Nanoscale* **2016**, *8* (5), 2787–2794. https://doi.org/10.1039/C5NR07835K.

(6) Li, C.-J.; Xu, G.-R.; Zhang, B.; Gong, J. R. High Selectivity in Visible-Light-Driven Partial Photocatalytic Oxidation of Benzyl Alcohol into Benzaldehyde over Single-Crystalline Rutile TiO2 Nanorods. *Appl. Catal. B Environ.* **2012**, *115 – 116*, 201 – 208. https://doi.org/10.1016/j.apcatb.2011.12.003.

(7) Zhang, L.; Shi, G. Preparation of Highly Conductive Graphene Hydrogels for Fabricating Supercapacitors with High Rate Capability. *J. Phys. Chem. C* **2011**, *115* (34), 17206 – 17212. https://doi.org/10.1021/jp204036a.

(8) Yang, X.; Zhu, J.; Qiu, L.; Li, D. Bioinspired Effective Prevention of Restacking in Multilayered Graphene Films: Towards the Next Generation of High-Performance Supercapacitors. *Adv. Mater.* **2011**, *23* (25), 2833–2838. https://doi.org/10.1002/adma.201100261.

(9) Tang, Z.; Shen, S.; Zhuang, J.; Wang, X. Noble-Metal-Promoted Three-Dimensional Macroassembly of Single-Layered Graphene Oxide. *Angew. Chem. Int. Ed.* **2010**, *49* (27), 4603 – 4607. https://doi.org/10.1002/anie.201000270.

(10) Hu, C.; Zhai, X.; Zhao, Y.; Bian, K.; Zhang, J.; Qu, L.; Zhang, H.; Luo, H. Small-Sized PdCu Nanocapsules on 3D Graphene for High-Performance Ethanol Oxidation. *Nanoscale* **2014**, *6* (5), 2768 – 2775. https://doi.org/10.1039/C3NR05722D.

(11) Wang, X.; Lu, L.; Yu, Z.; Xu, X.; Zheng, Y.; Yu, S. Scalable Template Synthesis of Resorcinol – Formaldehyde/Graphene Oxide Composite Aerogels with Tunable Densities and Mechanical Properties. *Angew. Chem. Int. Ed*. **2015**, *54* (8), 2397–2401. https://doi.org/10.1002/anie.201410668.

(12) Srinivas, G.; Burress, J. W.; Ford, J.; Yildirim, T. Porous Graphene Oxide Frameworks: Synthesis and Gas Sorption Properties. *J. Mater. Chem*. **2011**, *21* (30), 11323–11329. https://doi.org/10.1039/C1JM11699A.

(13) Qu, H.; Huang, L.; Han, Z.; Wang, Y.; Zhang, Z.; Wang, Y.; Chang, Q.; Wei, N.; Kipper, M. J.; Tang, J. A Review of Graphene-Oxide/Metal–Organic Framework Composites Materials: Characteristics, Preparation and Applications. *J. Porous Mater.* **2021**, *28* (6), 1837 – 1865. https://doi.org/10.1007/s10934-021-01125-w.

(14) Liu, F.; Zhang, L.; Wang, L.; Zhao, B.; Wu, W. Graphene Oxide for Electronics. In Oxide Electronics; *John Wiley & Sons, Ltd,* **2021**; pp 1–19. https://doi.org/10.1002/9781119529538.ch1.

(15) Kamat, P. V. Graphene-Based Nanoarchitectures. Anchoring Semiconductor and Metal Nanoparticles on a Two-Dimensional Carbon Support. *J. Phys. Chem. Lett.* **2010**, *1* (2), 520 – 527. https://doi.org/10.1021/jz900265j.

(16) Sun, Y.; Tang, J.; Zhang, K.; Yuan, J.; Li, J.; Zhu, D.-M.; Ozawa, K.; Qin, L.-C. Comparison of Reduction Products from Graphite Oxide and Graphene Oxide for Anode Applications in Lithium-Ion Batteries and Sodium-Ion Batteries. *Nanoscale* **2017**, *9* (7), 2585 – 2595. https://doi.org/10.1039/C6NR07650E.

(17) Zięba, W.; Jurkiewicz, K.; Burian, A.; Pawlyta, M.; Boncel, S.; Szymańśki, G. S.; Kubacki, J.; Kowalczyk, P.; Krukiewicz, K.; Furuse, A.; Kaneko, K.; Terzyk, A. P. High-Surface-Area Graphene Oxide for Next-Generation Energy Storage Applications. ACS Appl. *Nano Mater.* **2022**, *5* (12), 18448–18461. https://doi.org/10.1021/acsanm.2c04281.

(18) Burress, J. W.; Gadipelli, S.; Ford, J.; Simmons, J. M.; Zhou, W.; Yildirim, T. Graphene Oxide Framework Materials: Theoretical Predictions

and Experimental Results. Angew. *Chem. Int. Ed.* **2010**, *49* (47), 8902–8904. https://doi.org/10.1002/anie.201003328.

(19) Kumar, R.; Suresh, V. M.; Maji, T. K.; Rao, C. N. R. Porous Graphene Frameworks Pillared by Organic Linkers with Tunable Surface Area and Gas Storage Properties. *Chem. Commun.* **2014**, *50* (16), 2015 – 2017. https://doi.org/10.1039/C3CC46907G.

(20) Cote, A. P.; Benin, A. I.; Ockwig, N. W.; O'Keeffe, M.; Matzger, A. J.; Yaghi, O. M. Porous, Crystalline, Covalent Organic Frameworks. *Science* **2005**, *310* (5751), 1166-1170. https://doi.org/10.1126/science.1120411.

(21) Chan, Y.; Hill, J. M. Hydrogen Storage inside Graphene-Oxide Frameworks. *Nanotechnology* **2011**, *22* (30), 305403. https://doi.org/10.1088/0957-4484/22/30/305403.

(22) Yang, L.; Xiao, X.; Shen, S.; Lama, J.; Hu, M.; Jia, F.; Han, Z.; Qu, H.; Huang, L.; Wang, Y.; Wang, T.; Ye, Z.; Zhu, Z.; Tang, J.; Chen, J. Recent Advances in Graphene Oxide Membranes for Nanofiltration. *ACS Appl. Nano Mater*. **2022**, *5* (3), 3121 – 3145. https://doi.org/10.1021/acsanm.1c04469.

(23) Mi, B. Graphene Oxide Membranes for Ionic and Molecular Sieving. *Science* **2014**, *343* (6172), 740 – 742. https://doi.org/10.1126/science.1250247.

(24) Li, G.; Shi, L.; Zeng, G.; Li, M.; Zhang, Y.; Sun, Y. Sharp Molecular-Sieving of Alcohol−Water Mixtures over Phenyldiboronic Acid Pillared Graphene Oxide Framework (GOF) Hybrid Membrane. *Chem. Commun.* **2015**, *51* (34), 7345–7348. https://doi.org/10.1039/C5CC00924C.

(25) Yuan, B.; Wang, M.; Wang, B.; Yang, F.; Quan, X.; Tang, C. Y.; Dong, Y. Cross-Linked Graphene Oxide Framework Membranes with Robust Nano-Channels for Enhanced Sieving Ability. *Environ. Sci. Technol.* **2020**, *54* (23), 15442–15453. https://doi.org/10.1021/acs.est.0c05387.

(26) Li, M.; Wang, J.; Jiao, C.; Wang, C.; Wu, Q.; Wang, Z. Graphene Oxide Framework: An Adsorbent for Solid Phase Extraction of Phenylurea Herbicides from Water and Celery Samples. *J. Chromatogr. A* **2016**, *1469*, 17–24. https://doi.org/10.1016/j.chroma.2016.09.056.

(27) Li, Y.; Xu, X.; Guo, H.; Bian, Y.; Li, J.; Zhang, F. Magnetic Graphene Oxide−based Covalent Organic Frameworks as Novel Adsorbent for Extraction and Separation of Triazine Herbicides from Fruit and Vegetable Samples. *Anal. Chim. Acta* **2022**, *1219*, 339984. https://doi.org/10.1016/j.aca.2022.339984.

(28) Shekarizadeh, A.; Azadi, R. Synthesis of Pd@graphene Oxide Framework Nanocatalyst with Enhanced Activity in Heck-Mizoroki Cross-

Coupling Reaction. *Appl. Organomet. Chem.* **2020**, *34* (9), e5775. https://doi.org/10.1002/aoc.5775.

(29) Tran, T. P. N.; Thakur, A.; Trinh, D. X.; Dao, A. T. N.; Taniike, T. Design of Pd@graphene Oxide Framework Nanocatalyst with Improved Activity and Recyclability in Suzuki-Miyaura Cross-Coupling Reaction. *Appl. Catal. Gen.* **2018**, *549*, 60 – 67. https://doi.org/10.1016/j.apcata.2017.09.026.

(30) Seenivasan, K.; Tran, T. P. N.; Mohan, P.; Ton, N. N. T.; Thakur, A.; Chammingkwan, P.; Rawat, D. S.; Taniike, T. Graphene Oxide Framework-Confined Ru (ru@GOF) as Recyclable Catalyst for Hydrogenation of Levulinic Acid into γ-Valerolactone with Formic Acid. *J. Mater. Sci.* **2022**, *57* (25), 11714–11724. https://doi.org/10.1007/s10853-022-07340-3.

(31) Tran, T. P. N.; Nguyen, T. N.; Taniike, T.; Nishimura, S. Tailoring Graphene Oxide Framework with N- and S- Containing Organic Ligands for the Confinement of Pd Nanoparticles towards Recyclable Catalyst Systems. *Catal. Lett.* **2021**, *151* (1), 247–254. https://doi.org/10.1007/s10562-020-03284-y.

(32) Afrin, S.; Khan, M. W.; Haque, E.; Ren, B.; Ou, J. Z. Recent Advances in the Tuning of the Organic Framework Materials – The Selections of

Ligands, Reaction Conditions, and Post-Synthesis Approaches. *J. Colloid Interface Sci.* **2022**, *623*, 378–404. https://doi.org/10.1016/j.jcis.2022.05.026.

(33) Dimiev, A. M.; Tour, J. M. Mechanism of Graphene Oxide Formation. *ACS Nano* **2014**, *8* (3), 3060–3068. https://doi.org/10.1021/nn500606a.

(34) Sun, L. Structure and Synthesis of Graphene Oxide. *Chin. J. Chem. Eng.* **2019**, *27* (10), 2251–2260. https://doi.org/10.1016/j.cjche.2019.05.003.

(35) Sun, L.; Fugetsu, B. Mass Production of Graphene Oxide from Expanded Graphite. *Mater. Lett.* **2013**, *109*, 207 – 210. https://doi.org/10.1016/j.matlet.2013.07.072.

(36) Lavin-Lopez, M. P.; Patón-Carrero, A.; Muñoz-Garcia, N.; Enguilo, V.; Valverde, J. L.; Romero, A. The Influence of Graphite Particle Size on the Synthesis of Graphene-Based Materials and Their Adsorption Capacity. *Colloids Surf. Physicochem. Eng. Asp.* **2019**, *582*, 123935. https://doi.org/10.1016/j.colsurfa.2019.123935.

(37) Radoń, A.; Włodarczyk, P.; Łukowiec, D. Structure, Temperature and Frequency Dependent Electrical Conductivity of Oxidized and Reduced Electrochemically Exfoliated Graphite. *Phys. E Low-Dimens. Syst. Nanostructures* **2018**, *99*, 82 – 90. https://doi.org/10.1016/j.physe.2018.01.025.

(38) Guo, S.; Garaj, S.; Bianco, A.; Ménard-Moyon, C. Controlling Covalent Chemistry on Graphene Oxide. *Nat. Rev. Phys.* **2022**, *4* (4), 247–262. https://doi.org/10.1038/s42254-022-00422-w.

(39) Hummers, W. S.; Offeman, R. E. Preparation of Graphitic Oxide. *J. Am. Chem. Soc.* **1958**, *80* (6), 1339 – 1339. https://doi.org/10.1021/ja01539a017.

(40) Glaskova, T.; Zarrelli, M.; Borisova, A.; Timchenko, K.; Aniskevich, A.; Giordano, M. Method of quantitative analysis of filler dispersion in composite systems with spherical inclusions, *Comp. Sci. Tech.* **2011**, *71*, 1543–1549. https://doi.org/10.1016/j.compscitech.2011.06.009.

(41) Glaskova, T.; Zarrelli, M.; Aniskevich, A.; Giordano, M.; Trinkler, L.; Berzina, B. Quantitative optical analysis of filler dispersion degree in MWCNT – epoxy nanocomposite, *Comp. Sci. Tech.* **2012**, *72*, 477-481. https://doi.org/10.1016/j.compscitech.2011.11.029.

(42) Schneider, C. A.; Rasband, W. S.; Eliceiri, K. W. NIH Image to ImageJ: 25 Years of Image Analysis. *Nat. Methods* **2012**, *9* (7), 671–675. https://doi.org/10.1038/nmeth.2089.

(43) Acik, M.; Lee, G.; Mattevi, C.; Chhowalla, M.; Cho, K.; Chabal, Y. J. Unusual Infrared-Absorption Mechanism in Thermally Reduced Graphene Oxide. *Nat. Mater.* **2010**, *9* (10), 840–845. https://doi.org/10.1038/nmat2858.

(44) Zhang, H.; Hines, D.; Akins, D. L. Synthesis of a Nanocomposite Composed of Reduced Graphene Oxide and Gold Nanoparticles. *Dalton Trans* **2014**, *43* (6), 2670–2675. https://doi.org/10.1039/C3DT52573B.

(45) Kuila, A.; Maity, N.; Layek, R. K.; Nandi, A. K. On the pH Sensitive Optoelectronic Properties of Amphiphilic Reduced Graphene Oxide via Grafting of Poly(Dimethylaminoethyl Methacrylate): A Signature of p- and n-Type Doping. *J Mater Chem A* **2014**, *2* (38), 16039 – 16050. https://doi.org/10.1039/C4TA03408B.

(46) Zheng, S.; Tu, Q.; Urban, J. J.; Li, S.; Mi, B. Swelling of Graphene Oxide Membranes in Aqueous Solution: Characterization of Interlayer Spacing and Insight into Water Transport Mechanisms. *ACS Nano* **2017**, *11* (6), 6440–6450. https://doi.org/10.1021/acsnano.7b02999.

(47) Ferrari, A. C.; Robertson, J. Interpretation of Raman Spectra of Disordered and Amorphous Carbon. *Phys. Rev. B* **2000**, *61* (20), 14095–14107. https://doi.org/10.1103/PhysRevB.61.14095.

(48) Haque, E.; Yamauchi, Y.; Malgras, V.; Reddy, K. R.; Yi, J. W.; Hossain, Md. S. A.; Kim, J. Nanoarchitectured Graphene - Organic Frameworks (GOFs): Synthetic Strategies, Properties, and Applications. *Chem. – Asian J.* **2018**, *13* (23), 3561 – 3574. https://doi.org/10.1002/asia.201800984.

(49) Chambhare, S. U.; Lokhande, G. P.; Jagtap, R. N. Design and UV-Curable Behaviour of Boron Based Reactive Diluent for Epoxy Acrylate Oligomer Used for Flame Retardant Wood Coating. *Des. Monomers Polym.* **2017**, *20* (1), 125–135. https://doi.org/10.1080/15685551.2016.1231029.

(50) Khan, M. U.; Shaida, M. A. Reduction Mechanism of Graphene Oxide Including Various Parameters Affecting the C/O Ratio. *Mater. Today Commun.* **2023**, *36*, 106577. https://doi.org/10.1016/j.mtcomm.2023.106577.

(51) Lesiak, B.; Trykowski, G.; Tóth, J.; Biniak, S.; Kövér, L.; Rangam, N.; Stobinski, L.; Malolepszy, A. Chemical and Structural Properties of Reduced Graphene Oxide—Dependence on the Reducing Agent. *J. Mater. Sci.* **2021**, *56* (5), 3738–3754. https://doi.org/10.1007/s10853-020-05461-1.

(52) Sparavigna, A. C. Graphene and Graphene Oxide (Raman Spectroscopy). *ChemRxiv* **2024**. https://doi.org/10.26434/chemrxiv-2024-86stv-v2.

(53) Sathiyan, K.; Gao, C.; Wada, T.; Mukherjee, P.; Seenivasan, K.; Taniike, T. Structure-Driven Performance Enhancement in Palladium – Graphene Oxide Catalysts for Electrochemical Hydrogen Evolution. *Materials* **2024**, *17* (21), 5296. https://doi.org/10.3390/ma17215296.

Chapter 3

Design of Graphene Oxide-Based Palladium Nanocatalysts for Hydrogen Evolution Reaction

Chapter 3

Abstract

Graphene oxide (GO) has recently gained significant attention in electrocatalysis as a promising electrode material owing to its unique physiochemical properties, such as enhanced electron transfers due to a conjugated π-electron system, high surface area, and stable support for loading electroactive species, including metal nanoparticles. However, only a few studies have been directed toward the structural characteristics of GO, elaborating on the roles of oxygen-containing functional groups, the presence of defects, interlayer spacing between the layered structure, and nonuniformity in the carbon skeleton along with their influence on electrochemical performance. In this work, I aim to understand these properties in various GO materials derived from different graphitic sources. Both physiochemical and electrochemical characterization were employed to correlate the above-mentioned features and explore the effect of palladium nanoparticles (Pd NPs) location on various GO supports for hydrogen evolution reaction (HER). The inter-action of the functional groups has a crucial role in the Pd dispersion and its electrochemical performance. Among the different GO samples, Pd supported on GO derived from graphene nanoplate (GNP), Pd/GO-GNP, exhibits superior HER performance. It could be attributed to the optimal balance among particle size, defect density, less

inplane functionalities, and higher electro-chemical surface area. This study thus helps to identify the optimal conditions that lead to the best performance of Pd-loaded GO, contributing to the design of more effective HER electrocatalysts.

Keywords: Graphene oxide; Functional groups; Pd nanoparticle; Electrocatalysts; Hydrogen evolution reaction

Chapter 3

3.1. Introduction

The intellectual catalyst design approach is critical for developing advanced materials and accelerating various catalytic reactions, including those in industrial applications.[1] Among various techniques, particular importance is given to electrochemical water splitting reactions, which create clean, sustainable alternative energy to support the hydrogen economy.[2,3] Water splitting reaction proceeds via two half-cell reactions: H^+ ions get reduced at the cathode (hydrogen evolution reaction, HER), and the water gets oxidized at the anode (oxygen evolution reaction, OER).[4,5] While molecular hydrogen (H_2) is not available naturally, the energy produced is clean and environmentally friendly, gaining its interest in fuel cell technology and prompting researchers to necessitate its production on a large scale.[6] Moreover, hydrogen generated by the electrochemical approach appears to be greener and more sustainable.[7] Platinum (Pt) is considered the benchmark catalyst for HER in acidic media.[8] However, the limited abundance and high cost limit its practical applications.[9–11] To reduce pressure on sole Pt, palladium (Pd), having a good affinity for hydrogen can be an alternative.[12,13] However, the catalytic activity of Pd is lower compared to that of Pt since the Pd-hydrogen system tends to have an internal damage phenomenon due to hydrogen embrittlement that causes microstructural

changes and cracking, thus reducing its mechanical integrity.[14] It requires inert support materials that could stabilize the Pd electrodes. In that direction, if the desired performance is achieved, efforts should still be made to reduce the metal content and maximize the HER performance to compensate for the cost to a techno-economic level and facilitate real-time applications. One of the strategies to address this issue is reducing the nanoparticles (NPs) size and then further decorating them on a high surface area substrate.[15]

Graphene oxide (GO), a derivative of graphene, has various oxygen-containing functional groups, such as hydroxyl, epoxy, carbonyl, and carboxylic groups.[16] These functional groups act as binding sites for the reactants and allow transition metal ions to coordinate, making GO an excellent support candidate.[17,18] The utilization of Pd in its NPs form has the superior benefits of minimal usage while maintaining high catalytic efficiency when supported on GO.[19] This, in turn, makes the catalyst synthesis cost-effective. Electrochemical processes like HER benefit from binding Pd NPs on GO support not only due to uniform coverage of the metal nanoparticle (M-NPs) but also by improving stability.[20,21] GO supports have special advantages over other carbon supports for dispersing M-NPs. For example, typically existing carboxyl groups at the edges of GO sheets can efficiently serve as nucleation sites for Pd.[22] Hence, Pd NPs at higher

concentrations are prone to attach at edge positions. If these groups distribute uniformly on the surface, their interaction can facilitate the anchoring of the Pd NPs, thereby providing a more homogeneous distribution. Likewise, epoxy groups lying on the basal plane of the GO sheet may also act as Pd binding sites.[23] GO supports also allow controlling the degree of oxidation to maintain a balance be-tween the sp^2 hybridized carbon domains (related to conductivity and gas diffusion) and the functional groups introduced during oxidation (for dispersibility and functionalization). In general, the sp^2 hybridized regions of GO are less functionalized and may not provide strong anchoring sites for Pd NPs, resulting in sparser Pd distribution in these areas. Benefitting from the different functional groups attached, the GO has distinct merits: capable of controlling the particle dispersion and morphology, creating more catalytic active sites, and improving the binding between Pd NPs and GO supports for better HER kinetics.[24] However, the actual roles of the functional group, their location (on the edges and/or basal plane), their influence on M-NPs dispersion, and catalytic performance are insufficiently explored, with more focus given to the M-NPs. Besides functional groups, other structural features, like interlayer spacing between the GO sheets and defects (distortion or vacancy), demand careful consideration.

Chapter 3

This work aims to investigate the physiochemical characteristics of a wide series of Pd-loaded GO catalysts resulting from various graphitic sources and explain their HER performance. The results from this research will evidently show a clearer direction in designing effective HER electrocatalysts based on material characteristics and electrochemical behavior.

3.2. Experimental section

3.2.1. Materials

Four variations of GO materials were studied in the current research, among which three of them were reported in my previous publication. The sample codes of the GO materials are summarized in **Table 3.1**. GO-GNP, GO-graphite45, and GO-graphite150 were prepared from graphite sources with different particle sizes. GO-commercial (dry powder, 50–100 mesh) was purchased from Layer One – Advanced Materials. Graphene nanoplatelets (particle size < 2 μm) were purchased from Strem Chemicals. Graphite (particle size > 45 μm, purity > 98%) was purchased from Wako Pure Chemical Industries. Graphite (particle size >150 μm) was supplied by Sigma Aldrich. The details of the synthetic protocols for GO materials are available in the previous publication.[25]

Table 3.1 Sample codes for GO samples.

Carbon material	Sample code
N.A. [a]	GO-commercial
Graphite (> 45 μm)	GO-graphite45
Graphene nanoplatelets (< 2 μm)	GO-GNP
Graphite (> 150 μm)	GO-graphite150

[a] The GO was purchased from a commercial source.

Additionally, a graphene oxide framework (GOF) support was prepared from GO-GNP as a reference sample in the expectation of better dispersion and stabilization of Pd NPs in the confined spaces created by the covalently bonded linker molecules.[26–28] The GOF sample is referred to as GOF-GNP.

A Pd catalyst was synthesized by reducing $PdCl_2$ in the presence of GO and GOF materials in toluene.[26] In this method, the reactive functional groups present on the support were exploited as a reductant. For further details about the protocol, refer to my previous publication.[25] The catalyst where Pd was supported on a GO material is referred to as Pd/GO, and that for GOF-GNP is referred to as Pd@GOF-GNP.

Other reagents including diethyl ether (Wako Pure Chemical Industries), palladium (II) chloride (PdCl2, Sigma Aldrich), 1,4-phenylenediboronic acid

(purity > 95.0%, Sigma Aldrich), hydrogen peroxide (35% aqueous solution, Tokyo Chemical Industry Co., Ltd.), sulfuric acid (H_2SO_4) (Kanto Chemical Co., Inc.), potassium permanganate (Kanto Chemical Co., Inc.), toluene (Kanto Chemical Co., Inc.), methanol (Kanto Chemical Co., Inc.), ethanol (Kanto Chemical Co., Inc.), propanol (Fujifilm Wako Pure Chemical Co.,), 5% Nafion TM dispersion solution DE520 CS type (Fujifilm Wako Pure Chemical Co.,) and 0.3 μm and 0.05 μm alumina (Al_2O_3-Baikowski Co., Inc.), were used without further purification.

3.2.2. Characterization

The FT-IR spectra were acquired using JASCO 6100 (JASCO) in the range of 4,000–400 cm^{-1} with a resolution of 4 cm^{-1} by 16 scans. The sample powder was ground with dried KBr at a weight ratio of 1:50 and then pressed into a pellet. Raman spectra of powder samples dispersed on a glass plate were recorded using a laser Raman spectrometer, NRS-4100 (JASCO), with an excitation wavelength of 532 nm and an expo-sure time of 25 s with 10 acquisitions.

The morphology, particle size, and particle size distribution of the Pd NPs were investigated by TEM using H-7650 (Hitachi) operating at an acceleration voltage of 100 kV. The samples are dispersed in ethanol with

ultrasonication for 15 min, then dropped onto a carbon-coated copper grid and naturally dried overnight. The surface morphology was observed by SEM using TM-3030-plus (Hitachi), with an accelerating voltage of 15 kV. The sample was spread onto a copper tape for the measurement.

XPS was used to investigate the chemical composition and the oxidation state of individual elements. The spectra were recorded on Kratos AXIS Ultra DLD (Shimadzu) equipped with an Al-Kα anode. Powder samples were loaded onto a sample holder using double-sided adhesive copper tape. The survey spectrum was recorded with a 1 eV step size and a pass energy of 80 eV. Narrow scans were recorded with a 0.1 eV step size and a pass energy of 160 eV. The binding energies were calibrated using the C 1s peak of graphitic carbon at 284.6 eV. The sample powder was spread evenly on copper tape, and measurement positions were determined by adjusting the stage position to the location where the C 1s peak of the sample exhibited the highest intensity. The spectra were analyzed using XPSpeak 4.1 software, with baseline correction performed using the Shirley method. The elemental composition was calculated by the area ratio of the detected peaks. Note that the Cu peak was not detected in any of the samples, ruling out the possibility that the observed C and oxygen-containing functional group originated from the copper tape.

3.2.3. Electrochemical measurements

Electrochemical measurements were performed with an electrochemical work-station, HZ-7000, from Meiden Hokuto. The rotation speed was controlled with a rotating electrode device, HR series HR-500, connected to the workstation. A three-electrode cell was used, with a rotating disk electrode (RDE, diameter 5.0 mm and 0.196 cm^2 surface area) as the working electrode, an Ag/AgCl electrode (3.0 M KCl) as the reference, and a graphite rod as the counter electrode. All the experiments were performed at room temperature. Before the electrochemical measurements, the RDE working electrode was polished with 0.3 μm Al_2O_3 to remove any deposited materials, followed by polishing with 0.05 μm Al_2O_3 to make a smooth surface. Then, it was sonicated in water for 30 s using an ultrasonic bath to remove any deposited particles from the surface. 10 mg of catalyst powder was initially dispersed in a mixture containing 1.50 mL of H_2O, Milli-Q water (ultrapure water produced by a Milli-Q purification system, Millipore), 480 μL propanol, and 20 μL Nafion TM binder (5.0 wt%). The solution was ultrasonicated with a bath sonicator for 45 minutes to attain a uniform dispersion, followed by 5 minutes of probe sonication. Finally, 10 μL of the prepared ink was dropcasted on the RDE surface, covered with a vial, and

naturally dried at room temperature. The catalyst loading was set to 0.255 mg cm^{-2}.

3.3. Results and discussion

3.3.1. Characterization

All the GO and Pd/GO samples other than Pd/GO-graphite150 and its support were already characterized in the previous publication,[25] so their differences are briefly explained here. The IR and Raman spectra of the GO samples are shown in **Figure 3.1a, b**. The GO samples prepared in-house (GO-GNP, GO-graphite45, and GO-graphite150) had in-plane functional groups such as epoxy (C-O-C) and hydroxyl (C-OH), while GO-commercial possessed less number of in-plane functional groups but many aggregated cyclic esters. GO-GNP was the most defective due to the presence of many edges and GO-commercial was the least defective due to the largest lateral size of the sheets and the least in-plane functionalization.

Figure 3.1c shows the TEM images of the prepared Pd/GO catalysts together with the particle size distribution of Pd NPs calculated from the image. Pd/GO-GNP showed the largest particle size (average diameter = 20.1 ± 8.6 nm) among the catalyst samples. The reason for the smaller Pd NPs of Pd/GO-graphite45 (6.61 ± 2.2 nm) and Pd/GO-commercial (6.31 ± 2.5 nm)

is probably the formation of Pd NPs in between stacked GO sheets. GO-GNP had almost no such space due to the severe exfoliation, which resulted in the formation of significantly coarse Pd NPs.

The XPS elemental analysis results (**Table 3.2**) show that GO-GNP was less functionalized compared to the other GO supports as it exhibited ca. 3–4 wt% lower oxygen content. This tendency is maintained even after Pd loading. The higher Pd loading of Pd/GO-GNP and Pd/GO-commercial is attributed to the presence of coarse Pd particles deposited on the outer surface.[25]

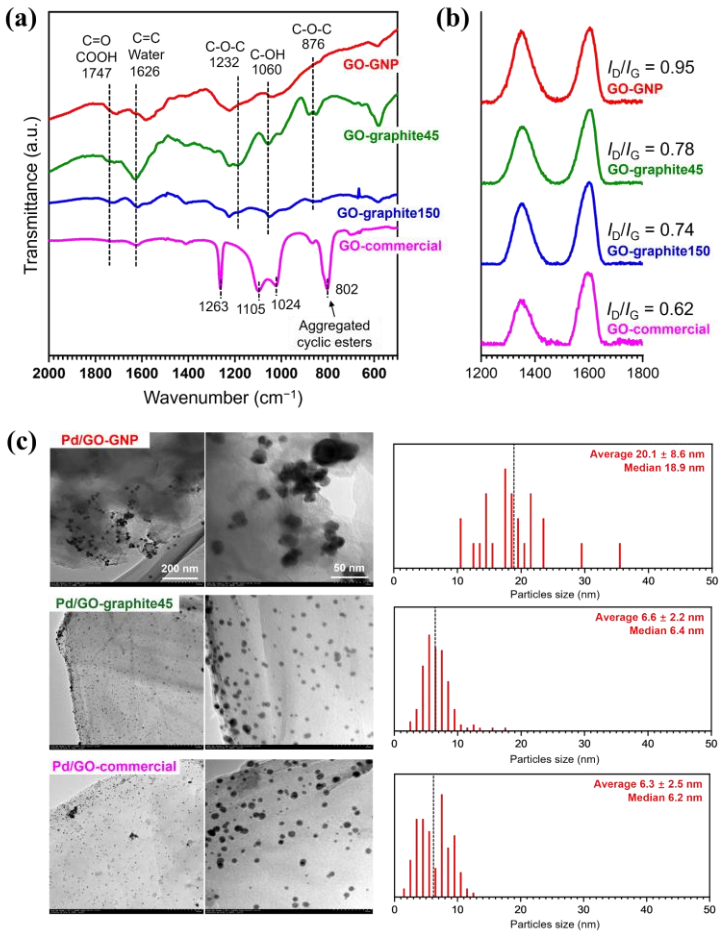

Figure 3.1 Characterization of the GO supports and the relevant Pd catalysts. (a) FT-IR and (b) Raman spectra of the supports. (c) TEM images for the supported Pd catalysts in two different magnifications. The particle size distribution of Pd NPs is shown on the right side of each image. The particle size was determined by analyzing randomly selected 200 particles at the fixed magnification using ImageJ software.[31] The IR and Raman spectra, as well as the TEM images for GO-GNP, GO-graphite45, GO-commercial, and the relevant Pd catalysts, are from my previous publication.[25]

Table 3.2. Elemental composition determined by XPS.

	C (wt%)	O (wt%)	Cl (wt%)	Pd (wt%)
GO-GNP [a]	65.5	34.5		
GO-graphite45 [a]	61.4	38.6		
GO-graphite150	55.9	44.1		
GO-commercial [a]	62.1	37.9		
Pd/GO-GNP [a]	49.7	25.1	8.6	16.7 (16.0/0.6) [b]
Pd/GO-graphite45 [a]	57.1	29.3	4.0	9.7 (8.9/0.7) [b]
Pd/GO-graphite150	45.8	39.6	3.33	11.3 (7.5/3.8) [b]
Pd/GO-commercial [a]	44.1	30.1	8.4	17.5 (15.7/1.7) [b]

a These data are from my previous publication.[25]

b The content of Pd(0) and Pd(II) are shown in the parentheses as (Pd(0)/Pd(II)).

3.3.2. Electrochemical Performance

The HER performances of Pd/GO catalysts were evaluated using the LSV technique with a 1600 rpm rotation speed. The catalytic current at 10 mA cm^{-2} was fixed as the benchmark for comparing the performance of different catalysts. Among all the catalysts, Pd/GO-GNP showed the best catalytic performance for HER with a lower over-potential (143 mV@10mA cm^{-2}) than the others, **Figure 3.2a**. The activity trend followed in the order

of Pd/GO-GNP > Pd/GO-graphite45 > Pd/GO-graphite150 > Pd/GO-commercial. Control experiments were performed using GOs without the Pd loading under identical conditions (**Figure 3.3**). The resultant LSV curves confirmed that no significant activity was brought by GO alone, suggesting that GO itself is less conductive. The improved activity may arise from the combined benefits of Pd NPs and GO support. It can be anticipated that when supported on GO, Pd/GO catalysts exhibit enhanced catalytic performance because of better Pd dispersion and electronic inter-actions with GO and by offering high surface-to-volume ratios, with an increased number of catalytic sites available for reactions.

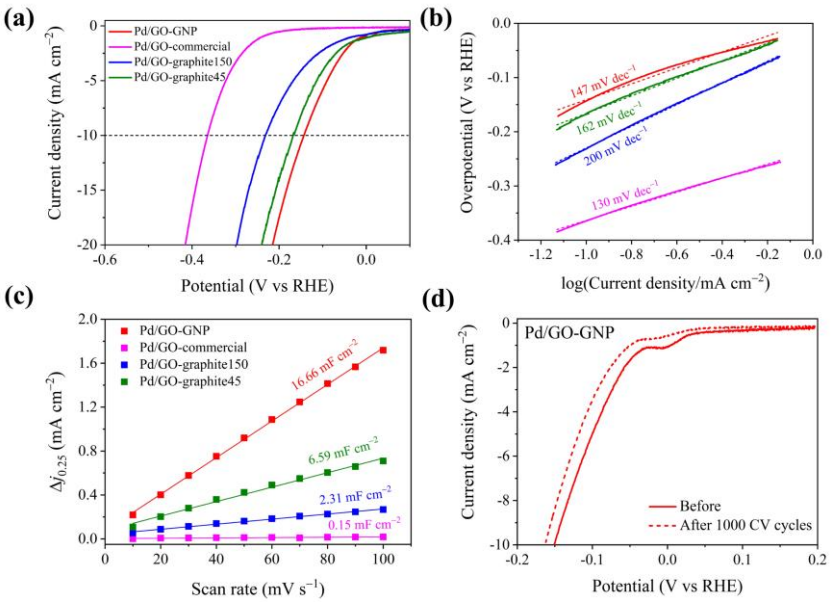

Figure 3.2 Electrocatalytic activity of synthesized catalysts (a) HER polarization curves measured in 0.5 M H2SO4 at 1600 rpm rotation, its corresponding (b)

Tafel plots, (c) C_{dl} plot obtained from the CV (Figure 3.5), (d) durability test: polarization curves obtained before and after 1000 CV cycles at 5 mV s^{-1}scan rate.

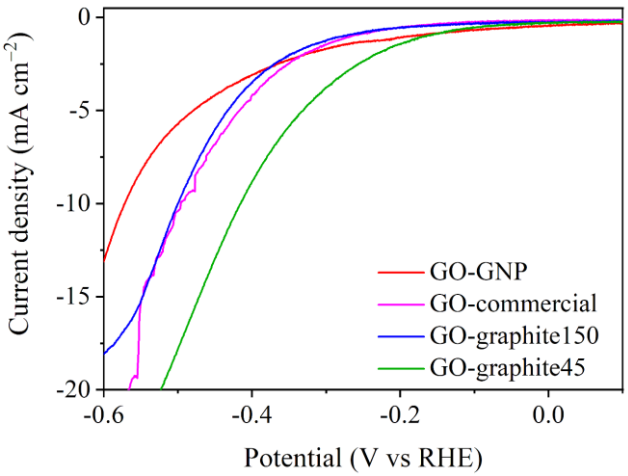

Figure 3.3. HER polarization curves of various GO samples (without Pd) measured in 0.5 M H_2SO_4 at 1600 rpm rotation.

The Tafel slopes obtained from the polarization curves were used to analyze the intrinsic nature of the catalysts. The Pd/GO-GNP had a lower Tafel value (147 mV dec^{-1}) compared to Pd/GO-graphite45 (162 mV dec^{-1}) and Pd/GO-graphite150 (200 mV dec^{-1}), which indicates its faster HER kinetics, **Figure 3.2b**. This, in turn, suggests that electron transfer is more facilitated in Pd/GO-GNP than in other catalysts. Compared to other forms of GO, GO-GNP generally contains fewer in-plane defects, thereby retaining

higher structural integrity, allowing the electron pathways to remain less disrupted and electron transfer to occur more smoothly and efficiently across the material. One possibility is that the interactions between Pd NPs and the GNP surface create an electronically favorable environment, modifying the electronic structure of Pd and thus enhancing its catalytic property to facilitate faster electron transfer. To validate this claim, the EIS technique was used to probe the interfacial electron transfer kinetics of the catalysts. The impedance spectra were represented in a Nyquist plot, **Figure 3.4a**, and fitted with a Randles circuit, R(QR), shown schematically in **Figure 3.4b**. The elements used for fitting and its summarized results were tabulated in **Table 3.3**. The solution resistance (R_s) remains the same for all the catalysts. The charge transfer resistance (R_{ct}) can be easily visualized in **Figure 3.4a**. The smaller the semicircle, the smaller the R_{ct}, and the higher the charge transfer. In other words, R_{ct} is inversely proportional to the current density. Pd/GO-GNP exhibited the lowest R_{ct} value, con-firming the highest conductivity among the tested catalysts. The results are thus consistent with the Tafel plot. The larger particle size of GO and stacking of GO sheets together hinder the electron transfer process in all the Pd-loaded GO catalysts except for Pd/GO-GNP.

Table 3.3. The fitted electrochemical results of the EIS parameters for different catalysts.

Electrocatalysts	R_s	Q	R_{ct}
Pd/GO-GNP	16.56	0.8636	4555
Pd/GO-commercial	16.57	0.8657	6104
Pd/GO-graphite150	16.76	0.8637	5720
Pd/GO-graphite45	16.46	0.8639	4880

R_s is the uncompensated solution resistance.

Q is the constant phase element (CPE) associated with the electrochemical double-layer capacitance at the catalyst | electrolyte interface.

R_{ct} is the charge transfer resistance between the interface of the electrode and electrolyte.

Note: The impedance measurements were performed using a 1 x 1 cm^2 carbon paper substrate as the working electrode with the same catalyst loading normalized relative to the electrode surface area.

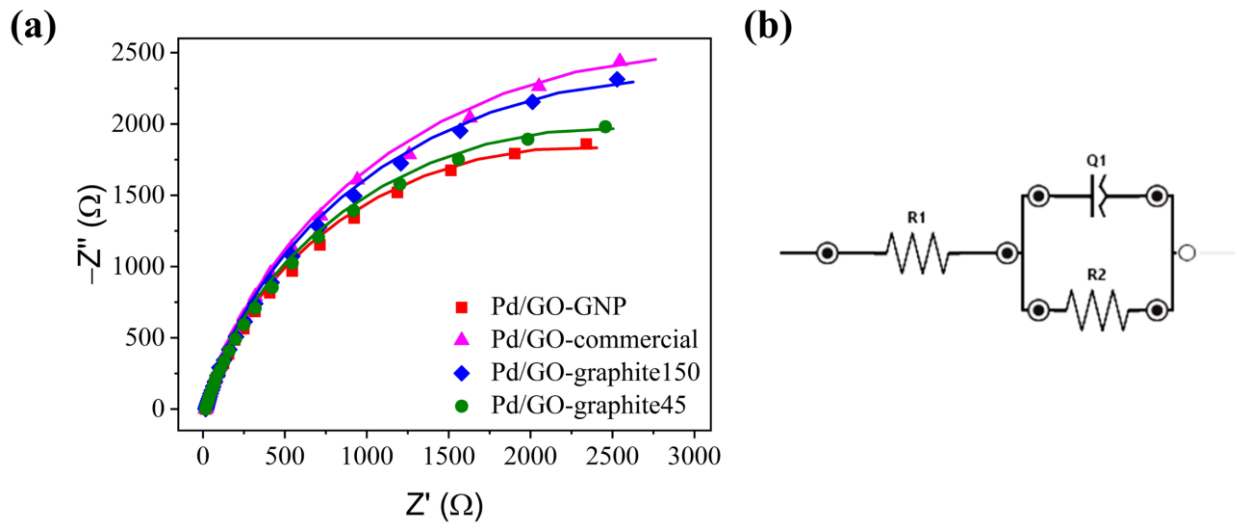

Figure 3.4. (a) Nyquist plot of all the catalysts, and (b) the equivalent circuit model used for the fitting.

The C_{dl} was determined to shed deeper insight into improved performance, giving better knowledge about electrochemically active sites of samples. **Figure 3.2c** shows the C_{dl} values obtained by performing CV at various scan rates (**Figure 3.5**). Among them, Pd/GO-GNP had the largest C_{dl} value of 16.66 mF cm^{-2} compared with Pd/GO-commercial (0.15 mF cm^{-2}), Pd/GO-graphite45 (6.59 mF cm^{-2}), and Pd/GO-graphite150 (2.31 mF cm^{-2}). Since electrochemical surface area (ECSA) is proportional to the C_{dl} values, the ECSA values were calculated and displayed in **Table 3.4**. In general, the presence of functional groups on GO can facilitate the uniform dispersion and anchoring of Pd NPs with a large number of accessible active sites for catalytic reaction by acting as nucleation sites. It should be highlighted that Pd loading on Pd/GO-GNP, as evidenced by the TEM image, is onto the surface of GO-GNPs, unlike any other type of GO material wherein Pd NPs are stacked between the layers. Besides, the size of the GO-GNP is noteworthy, as it is smaller—higher in surface area—compared to other GOs, making them more accessible for electrochemical reactions. Since the surface topology can influence the HER performance, the obtained

LSV results were normalized by the ECSA value to determine the actual source of activity. The obtained ECSA normalized HER plot (**Figure 3.6**) revealed that the HER activity trend is different while normalized with ECSA values. The HER activity followed the order: Pd/GO-commercial > Pd/GO-graphite150 > Pd/GO-GNP > Pd/GO-graphite45. These observations support the fact that the electrochemical activity obtained is mainly due to the enhanced electrochemical surface area of the catalyst, for which one cannot rule out the role of functional groups, which indirectly contribute to achieving a high electrochemical surface area.

Table 3.4. Double-layer capacitance (C_{dl}) value and its derived ECSA values for different catalysts.

Electrocatalysts	**C_{dl} (mF/cm^2)**	**ECSA (cm^2)**
Pd/GO-GNP	16.66	416.50
Pd/GO-commercial	0.15	3.75
Pd/GO-graphite150	2.31	57.75
Pd/GO-graphite45	6.59	164.75

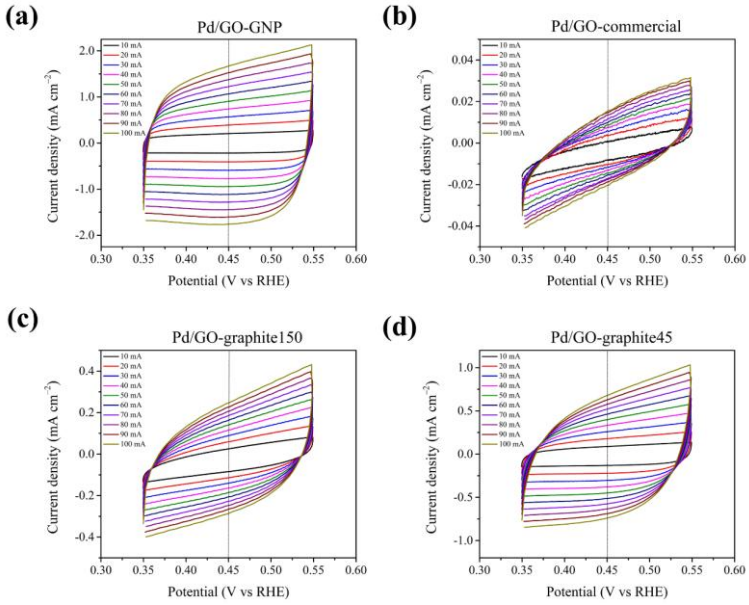

Figure 3.5. Cyclic voltammogram curves measurements in the non-faradic region to obtain the double-layer capacitance (C_{dl}).

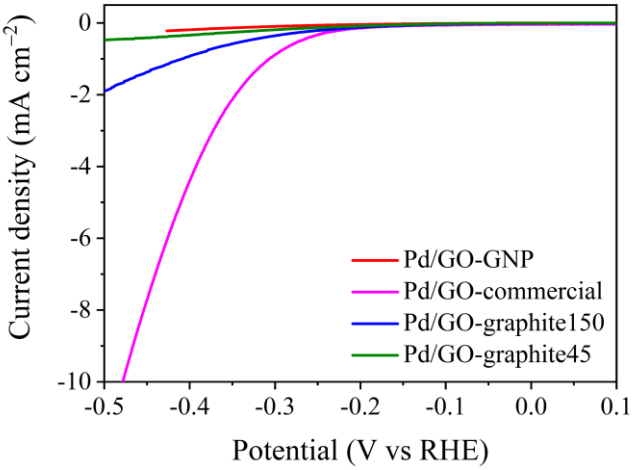

Figure 3.6. A plot of HER polarization curves normalized by ECSA.

Summarizing all the electrochemical measurements, it is reasonable to conclude that poorer functionality generates faster charge transfer kinetics. However, to validate this hypothesis, I further expanded my studies to evaluate the electrochemical performance of two types of GO-GNP, i.e., Pd/GNP and Pd@GOF-GNP. The extent of functionalization in GOF is usually higher than in GO due to the introduction of cross-linkers or other functional groups, providing a porous or extended network. As expected from the electrochemical HER results (**Figure 3.7**), a better activity of Pd/GO-GNP compared to Pd/GNP and Pd@GOF-GNP is determined. Although Pd@GOF-GNP has well-dispersed Pd NPs, their confinement between the GO layers makes it less accessible for the catalytic reaction. This is further evident from the obtained C_{dl} values in **Figure 3.8**. The lower C_{dl} value of Pd@GOF-GNP compared to Pd@GO-GNP could be attributed to its fewer exposed electrochemically active sites. CV measurements (**Figure 3.9**) were performed to identify the distinct role of Pd NPs. The palladium peak at +0.1 V vs RHE reflects that Pd/GO-GNP has more exposed active sites than Pd/GO-graphite45 and other catalysts. This finding correlates well with the TEM results. Altogether, it could be concluded that the Pd NPs distribution on or in between the GO layers has a critical role in determining HER performance, suggesting that tailoring the functional groups for more

exposure to the active surface might show better electrochemical performance.

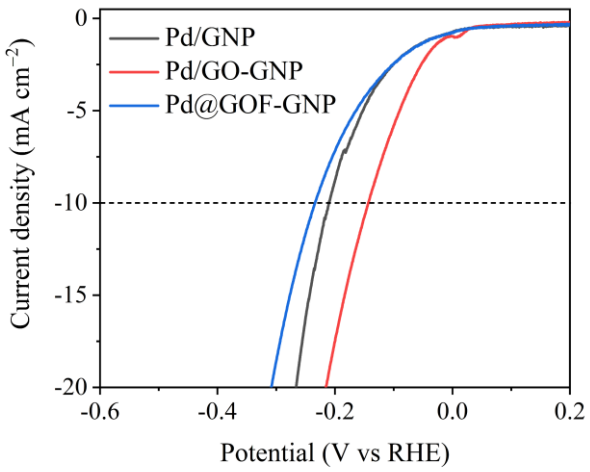

Figure 3.7. HER polarization curves of Pd with GNP material: Pd/GNP (without GO oxidation), Pd/GO-GNP (after GO oxidation), and Pd@GOF-GNP (forming graphene oxide framework) measured in 0.5 M H_2SO_4 at 1600 rpm rotation.

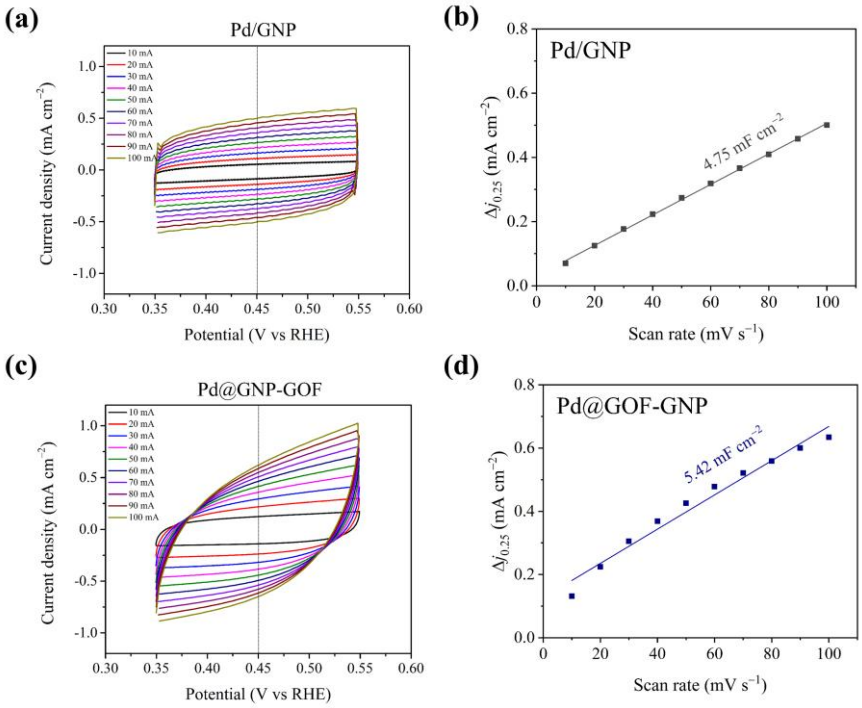

Figure 3.8. (a, c) CV in a non-faradaic region, and (b, d) their corresponding C_{dl} values.

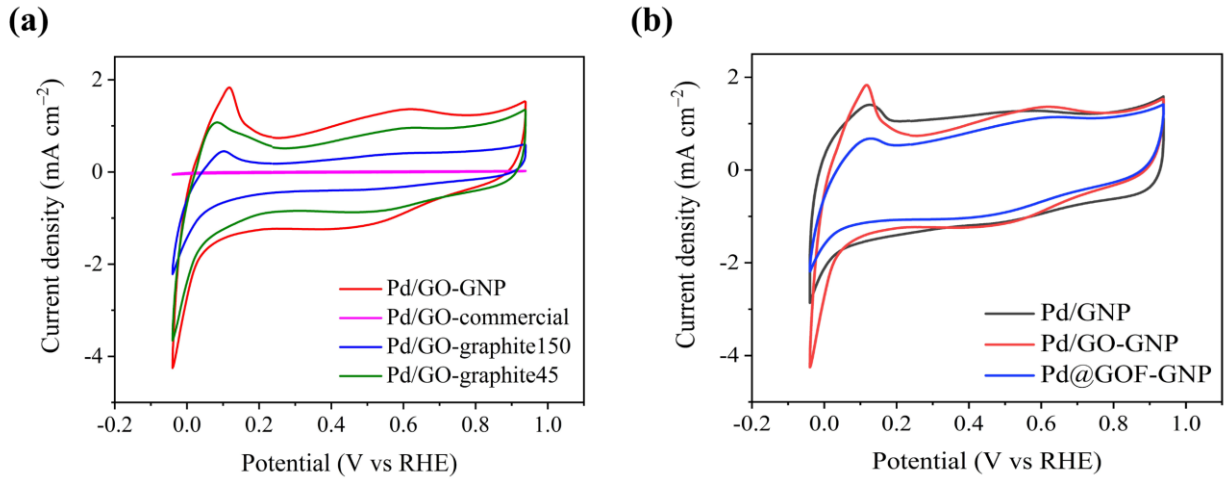

Figure 3.9. Cyclic voltammogram of various Pd-GO catalysts measured in 0.5 M H_2SO_4 solution at a scan rate of 50 mV s^{-1}.

Stability is an important criterion when proposing an electrocatalyst for practical applications. To analyze it, the HER polarization curves were measured before and after 1000 CV cycles. **Figure 3.2d** shows the HER polarization curves of Pd/GO-GNP measured before the 1st CV cycle (solid line) and after (dotted line) the 1000th CV cycle. The result reveals only an increase of 13 mV in overpotential, which implies reasonable stability. Such activity loss could be related to bubble formation that may lead to the catalyst leaching during the HER process. To rule out this, the catalyst with the same catalyst loading was coated on carbon paper, and the stability test was carried out. **Figure 3.10** shows almost no change in the polarization curve, thus confirming excellent durability. The interaction of the Pd NPs with GO's functional groups prevents their sintering or aggregation during catalytic reactions, therefore remaining at a high sur-face area over time. No characteristic changes were observed in Pd NPs, which was further corroborated by the TEM images shown in **Figure 3.11**, making Pd/GO-GNP a better electrocatalyst.

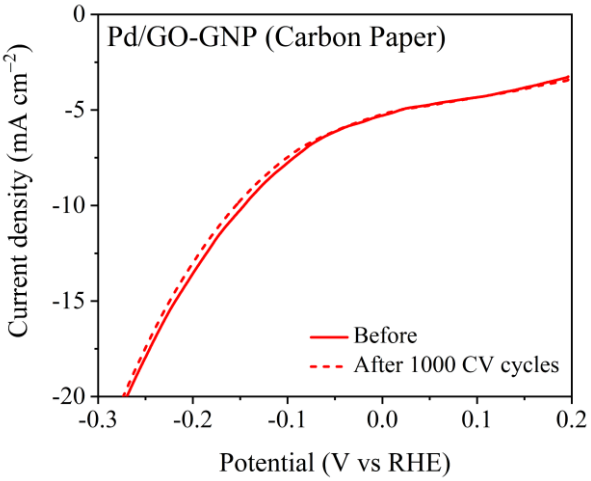

Figure 3.10. Durability test: HER polarization curves obtained before and after 1000 CV cycles at 5 mV s^{-1} (Pd/GO-GNP catalyst coated on carbon paper substrate).

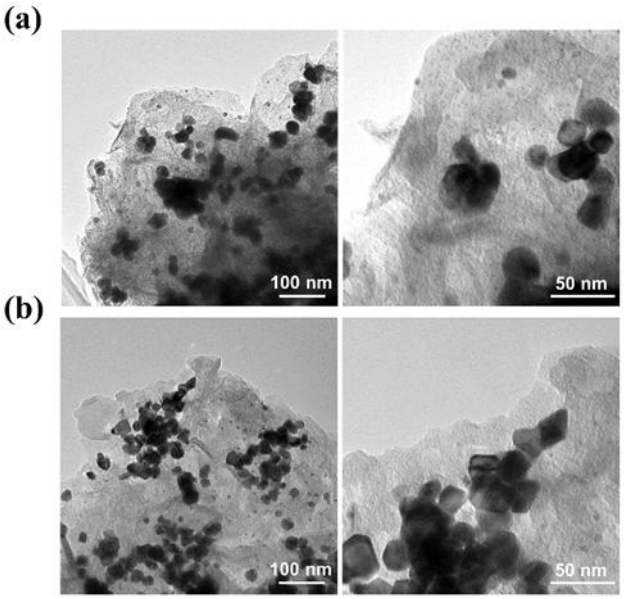

Figure 3.11 TEM images for the Pd/GO-GNP catalysts (a) before and (b) after 1000 CV cycles.

3.4. Conclusions

In summary, I state the critical role of functional groups and other structural features of graphitic-material-supported catalysts—Pd/GO—in electrochemical HER performance. Some key findings of this study are summarized as follows: 1. GO support in-plane functionalities have a significant role in Pd dispersion and anchoring. While the surface of Pd NPs is exposed on lower functionality GO-GNP support, for other GOs—although Pd NPs are smaller and homogeneous—they are entrapped between the layers, making them less accessible. 2. Apparently, the lateral dimensions of GO are very important in deciding its catalytic performance. While small GO/GNP sheets form a well-connected (sturdy) network with high electrochemically active surface area for fast electron transfer, larger sheets in GO-graphite45 and GO-graphite150 hinder this. The Pd/GO-GNP, having the highest activity of 143 mV@10mA cm^{-2}, benefits from the coincidental balance of optimal particle size, less inplane functionalities, defect density, and higher electrochemical surface area. The present work outlines the possibility of using GO supports in the rational design of HER electrocatalysts by tailoring their physiochemical properties.

References

(1) Prytkova, A.; Kirsanova, M. A.; Kiiamov, A. G.; Tayurskii, D. A.; Dimiev, A. M. Ni–Pd Nanocomposites on Reduced Graphene Oxide Support as Electrocatalysts for Hydrogen Evolution Reactions. *ACS Appl. Nano Mater.* **2023**, *6* (16), 14902–14909. https://doi.org/10.1021/acsanm.3c02461.

(2) Fei, H.; Dong, J.; Arellano-Jiménez, M. J.; Ye, G.; Dong Kim, N.; Samuel, E. L. G.; Peng, Z.; Zhu, Z.; Qin, F.; Bao, J.; Yacaman, M. J.; Ajayan, P. M.; Chen, D.; Tour, J. M. Atomic Cobalt on Nitrogen-Doped Graphene for Hydrogen Generation. *Nat. Commun.* **2015**, *6* (1), 8668. https://doi.org/10.1038/ncomms9668.

(3) Li, X.; Zhao, L.; Yu, J.; Liu, X.; Zhang, X.; Liu, H.; Zhou, W. Water Splitting: From Electrode to Green Energy System. *Nano-Micro Lett.* **2020**, *12* (1), 131. https://doi.org/10.1007/s40820-020-00469-3.

(4) Jayabharathi, J.; Karthikeyan, B.; Vishnu, B.; Sriram, S. Research on Engineered Electrocatalysts for Efficient Water Splitting: A Comprehensive Review. *Phys. Chem. Chem. Phys.* **2023**, *25* (13), 8992–9019. https://doi.org/10.1039/D2CP05522H.

(5) Sathiyan, K.; Mondal, T.; Mukherjee, P.; Patra, S. G.; Pitussi, I.; Kornweitz, H.; Bar-Ziv, R.; Zidki, T. Enhancing the Catalytic OER

Performance of MoS2 via Fe and Co Doping. *Nanoscale* **2022**, *14* (43), 16148–16155. https://doi.org/10.1039/D2NR03816A.

(6) Islam, A.; Islam, T.; Mahmud, H.; Raihan, O.; Islam, Md. S.; Marwani, H. M.; Rahman, M. M.; Asiri, A. M.; Hasan, Md. M.; Hasan, Md. N.; Salman, Md. S.; Kubra, K. T.; Shenashen, M. A.; Sheikh, Md. C.; Awual, Md. R. Accelerating the Green Hydrogen Revolution: A Comprehensive Analysis of Technological Advancements and Policy Interventions. *Int. J. Hydrog. Energy* **2024**, *67*, 458–486. https://doi.org/10.1016/j.ijhydene.2024.04.142.

(7) Aslam, S.; Rani, S.; Lal, K.; Fatima, M.; Hardwick, T.; Shirinfar, B.; Ahmed, N. Electrochemical Hydrogen Production: Sustainable Hydrogen Economy. *Green Chem.* **2023**, *25* (23), 9543–9573. https://doi.org/10.1039/D3GC02849F.

(8) Jawhari, A. H.; Hasan, N. Nanocomposite Electrocatalysts for Hydrogen Evolution Reactions (HERs) for Sustainable and Efficient Hydrogen Energy—Future Prospects. *Materials* **2023**, *16* (10), 3760. https://doi.org/10.3390/ma16103760.

(9) Davodi, F.; Cilpa-Karhu, G.; Sainio, J.; Tavakkoli, M.; Jiang, H.; Mühlhausen, E.; Marzun, G.; Gökce, B.; Laasonen, K.; Kallio, T. Designing of Low Pt Electrocatalyst through Immobilization on metal@C Support for

Efficient Hydrogen Evolution Reaction in Acidic Media. *J. Electroanal. Chem.* **2021**, *896*, 115076. https://doi.org/10.1016/j.jelechem.2021.115076.

(10) Li, Z.; Ge, R.; Su, J.; Chen, L. Recent Progress in Low Pt Content Electrocatalysts for Hydrogen Evolution Reaction. *Adv. Mater. Interfaces* **2020**, *7* (14), 2000396. https://doi.org/10.1002/admi.202000396.

(11) Balint, L.-C.; Hulka, I.; Kellenberger, A. Pencil Graphite Electrodes Decorated with Platinum Nanoparticles as Efficient Electrocatalysts for Hydrogen Evolution Reaction. *Materials* **2022**, *15* (1), 73. https://doi.org/10.3390/ma15010073.

(12) Liu, M.; Wang, X.; Liu, J.; Wang, K.; Jin, S.; Tan, B. Palladium as a Superior Cocatalyst to Platinum for Hydrogen Evolution Using Covalent Triazine Frameworks as a Support. *ACS Appl. Mater. Interfaces* **2020**, *12* (11), 12774–12782. https://doi.org/10.1021/acsami.9b21903.

(13) Chen, A.; Ostrom, C. Palladium-Based Nanomaterials: Synthesis and Electrochemical Applications. *Chem. Rev.* **2015**, *115* (21), 11999–12044. https://doi.org/10.1021/acs.chemrev.5b00324.

(14) Yu, H.; Díaz, A.; Lu, X.; Sun, B.; Ding, Y.; Koyama, M.; He, J.; Zhou, X.; Oudriss, A.; Feaugas, X.; Zhang, Z. Hydrogen Embrittlement as a Conspicuous Material Challenge─comprehensive Review and Future

Directions. *Chem. Rev.* **2024**, *124* (10), 6271–6392. https://doi.org/10.1021/acs.chemrev.3c00624.

(15) Sathiyan, K.; Lal, A.; Borenstein, A. Laser Processed Magnetite Nanoparticles Embedded on rGO Composites for Efficient Electrocatalytic Oxygen Evolution Reaction. *Adv. Sustain. Syst.* **2022**, *6* (7), 2200076. https://doi.org/10.1002/adsu.202200076.

(16) Khine, Y. Y.; Wen, X.; Jin, X.; Foller, T.; Joshi, R. Functional Groups in Graphene Oxide. *Phys. Chem. Chem. Phys.* **2022**, *24* (43), 26337–26355. https://doi.org/10.1039/D2CP04082D.

(17) Amirov, R. R.; Shayimova, J.; Nasirova, Z.; Solodov, A.; Dimiev, A. M. Analysis of Competitive Binding of Several Metal Cations by Graphene Oxide Reveals the Quantity and Spatial Distribution of Carboxyl Groups on Its Surface. *Phys. Chem. Chem. Phys.* **2018**, *20* (4), 2320–2329. https://doi.org/10.1039/C7CP07055A.

(18) Amirov, R. R.; Shayimova, J.; Nasirova, Z.; Dimiev, A. M. Chemistry of Graphene Oxide. Reactions with Transition Metal Cations. *Carbon* **2017**, *116*, 356–365. https://doi.org/10.1016/j.carbon.2017.01.095.

(19) Chen, X.; Wu, G.; Chen, J.; Chen, X.; Xie, Z.; Wang, X. Synthesis of "Clean" and Well-Dispersive Pd Nanoparticles with Excellent

Electrocatalytic Property on Graphene Oxide. *J. Am. Chem. Soc.* **2011**, *133* (11), 3693–3695. https://doi.org/10.1021/ja110313d.

(20) Hanan, A.; Shu, D.; Aftab, U.; Cao, D.; Laghari, A. J.; Solangi, M. Y.; Abro, M. I.; Nafady, A.; Vigolo, B.; Tahira, A.; Ibupoto, Z. H. Co2FeO4@rGO Composite: Towards Trifunctional Water Splitting in Alkaline Media. *Int. J. Hydrog. Energy* **2022**, *47* (80), 33919–33937. https://doi.org/10.1016/j.ijhydene.2022.07.269.

(21) Kumar, K. P. A.; Alduhaish, O.; Adil, S. F.; Pumera, M. Grafting of Pd on Covalently and Noncovalently Modified N-doped Graphene for Electrocatalysis. *Adv. Mater. Interfaces* **2022**, *9* (27), 2102317. https://doi.org/10.1002/admi.202102317.

(22) Zubir, N. A.; Yacou, C.; Motuzas, J.; Zhang, X.; Diniz da Costa, J. C. Structural and Functional Investigation of Graphene Oxide–Fe3O4 Nanocomposites for the Heterogeneous Fenton-like Reaction. *Sci. Rep.* **2014**, *4* (1), 4594. https://doi.org/10.1038/srep04594.

(23) Tang, S.; Zhu, J. Structural and Electronic Properties of Pd-Decorated Graphene Oxides and Their Effects on the Adsorption of Nitrogen Oxides: Insights from Density Functional Calculations. *RSC Adv.* **2014**, *4* (44), 23084–23096. https://doi.org/10.1039/C4RA03910F.

(24) Karuppasamy, L.; Gurusamy, L.; Anandan, S.; Liu, C.-H.; Wu, J. J. Graphene Nanosheets Supported High-Defective Pd Nanocrystals as an Efficient Electrocatalyst for Hydrogen Evolution Reaction. *Chem. Eng. J.* **2021**, *425*, 131526. https://doi.org/10.1016/j.cej.2021.131526.

(25) Gao, C.; Wada, T.; Seenivasan, K.; Chammingkwan, P. Critical Properties for Stabilizing Pd Nanoparticles in Graphene Oxide Framework-Supported Catalysts: Insights from Multifaceted Characterization. Social Science Research Network: Rochester, NY July 9, 2024. https://doi.org/10.2139/ssrn.4888219.

(26) Tran, T. P. N.; Thakur, A.; Trinh, D. X.; Dao, A. T. N.; Taniike, T. Design of Pd@Graphene Oxide Framework Nanocatalyst with Improved Activity and Recyclability in Suzuki-Miyaura Cross-Coupling Reaction. *Appl. Catal. Gen.* **2018**, *549*, 60–67. https://doi.org/10.1016/j.apcata.2017.09.026.

(27) Tran, T. P. N.; Nguyen, T. N.; Taniike, T.; Nishimura, S. Tailoring Graphene Oxide Framework with N- and S- Containing Organic Ligands for the Confinement of Pd Nanoparticles Towards Recyclable Catalyst Systems. *Catal. Lett.* **2021**, *151* (1), 247–254. https://doi.org/10.1007/s10562-020-03284-y.

(28) Seenivasan, K.; Tran, T. P. N.; Mohan, P.; Ton, N. N. T.; Thakur, A.; Chammingkwan, P.; Rawat, D. S.; Taniike, T. Graphene Oxide Framework-Confined Ru (Ru@GOF) as Recyclable Catalyst for Hydrogenation of Levulinic Acid into γ-Valerolactone with Formic Acid. *J. Mater. Sci.* **2022**, *57* (25), 11714–11724. https://doi.org/10.1007/s10853-022-07340-3.

(29) Mukherjee, P.; Sathiyan, K.; Vishwanath, R. S.; Zidki, T. Anchoring MoS2 on an Ethanol-Etched Prussian Blue Analog for Enhanced Electrocatalytic Efficiency for the Oxygen Evolution Reaction. *Mater. Chem. Front.* **2022**, *6* (13), 1770–1778. https://doi.org/10.1039/D2QM00183G.

(30) Mukherjee, P.; Sathiyan, K.; Bar-Ziv, R.; Zidki, T. Chemically Etched Prussian Blue Analog–WS2 Composite as a Precatalyst for Enhanced Electrocatalytic Water Oxidation in Alkaline Media. *Inorg. Chem.* **2023**, *62* (35), 14484–14493. https://doi.org/10.1021/acs.inorgchem.3c02537.

(31) Schneider, C. A.; Rasband, W. S.; Eliceiri, K. W. NIH Image to ImageJ: 25 Years of Image Analysis. *Nat. Methods* **2012**, *9* (7), 671–675. https://doi.org/10.1038/nmeth.2089.

Chapter 4

Design of Graphene Oxide by Tuning the Types of Linker Molecules for Recyclable Nanocatalysis

Chapter 4

Abstract

Catalyst supports play a critical role in metal nanoparticle (NP) catalysts. Traditional methods, such as impregnation, are commonly used to confine NPs within porous materials to prevent sintering. Graphene oxide frameworks (GOFs), which are porous materials formed by the crosslinking of graphene oxide (GO) with linker molecules, are widely investigated for various applications such as water treatment and gas storage, while also holding potential as supports for NP catalysts. The properties of GOF is highly depends on the types of linker molecule; however, the impact of linker molecules with different functional groups on the performance of GOF-confined nanocatalysts has not been systematically investigated. In this study, various linker molecules were used to synthesize GOFs and their capability as nanocatalyst supports were investigated. By comparing the properties and catalytic performance of different GOFs, the significance of linker molecules on catalytic performance was highlighted. The findings contribute valuable insights for designing high-performance GOF-confined catalysts tailored for different environments.

Keywords: Graphene oxide, graphene oxide framework, Suzuki-Miyaura coupling raction, nano catalysts

Chapter 4

4.1. Introduction

In heterogeneous catalysis, the number of exposed active sites has long been regarded as one of the most important concepts.[1] The confined environment around the active sites can help to stabilize active sites and modulate chemistry at the sites, which has a significant effect on catalytic performance, similar to the role of globular proteins in an enzyme.[2,3] The reactants and metal/metal–oxide nanoparticles (NPs) have been known to exhibit modified behaviors and properties compared to their unconfined counterparts.[4,5]

A significant effect on the adsorption energies of molecules confined in porous materials like zeolites and metal-organic framework (MOF) materials has been established.[6] The spatial restriction of metal NPs within nano-sized spaces can inhibit their sintering, aggregation, detachment, and poisoning, thus enhancing activity.[7] Most conventional methods involve tedious preparation processes, including impregnation, self-assembly, ligand template approach, and covalent anchoring of metal precursors followed by the reducing and capping agents.[8] Therefore, advanced technologies for the preparation of confined NPs are needed to overcome the existing limitations.

Chapter 4

Synthesis of graphene oxide frameworks (GOFs), in which graphene oxide (GO) sheets are crosslinked by linker molecules, has produced a new class of porous materials with a wide range of applications.[9]

Several research groups have reported the successful applications of GOFs. For instance, Nicolai et al. reported GOFs as a potential material for high-performance desalination membranes based on classical molecular dynamics simulations.[10] The GOFs have also been successfully applied in gas storage as a superior adsorbent for H_2 and CO_2.[11–13] It has also been demonstrated that a covalently linked GOF is a promising support for hosting metal NPs in a catalytically recyclable fashion. Additionally, covalently linked GOFs show great potential as recyclable supports for metal nanocatalysts. Reports indicate that confined Pd and Ru NPs exhibit excellent dispersion and uniform size distribution inside the GOF gallery space, which afforded superior activity and recyclability compared to the unconfined catalysts.[14–16] Due to its diverse functional groups, GO can be linked with molecules having different functional groups to synthesize GOFs with various characteristics. This is significant for designing the high-performance catalysts that can adapt to different catalytic environments. Therefore, it is crucial to understand how linker molecules with different functional groups affect the catalytic performance of GOFs. However, to the

best of my knowledge, there has been no systematic discussion on how different covalent crosslinking molecules affect the catalytic performance of catalysts supported by GOFs to date.

In this research, I focused on how linker molecules with different functional groups affect the catalytic performance of the synthesized GOFs. I used 2 different GO sources and five different linker molecules with various functional groups and commercial GO to synthesize different GOFs. These GOFs were then used to support palladium catalysts (Pd@GOF) for catalytic reactions. The GOFs and Pd@GOFs were characterized using multiple techniques, and by comparing the characterization results and catalytic performance of different GOFs, I elucidated the impact of linker molecules on GOFs.

4.2. Experimental section

4.2.1. Materials

GO (dry powder, 50-100 mesh), was purchased from Layer One–Advanced Materials. Benzene-1,4-diboronic acid (PDBA, ≥ 95.0%), palladium (II) chloride ($PdCl_2$, ≥ 99.9%), were purchased from Sigma Aldrich. Graphite (particle size > 45 μm, purity > 98%), N,N-dimethylformamide (DMF, ≥ 99.5%), *p*-phenylenediamine (pPDA, ≥ 97.0%),

diethyl ether (≥ 99.5%), were supplied by Wako Pure Chemical Industries, Ltd. Terephthalaldehyde (TPA, > 98.0%), terephthalic acid (PDCA, ≥ 99.0%), 1,4-phenylene diisocyanate (PDIC, ≥ 98.0%), obtained from Tokyo Chemical Industry Co., Ltd. Toluene (≥ 99.7%), methanol (≥ 99.8%), ethanol (≥ 99.5%), were obtained from Kanto Chemical Co., Inc. Silicon (VI) oxide (α-quartz powder, 0.8 μm, ≥ 99.9%) was purchased from Koujundo Chemical Laboratory CO., Ltd. All chemicals were of research grade and used without further purification.

4.2.2. Sample preparation

The GO sources was used the commercial GO and GO which synthesized by modified Hummers method. The GOF was synthesized by solvent thermal method[17]. The GO powder (300 mg) was dispersed in a solution where linker dissolved (5.4 mmol) in a solvent (60 mL). The solvent was chosen based on the used linkers and the details are given in **Table 4.1**, The GO slurry was then heated at 60 or 80 °C for 24 or 48 h under an N_2 atmosphere. The suspension is stirred every few hours. After the reaction, the slurry is washed with methanol and centrifugated several times. Finally, the separated powder is vacuum dried at 60 °C for 12 hours to obtain GOF-yyy-xxx: yyy is the name of GO sources and xxx is the name of the used linker.

Table 4.1. Reaction condition for preparation of GOFs

Linker	Solvent	Time (h)	Temperature (°C)
pPDA	H_2O	24	60
PDCA	DMF	24	60
TPA	Methanol	24	60
PDIC	DMF	24	60
PDBA	Methanol	48	80

To understand the correlation of the linker amount and the structural characteristic of the GOF, I prepared GOF-PDBA and GOF-PDIC with varying the charge amount of the linker (3, 6, 9, 12, 15 and 18 mmol/g-GO) with the same basic preparation protocol.

4.2.3. Synthesis of Pd@GOF

The Pd@GOF was synthesized through the reduction of $PdCl_2$ in the presence of a GOF in toluene.[14] $PdCl_2$ (12 mg) and a GOF (60 mg) were

mixed under an N_2 atmosphere in a glove bag. Then, toluene (30 ml) was added to the mixture. The solvent was heated at 80 °C and stirred for 4 h under N_2. After the reaction, the dispersion was allowed to settle and cool to room temperature. Finally, the slurry was filtered and washed with diethyl ether using a 0.22 μm PES membrane (EMD Millipore) filter. The resulting catalyst was vacuum-dried at 60 °C for 12 h.

4.2.5. Characterization

The interlayer distance (*d*-spacing) between GO sheets was determined based on powder XRD. The XRD patterns were recorded in the 2θ range of 5–90° at a speed of 2°/min and a step size of 0.01° on MiniFlexC600 (Rigaku) with Cu Kα radiation (λ = 1.5418 Å). Measurements were performed 3 times for each sample to calculate the error range. To quantify the peak intensity, SiO_2 (α-quartz) powder was chosen as a standard as the most intense peak (101 at 26.6°) is well separated from those of GOFs. The SiO_2 standard was mixed with the sample with the weight ratio of 1:3. Raman spectra of powder samples dispersed on a glass plate were recorded using a laser Raman spectrometer, NRS-4100 (JASCO) with an excitation wavelength of 532 nm and an exposure time of 25 s with 10 acquisitions. Measurements were performed 3 times for each sample to calculate the error

range. The covalent functionalization of GO was confirmed using Fourier transform infrared spectroscopy (FT-IR). The FT-IR spectra were acquired using JASCO 6100 (JASCO) in the range of 4,000–400 cm^{-1} with a resolution of 1 cm^{-1} by 16 scans. Sample powder was ground with dried KBr at a weight ratio of 1:50 and then pressed into a pellet. The morphology, particle size, and particle size distribution of the Pd NPs were investigated by TEM using H-7650 (Hitachi) operating at an acceleration voltage of 100 kV. A sample is dispersed in ethanol with ultrasonication for 15 min, then dropped onto a carbon-coated copper grid and naturally dried overnight.

4.2.6. Catalytic test

Pd@GOF and Pd/GO catalysts were used in the Suzuki-Miyaura coupling reaction of bromobenzene and phenylboronic acid to form biphenyl. Under an N_2 atmosphere, a catalyst (17.5 mg), phenylboronic acid (67.6 mg), bromobenzene (52.6 μL), and potassium carbonate (193.5 mg) were mixed in toluene (2.0 mL). The mixture was heated at 80 °C and stirred under N2 for 6 h. After the reaction, the liquid part was separated by decantation following centrifugation (10,000 rpm, 5 min). The separated liquid was analyzed using an 7890A (Agilent) equipped with a flame ionization detector (GC-FID). The yield was calculated using the following equation:

$$yield = \frac{[biphenyl]}{[bromobenzene]_0} \times 100\% \quad (1)$$

where the $[bromobenzene]_0$ is the initial concentration of bromobenzene and the [biphenyl] is the concentration of biphenyl after the reaction. The concentration was determined using GC-FID employing an external standard method.

To evaluate recyclability, the solid part was washed 5 times with toluene (5 mL) through decantation and centrifugation (10,000 rpm, 5 min). The washed catalyst was employed for the subsequent cycle of reaction. The catalytic recyclability was assessed by determining the reduction in the yield.

4.3. Results and discussion

4.3.1. Characterization of GOFs

Figure 4.2 and **Table 4.2** summarize the XRD and Raman results of all GOFs and GO starting material. In the XRD patterns (**Figure 4.2a**), GO showed a single diffraction peak at 2θ of 26.7°, corresponding to the (001) plane with the *d*-spacing of 8.3 Å. After reacting with linkers, the position of the (001) peak shifted to the lower angle side with keeping its sharpness in GOF-PDCA, TPA, PDBA. The corresponding *d*-spacing was 9.1, 9.0, and 11.2, respectively. This expansion should be arisen from the intercalation of likers into GO sheets. It is also worth noting that the GOF samples did not

show any clear sign of unreacted GO or graphite formation at 11.4° and 26.5°. On the other hand, GOF-pPDA and PDIC almost completely loose the (001) peak. This is likely due to the destruction of the GO structure, e.g., exfoliation etc. Compared the GO, almost all of the peak areas of GOFs materials have decreased, that's probably caused by lower density which is because of the expansion of *d*-spacing All the GOFs showed a similar I_D/I_G ratio than the GO. It has already been reported that there is about +0.1 deviation after GOF synthesis.[18] In the Raman spectra shown in **Figure 4.2b**, all the GOF shown a higher I_D/I_G ratio than GO, that is because of the increasing defects which caused by the consuming function groups.[19–21]

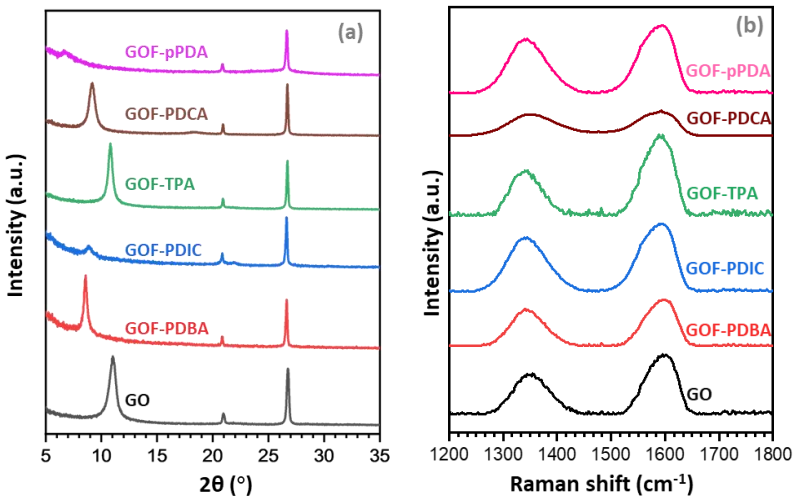

Figure 4.2 XRD patterns (a) and Raman spectra (b) of GO and GOFs with different linkers.

Table 4.2 Characterization of GOFs with different linkers

Sample code	*d*-spacing	Area ratio ($GOF_{001}/SiO_{2,101}$)	I_D/I_G ratio
GOF-pPDA	13.4 ± 0.2 Å	- *	0.79 ± 0.01
GOF-PDCA	9.1 ± 0.2 Å	3.2 ± 0.2	0.86 ± 0.02
GOF-TPA	9.0 ± 0.2 Å	3.2 ± 0.0	0.73 ± 0.02
GOF-PDIC	10.0 ± 0.3 Å	- *	0.80 ± 0.02
GOF-PDBA	11.2 ± 0.2 Å	2.2 ± 0.1	0.80 ± 0.01
GOl	8.3 ± 0.0 Å	4.3 ± 0.1	0.67 ± 0.01

* The peak area was not determined precisely due to poor fitting of the extremely broad (001) diffraction peak.

The validation of covalent bonds of GOFs was confirmed by FT-IR (**Figure 4.3**). GO showed the peaks of C=O stretch, C=C stretch, C-OR stretch, and C-O-C stretch as already reported in literature.[9,11,22] For GOF-pPDA, if it was successfully synthesized, it should show the C-H stretch, which is appear between 1650-1580 cm^{-1}, and C-N stretch which is shown between 1350-1280 cm^{-1}, but both the adsorption did not show up. The absence of these two characteristic peaks means that GOF-pPDA is probably

not successfully synthesized. At the same time, the disappearance of the peaks corresponding to stretching of C=O and C=C from GO suggests that the surface functional groups of GO may also be partly consumed. Regarding GOF-PDCA, the intensity of the peaks corresponding to C=O and C=C phenyl stretch have increased. This is because of the benzene ring with a carboxyl group of the PDCA linker. The appearance of CH_{phenyl} also supports the presence of PDCA molecule. The appearance of C-O-C stretch suggests the formation of ester bonds. These observations prove the formation of covalent link between PDCA and GO layers. As for GOF-TPA, the appearance of C=O stretch peak suggests the presence of unreacted aldehyde groups of TPA linker. The increment of C=C stretch peak and the appearance of C-H stretch peak should be due to the insertion of the benzene ring. The emergence of the C-O-C stretch peak suggests the formation of ether bonds. Thus, the successful covalent link formation was proved. In the GOF-PDIC, the C=O stretch peak has slightly shifted from that of GO because of the formation of carbamate group. The increment of C=C stretch peak and the appearance of the C-H stretch peak should be attributed to the insertion of benzene ring. The peaks attributed to C-N stretch and C-O stretch suggest the formation of carbamate group, indicating that the covalent link is established in between the PDIC and GO layers. Similar to the other GOFs,

GOF-PDBA also showed an increment of C=C stretch peak intensity, and the appearance of C-H stretch peak. And the appearance of narrow B-O and B-C stretches suggests the formation of a boronic ester bond. Both observations suggest that the PDBA linker was inserted in between GO layers with the formation of direct covalent linkers.

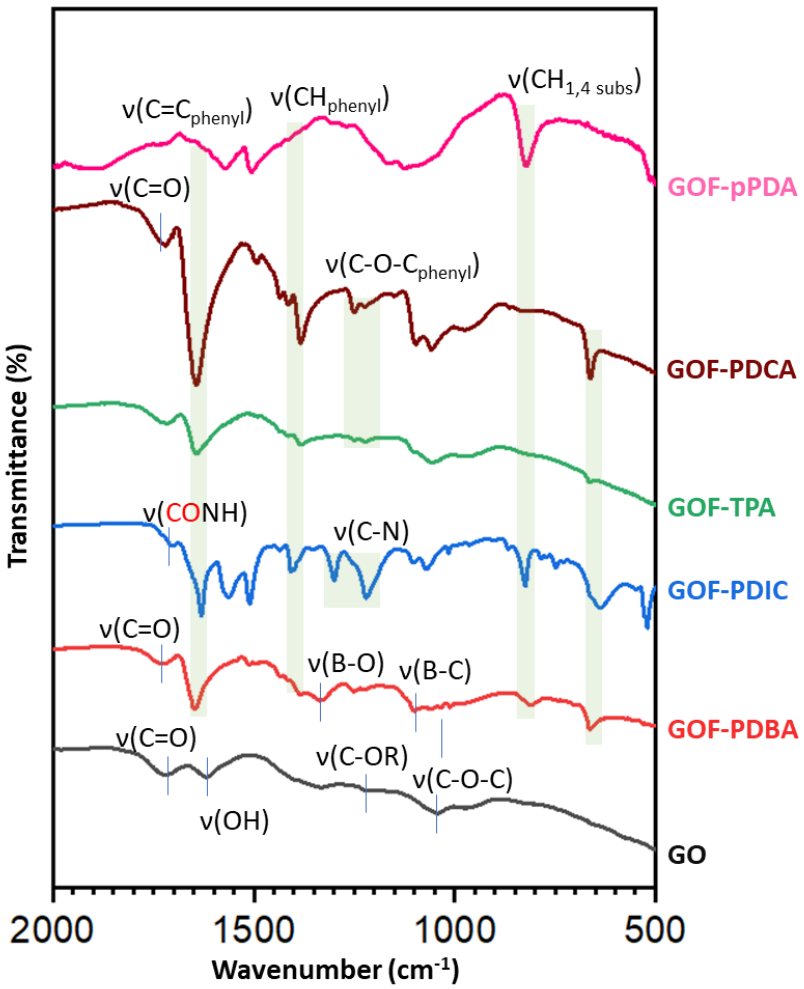

Figure 4.3 FT-IR of GO and GOFs with different linkers.

4.3.2. Characterization of catalysts

Figure 4.4 and **Table 4.3** summarize the Raman and XRD results of the catalysts supported on GOFs or GO. The (001) diffraction peaks shifted by the catalyst preparation. The differences of *d*-spacing before and after catalyst preparation are as follows: Pd@ GOF-pPDA: −0.4, Pd@ GOF-PDCA: −0.2, Pd@ GOF-TPA: −0.3, Pd@ GOF-PDIC: −1.9, Pd@ GOF-PDBA: −2.2, Pd/GO: −0.8. One can consider the GOF structure itself has been affected by the reduction process, but all the Pd supported catalysts showed similar Raman spectra to those of the original materials except for Pd@ GOF-pPDA.

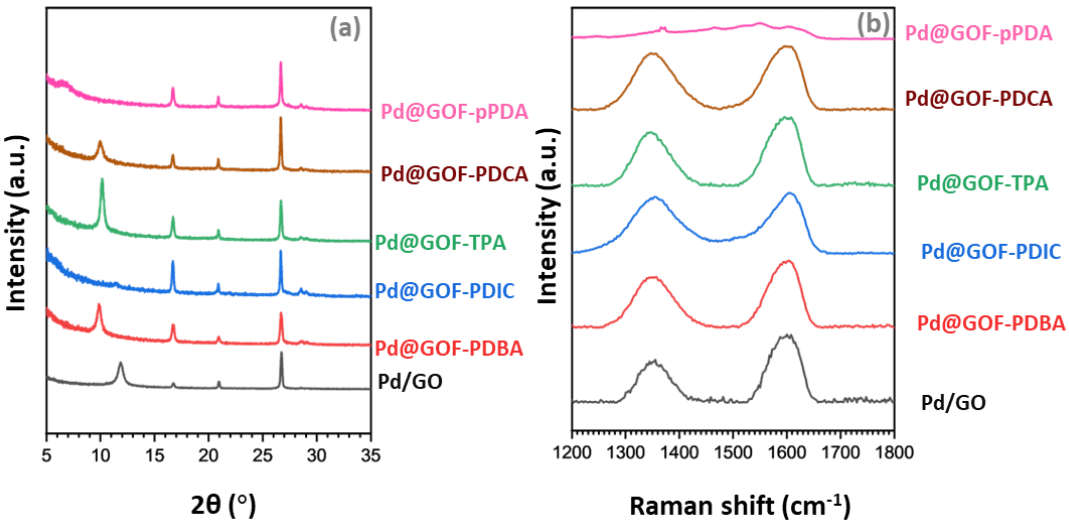

Figure 4.4 XRD patterns (a) and Raman spectra (b) of Pd@GOFs and Pd/GO.

Table 4.3 Characterization of Pd@GOFs or Pd/GO.

Sample code	*d*-spacing	Area ratio (GOF/SiO_2)	I_D/I_G ratio
Pd@ GOF-pPDA	13.8 Å	- *	-
Pd@ GOF-PDCA	8.9 Å	2.8	0.88
Pd@ GOF-TPA	8.7 Å	3.3	0.78
Pd@ GOF-PDIC	8.1 Å	- *	0.93
Pd@ GOF-PDBA	9.0 Å	3.4	0.76
Pd/GO	7.5Å	2.3	0.63

* The peak area was not determined precisely due to poor fitting of the extremely broad (001) diffraction peak.

The Pd NP particle dispersion of all the catalysts were observed by TEM. The TEM images and particle size statistics are shown in **Figures 4.5–4.10**, respectively. The Pd NPs were observed in all the catalyst samples as darker spots. All the Pd@GOF catalysts showed a comparable size and a particle size distribution compared to those of the previous research (Pd@ GOF-PDBA: 3.9 ± 2.1 nm).[16,22] The narrow particle size distribution indicates the controlled growth of Pd NPs inside the gallery space of the GOFs, which

suppressed excessive growth and agglomeration. The difference in *d*-spacing and types of linkers did not seem to have much effect on the formation of NPs.

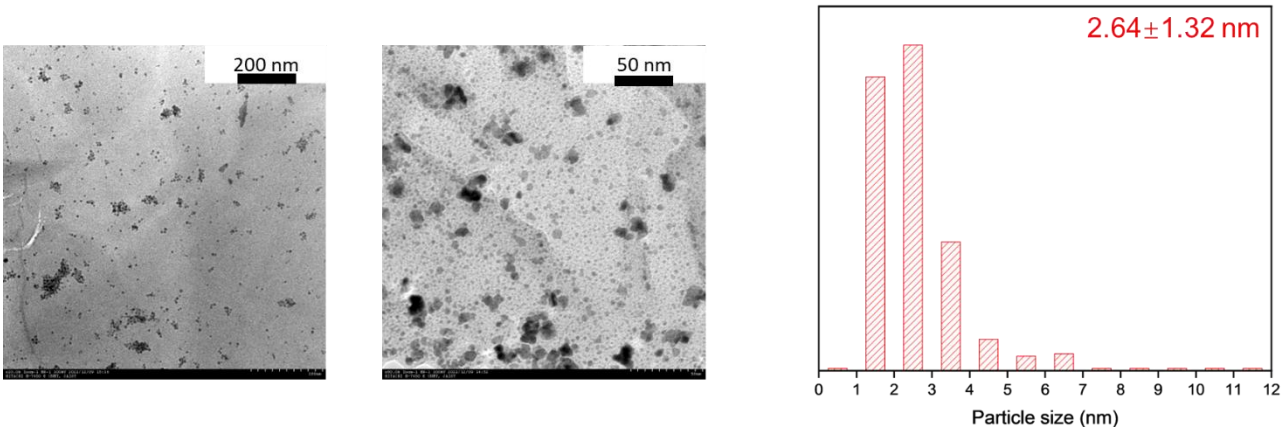

Figure 4.5 TEM images for GOF-pPDA.

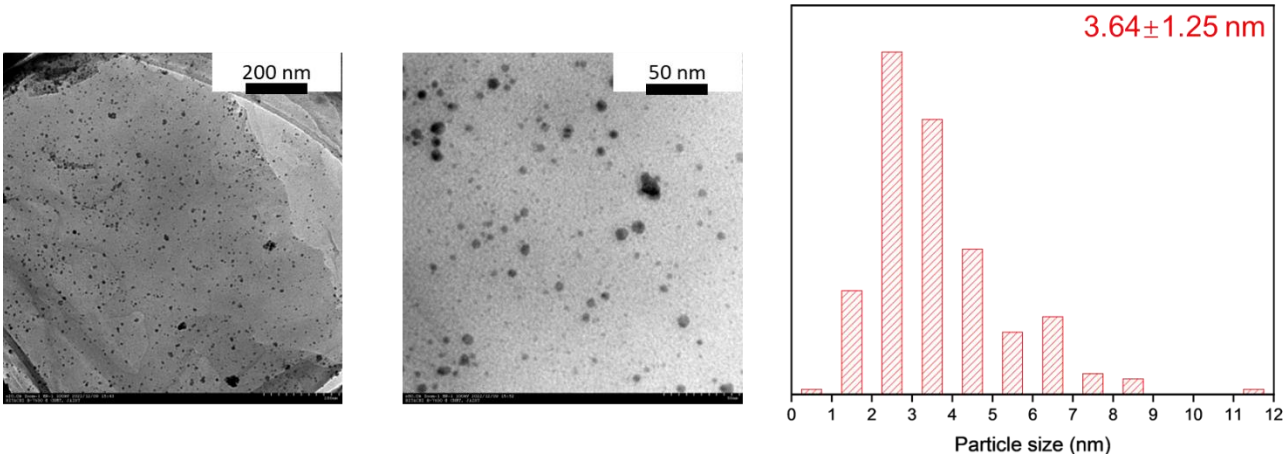

Figure 4.6 TEM images for Pd@ GOF-PDCA.

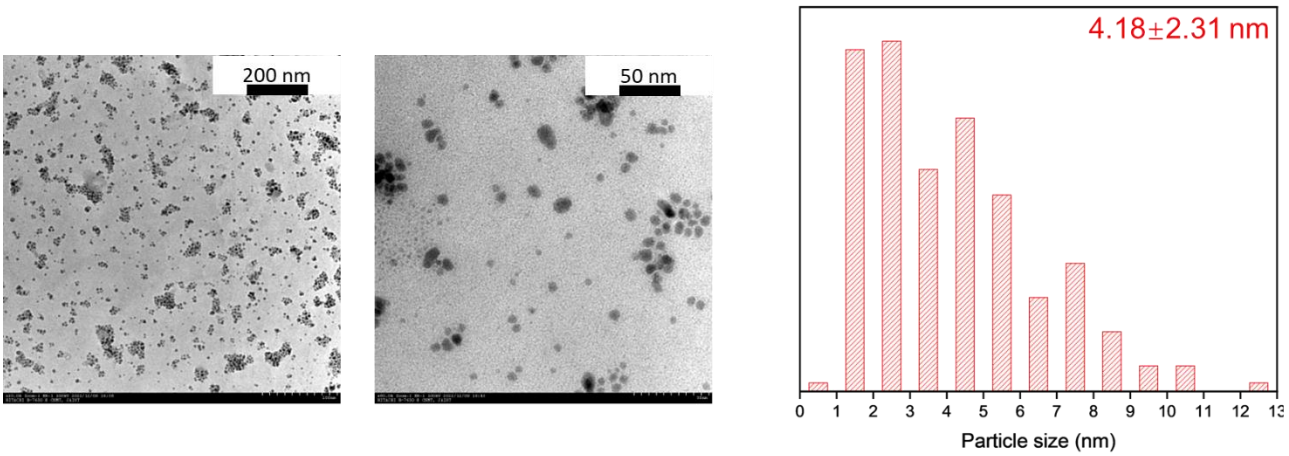

Figure 4.7 TEM images for Pd@ GOF-TPA.

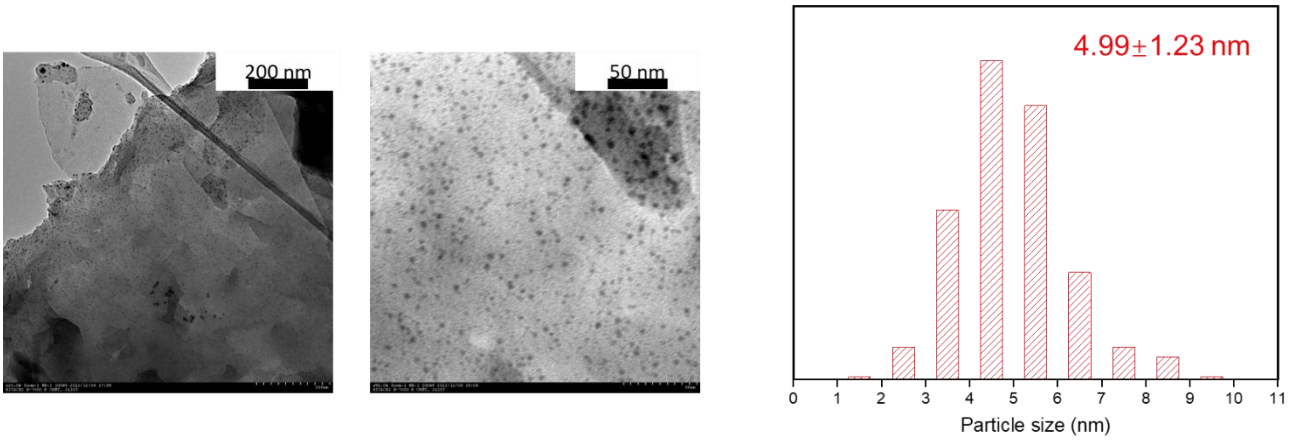

Figure 4.8 TEM images for Pd@ GOF-PDIC.

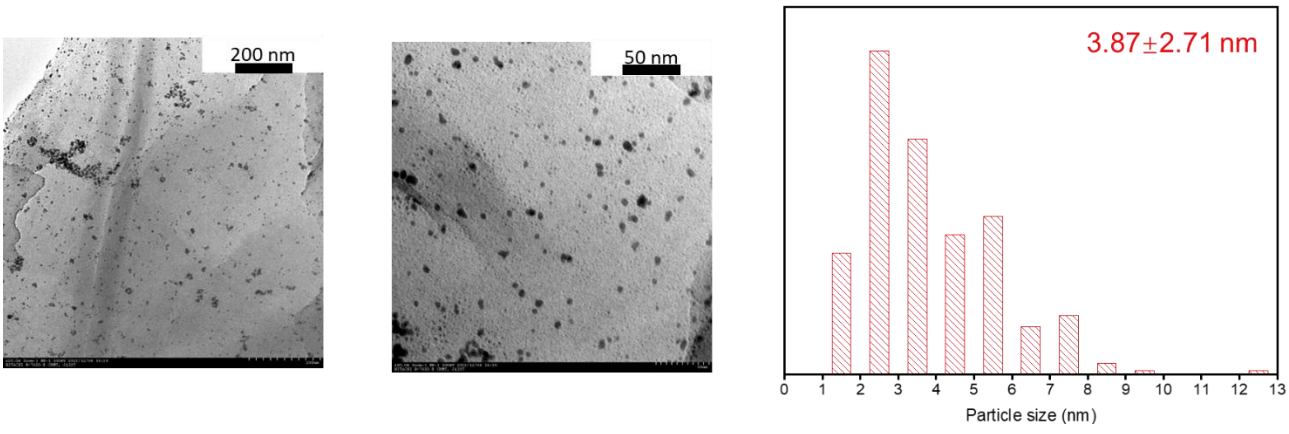

Figure 4.9 TEM images for Pd@ GOF-PDBA.

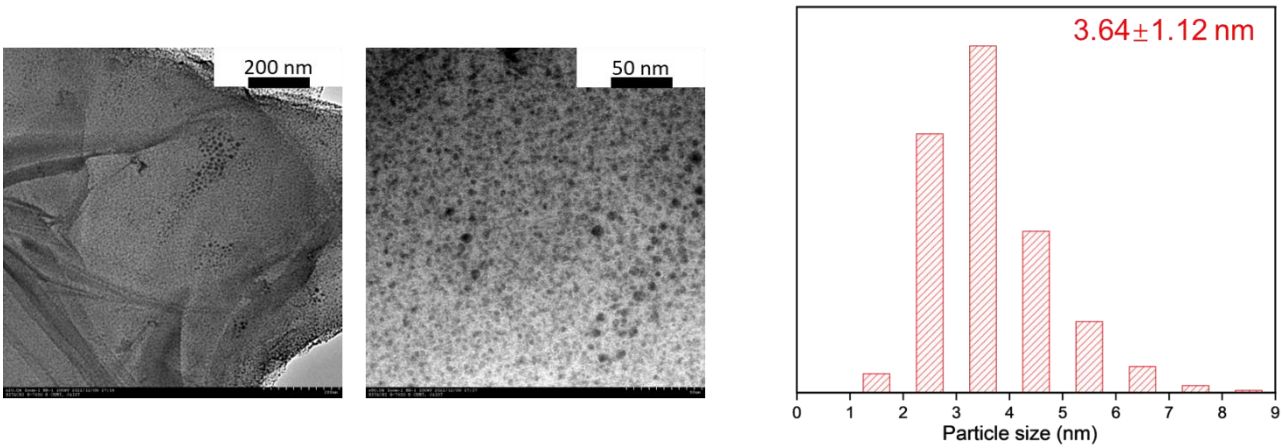

Figure 4.10 TEM images for Pd/GO.

4.3.3. Variation of the linker amount

Figure 4.11 and **Table 4.4** summarize the Raman and XRD results of all GOF-PDBA materials which were synthesized with different linker ratio. It is obvious that the *d*-spacing increased by increasing the amount of linker. It is interesting that even if a small amount of linkers were applied (GOF-PDBA-5), the (001) diffraction peak of the original GO was not observed, indicating that the linker molecules were well dispersed in the GOF structure. It is also worth noting that the (001) diffraction peak in GOF-PDBA became sharper compared to that of GO, which is suggestive of that the orderliness in the *c*-direction increased. Either crystalline dimension increment or narrowing in the distribution of *d*-spacing among the GO layers is possible.

On the other hand, the peak area decreases with increasing the linker amount.

This may involve a decrease in density due to increased *d*-spacing.

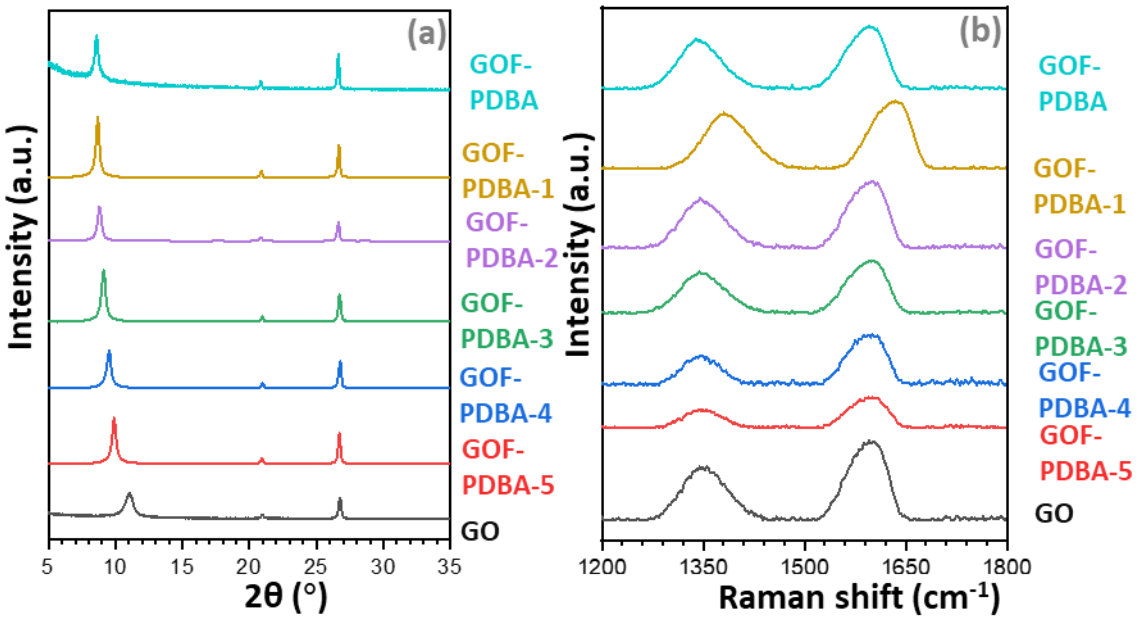

Figure 4.11 XRD (a) and Raman (b) of GOF-PDBA with different linker ratio.

Table 4.4 Characterization of GOF-PDBA with different linkers ratio.

Sample code	PDBA/GO (mmol/g)	*d*-spacing	Area ratio (GOF/SiO_2)	I_D/I_G ratio
GOF-PDBA	18	10.3 ± 0.1 Å	2.2 ± 0.1	0.80 ± 0.01
GOF-PDBA-1	15	10.0 ± 0.0 Å	2.7 ± 0.1	0.83 ± 0.01

GOF-PDBA-2	12	10.1 ± 0.1 Å	2.5 ± 0.1	0.76 ± 0.03
GOF-PDBA-3	9	9.7 ± 0.0 Å	2.4 ± 0.0	0.80 ± 0.00
GOF-PDBA-4	6	9.6 ± 0.2 Å	3.2 ± 0.0	0.57 ± 0.02
GOF-PDBA-5	3	9.4 ± 0.2 Å	3.4 ± 0.1	0.58 ± 0.01
GO	-	8.0 ± 0.0 Å	4.3 ± 0.1	0.67 ± 0.01

The FT-IR spectra of the GOF-PDBA samples are shown in **Figure 4.12**. The basic discussion has already been made in Section 4.3.1, **Figure 4.3**. With the increasing PDBA, the peak of C=C stretch which is of GO is decreased and the peaks of B-O and B-C stretches are increasing. Naturally, the number of inserted linkers increased with the loading amount. It was suggested that the number of pillars can be controlled by linker/GO ratio.

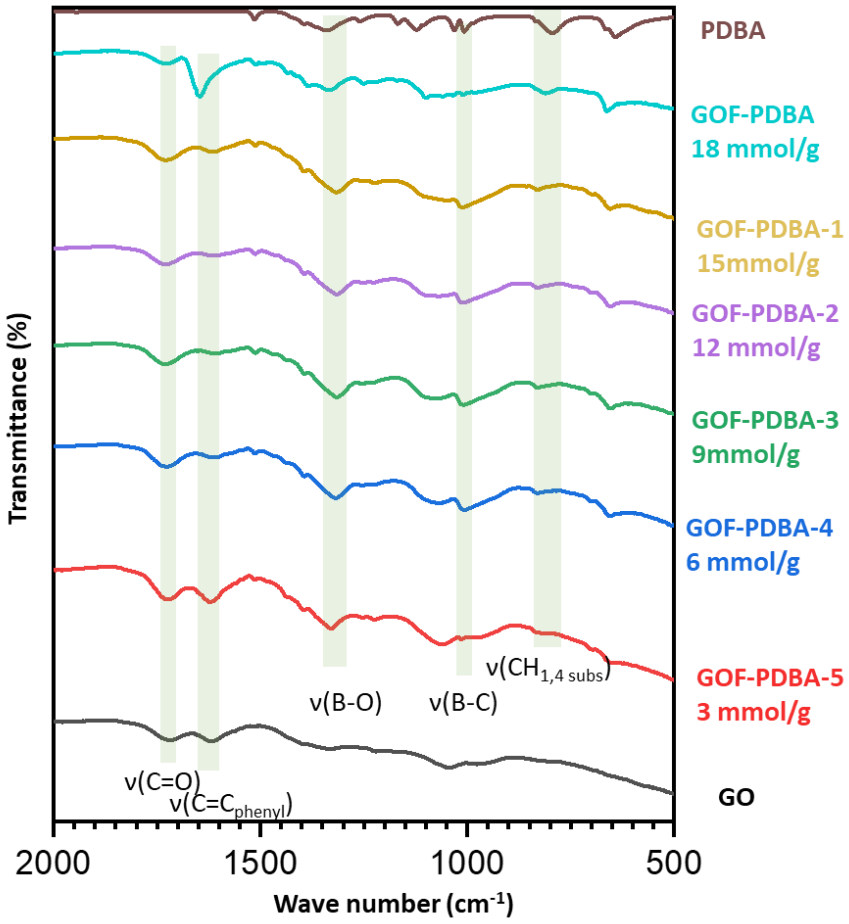

Figure 4.12 FT-IR of GO and GOF-PDBA with different linker ratio.

Figure 4.13 and **Table 4.5** summarize the Raman and XRD results of all GOF-PDIC samples which was synthesized with different linker ratio. Similar to the case of GOF-PDBA, increasing the linker amount led to a larger *d*-spacing. It is interesting that (002) diffraction peak became broader compared to that of GO, giving different effects from the PDBA.

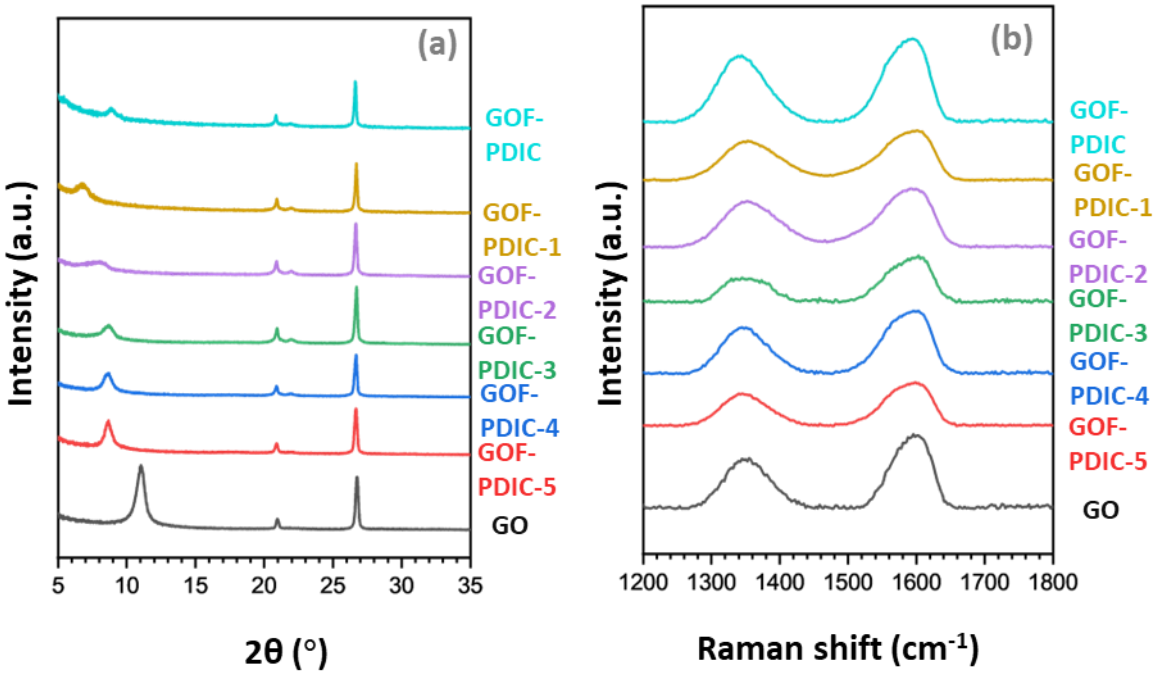

Figure 4.13 XRD (a) and Raman (b) of GOF-PDIC with different linker ratio.

Table 4.5 Characterization of GOF-PDIC with different linkers ratio.

Sample code	PDIC/GO (mmol/g)	*d*-spacing	Area ratio (GOF/SiO_2)	I_D/I_G ratio
GOF-PDIC	18	10.0 ± 0.0 Å	3.1 ± 0.3	0.80 ± 0.02
GOF-PDIC-1	15	13.3 ± 0.2 Å	5.7 ± 0.2	0.78 ± 0.03
GOF-PDIC-2	12	11.1 ± 0.0 Å	3.0 ± 0.3	0.74 ± 0.06
GOF-PDIC-3	9	10.4 ± 0.0 Å	2.5 ± 0.3	0.76 ± 0.12
GOF-PDIC-4	6	10.2 ± 0.0 Å	2.4 ± 0.2	0.80 ± 0.04
GOF-PDIC-5	3	10.2 ± 0.0 Å	2.6 ± 0.2	0.75 ± 0.05

GO	-	8.0 ± 0.0 Å	4.3 ± 0.1	0.67 ± 0.01

The FT-IR spectra of all the GOF-PDIC samples are shown in **Figure 4.14**. The basic discussion was already provided in Section 4.3.1, **Figure 4.3**. The formation of carbamate was confirmed by the appearance of the peaks corresponding to NH, C-N, and C-O stretching. The increase of the C=C and C-H stretching peaks suggests PDIC insertion. The fact that the absence of a peak corresponding to N=C=O was observed after reaction also suggests the formation of direct bonds between linker and GO layer. Compared to the GOF-PDBA, the GOF-PDIC does not show a clear tendency to change the linker/GO ratio. That is probably because the number of functional groups reactive or accessible to PDIC is very limited so even a small amount of PDIC was already in excess.

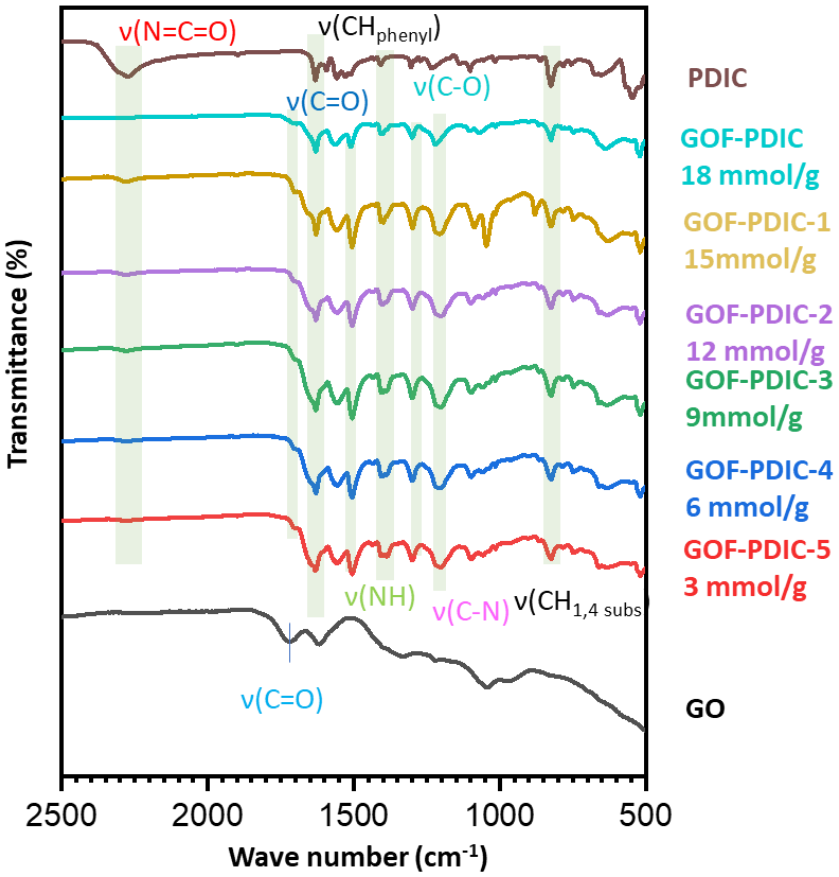

Figure 4.14 FT-IR of GO and GOF-PDIC with different linker ratio.

4.3.4 Catalytic test

Figure 4.15 shows the catalytic test and recyclability results for Pd@GOFs. In the first cycle, Pd@ GOF-PDBA exhibited the highest catalytic activity, while GOF-TPA showed the lowest. In the second cycle, the catalytic activity of almost all the catalysts significantly decreased. Pd@ GOF-PDBA experienced the most severe drop in performance, whereas the

other four Pd@GOF catalysts relatively maintained their activity, with Pd@ GOF-TPA and Pd@ GOF-PDIC demonstrating better performance.

It should be noted that commercially available GO, rather than in-house synthesized GO, was used in these experiments for reasons of scalability and accessibility. While Pd@ GOF-PDBA had the best performance in the first cycle, it exhibited the poorest performance in the second cycle. Since TEM analysis revealed no significant differences in particle size, the observed drop in activity cannot be attributed to differences in the surface area of the Pd NPs. Therefore, it is inferred that while Pd@ GOF-PDBA initially had a higher Pd loading, most of the Pd NPs were released during the first cycle. As discussed in Chapter 2, this is likely due to the limited number of in-plane functional groups in commercially available GO that can react with PDBA, resulting in insufficient linkers to retain the Pd NPs.

In contrast, the other Pd@GOFs, while exhibiting lower initial activity, retained their activity relatively well. This is likely because the other linker molecules reacted more efficiently with the functional groups on the GO surface compared to PDBA, thus maintaining a sufficient number of linkers.

In the case of GOF-pPDA, where the GO sheets were completely exfoliated, irregular aggregated structures might have formed. These structures could trap Pd NPs in the inter-particle spaces rather than on

terraces, similar to the behavior observed for GO-GNP in Chapters 2 and 3, thereby retaining some level of reactivity.

Although there is insufficient experimental evidence to fully elucidate why Pd@ GOF-TPA and Pd@ GOF-PDIC exhibited superior activity retention compared to other linkers, it is hypothesized that factors such as the compatibility between the linker and the functional groups on GO, as well as the affinity of the linkers for GO, play a role.

In summary, the critical factor in selecting linkers is their ability to balance the availability of polar functional groups necessary for the reduction and immobilization of $PdCl_2$, while maintaining a sufficient number of pillars to prevent the detachment of the formed Pd NPs. By employing linkers that selectively react with specific functional groups and appropriately tuning the functional groups on the GO surface, it may be possible to design superior support materials for catalytic applications.

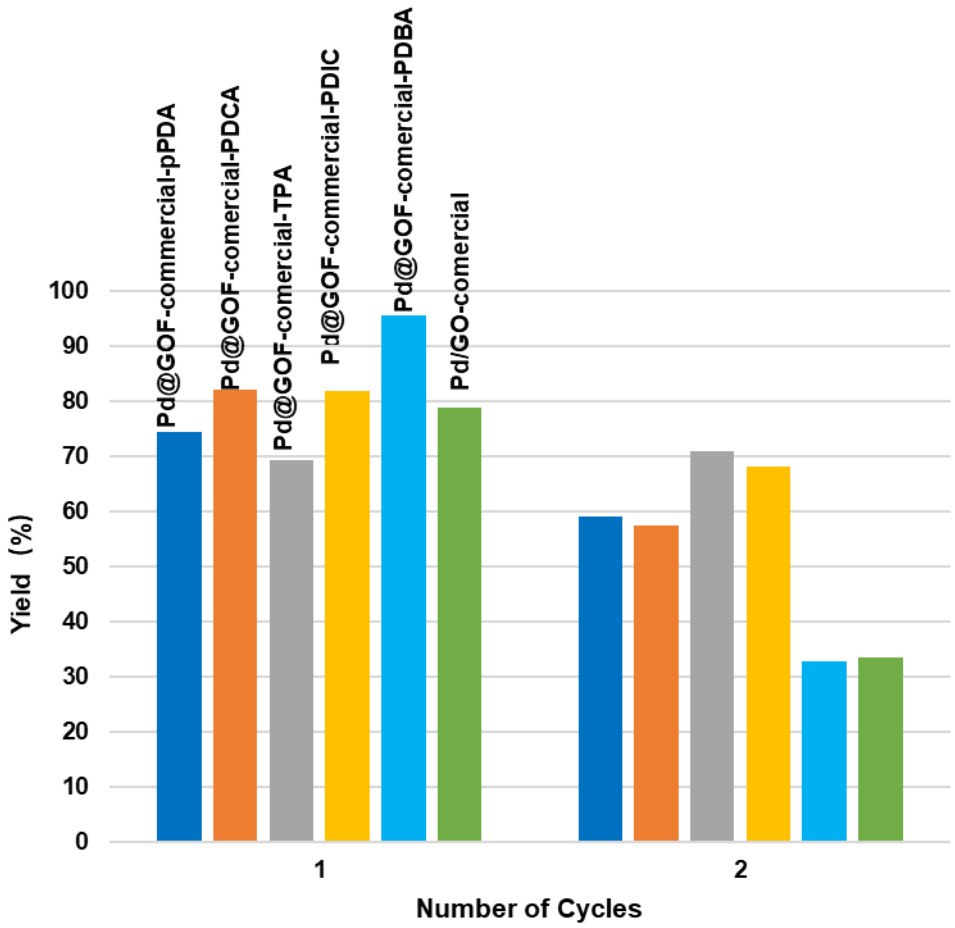

Figure 4.15 Catalytic test for Pd@GOFs and Pd/GO.

4.4. Conclusions

In this research, I have successfully synthesized and characterized several kinds of GOFs, which were covalently linked by five different organic linkers. This enabled me to explore the construction of GOFs by reacting various functional groups of GO with linkers. I also investigated the structural effects by varying the amount of linker. It was found that more linkers have an expansion effect on the layer spacing of GOFs. FTIR results suggest that the maximum amount of linker that can be covalently bonded depends on the number of reactive functional groups on the GO surface. I also successfully synthesized and characterized Pd@GOF catalysts. It was demonstrated that the confinement of NPs is independent of the covalent reaction between the linker and GO. These catalysts were applied to the Suzuki-Miyaura coupling reaction, where their activity and durability exhibited significant differences. This implies that linker molecules with different functional groups have a substantial impact on the catalytic performance of the synthesized GOFs.

References

(1) Ludwig, J. R.; Schindler, C. S. Catalyst: Sustainable Catalysis. *Chem* **2017**, *2* (3), 313–316. https://doi.org/10.1016/j.chempr.2017.02.014.

(2) Ataee-Esfahani, H.; Wang, L.; Nemoto, Y.; Yamauchi, Y. Synthesis of Bimetallic Au@pt Nanoparticles with Au Core and Nanostructured Pt Shell toward Highly Active Electrocatalysts. *Chem. Mater.* **2010**, *22* (23), 6310–6318. https://doi.org/10.1021/cm102074w.

(3) Wang, L.; Yamauchi, Y. Block Copolymer Mediated Synthesis of Dendritic Platinum Nanoparticles. *J. Am. Chem. Soc.* **2009**, *131* (26), 9152–9153. https://doi.org/10.1021/ja902485x.

(4) Wang, L.; Yamauchi, Y. Metallic Nanocages: Synthesis of Bimetallic Pt-Pd Hollow Nanoparticles with Dendritic Shells by Selective Chemical Etching. *J. Am. Chem. Soc.* **2013**, *135* (45), 16762–16765. https://doi.org/10.1021/ja407773x.

(5) Wang, L.; Yamauchi, Y. Autoprogrammed Synthesis of Triple-Layered Au@pd@pt Core-Shell Nanoparticles Consisting of a Au@pd Bimetallic Core and Nanoporous Pt Shell. *J. Am. Chem. Soc.* **2010**, *132* (39), 13636–13638. https://doi.org/10.1021/ja105640p.

(6) Munnik, P.; de Jongh, P. E.; de Jong, K. P. Recent Developments in the Synthesis of Supported Catalysts. *Chem. Rev.* **2015**, *115* (14), 6687–6718. https://doi.org/10.1021/cr500486u.

(7) Huo, J.; Tessonnier, J.-P.; Shanks, B. H. Improving Hydrothermal Stability of Supported Metal Catalysts for Biomass Conversions: A Review. *ACS Catal.* **2021**, *11* (9), 5248–5270. https://doi.org/10.1021/acscatal.1c00197.

(8) Haque, E.; Yamauchi, Y.; Malgras, V.; Reddy, K. R.; Yi, J. W.; Hossain, Md. S. A.; Kim, J. Nanoarchitectured Graphene-Organic Frameworks (GOFs): Synthetic Strategies, Properties, and Applications. *Chemistry – An Asian Journal* **2018**, *13* (23), 3561–3574. https://doi.org/10.1002/asia.201800984.

(9) Srinivas, G.; Burress, J. W.; Ford, J.; Yildirim, T. Porous Graphene Oxide Frameworks: Synthesis and Gas Sorption Properties. *J. Mater. Chem.* **2011**, *21* (30), 11323–11329. https://doi.org/10.1039/C1JM11699A.

(10) Nicolaï, A.; Sumpter, B. G.; Meunier, V. Tunable Water Desalination across Graphene Oxide Framework Membranes. *Phys. Chem. Chem. Phys.* **2014**, *16* (18), 8646–8654. https://doi.org/10.1039/C4CP01051E.

(11) Mercier, G.; Klechikov, A.; Hedenström, M.; Johnels, D.; Baburin, I. A.; Seifert, G.; Mysyk, R.; Talyzin, A. V. Porous Graphene Oxide/Diboronic

Acid Materials: Structure and Hydrogen Sorption. *J. Phys. Chem. C* **2015**, *119* (49), 27179–27191. https://doi.org/10.1021/acs.jpcc.5b06402.

(12) Chan, Y.; Hill, J. M. Hydrogen Storage inside Graphene-Oxide Frameworks. *Nanotechnology* **2011**, *22* (30), 305403. https://doi.org/10.1088/0957-4484/22/30/305403.

(13) Haque, E.; Islam, M. M.; Pourazadi, E.; Sarkar, S.; Harris, A. T.; Minett, A. I.; Yanmaz, E.; Alshehri, S. M.; Ide, Y.; Wu, K. C.-W.; Kaneti, Y. V.; Yamauchi, Y.; Hossain, M. S. A. Boron-Functionalized Graphene Oxide-Organic Frameworks for Highly Efficient CO2 Capture. *Chemistry, an Asian Journal* **2017**, *12* (3), 283–288. https://doi.org/10.1002/asia.201601442.

(14) Tran, T. P. N.; Thakur, A.; Trinh, D. X.; Dao, A. T. N.; Taniike, T. Design of Pd@Graphene Oxide Framework Nanocatalyst with Improved Activity and Recyclability in Suzuki-Miyaura Cross-Coupling Reaction. *Appl. Catal. A* **2018**, *549*, 60–67. https://doi.org/10.1016/j.apcata.2017.09.026.

(15) Tran, T. P. N.; Nguyen, T. N.; Taniike, T.; Nishimura, S. Tailoring Graphene Oxide Framework with N- and S- Containing Organic Ligands for the Confinement of Pd Nanoparticles Towards Recyclable Catalyst Systems. *Catal. Lett.* **2021**, *151* (1), 247–254. https://doi.org/10.1007/s10562-020-03284-y.

(16) Seenivasan, K.; Tran, T. P. N.; Mohan, P.; Ton, N. N. T.; Thakur, A.; Chammingkwan, P.; Rawat, D. S.; Taniike, T. Graphene Oxide Framework-Confined Ru (Ru@GOF) as Recyclable Catalyst for Hydrogenation of Levulinic Acid into γ-Valerolactone with Formic Acid. *J. Mater. Sci.* **2022**, *57* (25), 11714–11724. https://doi.org/10.1007/s10853-022-07340-3.

(17) Hummers, W. S.; Offeman, R. E. Preparation of Graphitic Oxide. *J. Am. Chem. Soc.* **1958**, *80* (6), 1339 – 1339. https://doi.org/10.1021/ja01539a017.

(18) Amirov, R. R.; Shayimova, J.; Nasirova, Z.; Solodov, A.; Dimiev, A. M. Analysis of Competitive Binding of Several Metal Cations by Graphene Oxide Reveals the Quantity and Spatial Distribution of Carboxyl Groups on Its Surface. *Phys. Chem. Chem. Phys.* **2018**, *20* (4), 2320–2329. https://doi.org/10.1039/C7CP07055A.

(19) Khan, M. U.; Shaida, M. A. Reduction Mechanism of Graphene Oxide Including Various Parameters Affecting the C/O Ratio. *Mater. Today Commun.* **2023**, *36*, 106577. https://doi.org/10.1016/j.mtcomm.2023.106577.

(20) Lesiak, B.; Trykowski, G.; Tóth, J.; Biniak, S.; Kövér, L.; Rangam, N.; Stobinski, L.; Malolepszy, A. Chemical and Structural Properties of Reduced Graphene Oxide—Dependence on the Reducing Agent. *J. Mater. Sci.* **2021**, *56* (5), 3738–3754. https://doi.org/10.1007/s10853-020-05461-1.

(21) Sparavigna, A. C. Graphene and Graphene Oxide (Raman Spectroscopy). May 10, 2024. https://doi.org/10.26434/chemrxiv-2024-86stv-v2.

(22) Burress, J. W.; Gadipelli, S.; Ford, J.; Simmons, J. M.; Zhou, W.; Yildirim, T. Graphene Oxide Framework Materials: Theoretical Predictions and Experimental Results. *Angew. Chem. Int. Ed.* **2010**, *49* (47), 8902–8904. https://doi.org/10.1002/anie.201003328.

Chapter 5

General Conclusion

Chapter 5

Graphene oxide (GO) and its derivatives possess high surface area, excellent properties, and easy modifiability, making them promising candidates for a wide range of applications in the catalytic field. The properties of GO significantly influence the performance of its derivatives and corresponding catalysts. However, research on the relationship between the characteristics of GO, its derivatives, and catalyst performance is still lacking. This paper aims to clarify the impact of GO and its derivatives' properties on catalytic reactions. The main work is as follows:

In **Chapter 2**, by synthesizing graphene oxide frameworks (GOFs) and catalysts based on GO of different qualities and characterizing them through various methods, this study elucidated how the properties of GO influence catalytic performance. The research revealed that the oxygen-containing functional groups and the lateral size of GO sheets significantly impact their catalytic performance.

In **Chapter 3**, by comparing the performance of various GO-supported palladium nanocatalysts in the hydrogen evolution reaction (HER), we examined how different properties of GO affect electrocatalytic performance. This study found that the functional groups on GO and the lateral size of GO sheets significantly influence electrocatalytic performance.

Chapter 5

In **Chapter 4**, using various linker molecules with different functional groups, we synthesized GOFs to explore their impact on catalytic performance. This study found that while the linker's functional groups did not affect particle confinement, they had a significant influence on the catalytic performance.

In conclusion, the research investigates the influence of different physicochemical properties of GO on performance and stability in various catalytic reactions from three distinct perspectives. This study highlights the importance of GO characteristics in designing high-performance nanocatalysts and provides valuable insights for synthesizing high-quality GO-based nanocatalysts.

List of publications and other achievements

Publications

1. **Gao, C.**; Wada, T.; Seenivasan, K.; Chammingkwan, P.; Taniike, T. Critical Properties for Stabilizing Pd Nanoparticles in Graphene Oxide Framework-Supported Catalysts: Insights from Multifaceted Characterization. Langmuir 2025. 41 (24), 15619-14529.

2. Krishina, S.; **GAO C.**; Wada, T.; Mukherjee, P.; Senivansan, K.; Taniike, T. Structure-driven performance enhancement in palladium–graphene oxide catalysts for electrochemical hydrogen evolution. Materials 2024, 17, 5296

Conferences

Domestic Conference

1. **Ce Gao,** Kalaivani Seenivasan, Toru Wada, Toshiaki Taniike, Cooperative Influences of Nanoparticle Localization and Phase Coarsening on Thermal Conductivity of Ternary Nanocomposites, The Chemical Society of Japan, Kinki Branch, Hokuriku District Lecture Meeting and Research Presentation, Nov. 17, 2023.

Achievements

International Conferences

1. **Ce Gao,** Kalaivani Seenivasan, Toru Wada, Toshiaki Taniike, Tuning the nature of graphene oxide frameworks used as support for palladium nanoparticle catalyst. , The 9th Asia Pacific Congress on Catalysis (APCAT-9), Hongzhou, China, Oct. 30-Nov.2, 2023.